THE DESIGN AND FABRICATION OF A HIGH-T_C DC SQUID GRADIOMETER

E. C. Knox-Davies

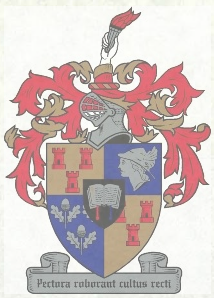

Thesis presented in partial fulfilment of the requirements for the degree of Master of Engineering at the University of Stellenbosch.

Supervisor: Prof. W. J. Perold

December 1999

Declaration

I, the undersigned, hereby declare that the work contained in this thesis is my own original work unless indicated otherwise and that it has not previously in its entirety or in part been submitted at any university for a degree.

E. C. Knox-Davies

25/11/1999

Date

Abstract

Superconducting quantum interference devices (SQUIDs) are very sensitive magnetic field sensors, finding applications in fundamental physics, non-destructive testing, biomagnetism and geophysics. This thesis describes how to design and fabricate a high-temperature dc SQUID gradiometer for operation at 77 K.

A design procedure for directly coupled SQUID gradiometers which incorporates recommendations and typical parameter values from literature is described. It is used to design a gradiometer and estimate its electrical parameters. The effect of thermal noise on the SQUID sensitivity as well as the current opinion on the mechanism and contribution of flicker noise are discussed. A number of commonly used SQUID read-out schemes and their respective merits are discussed.

The SQUID fabrication process and the optimisations necessary to perfect the process are described in some detail. A thin film of $YBa_2Cu_3O_7$, a high-temperature superconductor, is prepared by pulsed laser deposition on an MgO bicrystal substrate. The film is then patterned by conventional photolithography and wet etching to produce the desired circuit shape and form Josephson junctions on the bicrystal's grain boundary. Gold contact pads are deposited through a mask by pulsed laser deposition. A simpler version of the same fabrication process can be used to manufacture microwave filters.

Two attempts were made at constructing a Josephson junction test circuit but at no point did measurements of the fabricated junctions ever detect Josephson behaviour. This can be directly attributed to an inferior quality thin film. It was not attempted to fabricate the SQUID gradiometer because the successful operation of Josephson junctions could not be demonstrated.

Although the testing of the junctions did not produce positive results, the entire fabrication process, except for the deposition of a good quality film, has been demonstrated to be a success. Once a good quality superconducting film can be deposited, it should be straightforward to fabricate working Josephson junctions and SQUIDs.

Opsomming

'n SQUID (supergeleidende kwantum interferensie toestel) is 'n baie sensitiewe magnetiese-veld sensor wat verskeie toepassings het, soos byvoorbeeld in fundamentele fisika, nie-destruktiewe metings, bio-magnetisme en geofisika. Hierdie tesis beskryf hoe om 'n hoë-temperatuur gs SQUID magnetiese gradiëntmeter vir operasie by 77 K te ontwerp.

'n Ontwerpsprosedure vir direk-gekoppelde SQUID gradiëntmeters word daargestel. Tipiese parameter waardes en voorstelle wat in die literatuur beskryf word, word benut in hierdie prosedure, wat die ontwerp van 'n gradiëntmeter en die beraming van die elektriese eienskappe behels. Termiese ruis word in ag geneem deur die effek daarvan op die sensitiwiteit van die SQUID te beskryf. Die mees onlangse idees vir die verskynsel en effek van flikker ruis word ook bespreek. Algemene SQUID uitleesskemas en die meriete van elk word ook verduidelik.

Baie aandag word in die tesis bestee aan die besonderhede van die vervaardiging van 'n SQUID, sowel as die optimeringsstappe wat gevolg is. 'n $YBa_2Cu_3O_7$ dunfilm ('n hoë-temperatuur supergeleier), word deur middel van gepulsde laserdeposisie op 'n MgO bikristal substraat gedeponeer. Die film word dan deur standaard fotolitografie en nat etsing gevorm om Josephsonvlakke op die bikristal se greinvlak sowel as die gewensde stroombaanuitleg te vorm. Goud kontakte word deur middel van gepulsde laserdeposisie deur 'n masker gedeponeer. 'n Eenvoudiger weergawe van bogenoemde vervaardigingsproses kan ook gebruik word om mikrogolffilters te produseer.

Twee pogings is aangewend om 'n Josephson vlak toetsbaan te bou, maar geen Josephson gedrag kon deur metings waargeneem word nie. Dit kan definitief toegeskryf word aan die swak kwaliteit van die dunfilm. 'n SQUID gradiëntmeter is nie vervaardig nie, aangesien die korrekte werking van die Josephson vlakke nie waargeneem kon word nie.

Buiten vir die feit dat die toetsing van die Josephson vlakke nie positiewe resultate gelewer het nie, was die fabrikasieproses, met uitsondering van 'n goeie film deposisie, duidelik 'n sukses. Sodra hierdie probleem oorbrug kan word, behoort dit eenvoudig te wees om werkende Josephson vlakke en SQUIDs te vervaardig.

Acknowledgements

Many people have supported me during this thesis and it is not possible to mention them all individually. Nevertheless, there are a few that I should like to thank in particular.

I should like to thank Professor W. J. Perold for his patience, encouragement and help in the course of this thesis. His optimism and infectious enthusiasm never failed to have a positive effect.

I should like to thank my friends for their companionship and support. I should especially like to thank Riana for proofreading this thesis and for providing much needed encouragement when things looked difficult.

Lastly, I should like to thank my mother who helped to keep me motivated and also gave advice on language usage.

Contents

Chapter 1

Introduction

1.1 Early history and basic properties of superconductivity

1.1.1 Discovery

The phenomenon known as superconductivity was discovered by Kamerlingh Onnes while doing low-temperature research at the University of Leiden. He noticed that the resistance of a mercury sample suddenly became unmeasurably small when cooled below a critical temperature T_c. Investigating the effects of high currents and magnetic fields, he found that superconductivity would lapse if the magnetic field applied to the sample exceeded a critical value H_c or the current density in the material exceeded a critical current density J_c. He also noted the temperature dependence of these parameters. Superconductivity exists under a surface delimited by a critical temperature, current density and magnetic field as shown in Figure 1.1. If any of these parameters is exceeded, superconductivity is destroyed. In 1913, Kamerlingh Onnes was awarded the Nobel Prize in Physics for his low-temperature work.

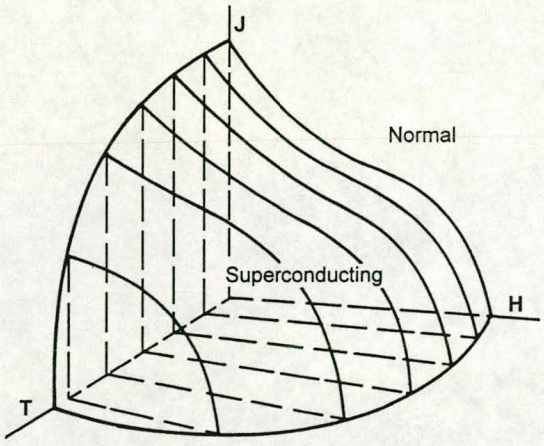

Figure 1.1 The surface under which superconductivity can exist [1].

At the time of these discoveries, the critical currents of known superconductors were so low as to prevent large-scale application in engineering. It is also interesting to note that superconductivity does not occur in copper, gold, silver and platinum which are all very good conductors at room temperature.

1.1.2 The Meissner effect

In 1933, W. H. Meissner and R. Ochsenfeld found that a superconductor expels an applied magnetic field [2]. This is true whatever the superconductor's thermal or magnetic history. The magnetic flux in the interior of the superconductor is zero

which means that a superconductor is a perfect diamagnet. The flux is expelled by surface currents flowing in such a way as to create an opposing field. That superconductivity is not just perfect conductivity is demonstrated by the fact that when a material is cooled down in the presence of a magnetic field, it expels the field as soon as it becomes superconducting. A perfect conductor would merely maintain the magnetic field which is present when the material becomes perfectly conducting. To say that flux is completely expelled from a superconductor is not strictly true. The magnetic field does in fact penetrate the superconductor for a short distance known as the London penetration depth λ_L. The Meissner effect is responsible for the levitation of a small superconductor above a magnet.

Superconductors can be classified as being of either type I or type II. Type I superconductors are completely diamagnetic below H_c and the Meissner effect holds true. Most of the superconducting elemental metals, except for niobium, are of type I. Above H_c, an applied magnetic field fully penetrates the material and electrical resistance is restored. Type II materials, e.g. $YBa_2Cu_3O_7$, behave like those of type I until the applied field reaches H_{c1}. Thereafter, they allow some magnetic flux to penetrate until H_{c2} at which point superconductivity is lost completely.

1.2 Theories, models and modern history of superconductivity

The most import theories and models will be mentioned here but not discussed in any depth as detailed descriptions can be found in any superconductivity textbook (e.g. [4]). Those models more directly related to the topic of the thesis will be dealt with at a later stage in some detail.

1.2.1 The two-fluid model

Gorter and Casimir proposed this model in 1934 to explain superconductivity [3]. Current flow in a superconductor is due to two parts. In the normal or ohmic channel, the charge carriers are normal electrons. In the other channel, superelectrons carry the current without resistance. The ratio of superelectrons to the total number of charge carriers in the material increases as the temperature is decreased. At $T = 0$, all the current is carried by the superelectrons and above $T = T_c$, only normal electrons exist. In the later BCS theory, superelectrons are shown to be pairs of bound electrons which break apart as the temperature rises.

1.2.2 The London theory

In 1935, Fritz and Heintz London developed a phenomenological theory of superconductivity described by two equations [4],

$$\mathbf{E} = \frac{\partial}{\partial t}(\Lambda \mathbf{J}) \tag{1.1}$$

and

$$\nabla\times(\Lambda\mathbf{J}) = -\mathbf{B}\,, \tag{1.2}$$

where $\Lambda \equiv \dfrac{m^*}{n^*(q^*)^2}$ and m^*, n^* and q^* are respectively the mass, density and charge of superelectron pairs.

The first London equation shows that a perfect conductor develops a voltage across it when it is driven by a time-varying current. By manipulation of Maxwell's equations and substitution of this equation, it is possible to obtain a characteristic length

$$\lambda_L = \sqrt{\frac{\Lambda}{\mu_0}} \tag{1.3}$$

associated with the properties of the system. This length is called the London penetration depth and is the extent to which a magnetic field penetrates a superconductor. It is similar to the skin depth in a normal conductor but frequency independent.

The second London equation is a postulate to guarantee that magnetic flux be expelled from a superconductor, in other words to force the Meissner effect to be true. In 1948, Fritz London showed that that the two London equations are a result of the quantum mechanical nature of superconductivity. This was the first theory to describe the properties of superconductors in the presence of electromagnetic fields.

1.2.3 The Ginzburg-Landau theory

The Russians, Vitaly Ginzburg and Lev Landau published a more complex extension to the London theory in 1950. It uses for the first time the concept of a quantum mechanical wave function φ to describe the state of the superconductor [5].

Using this theory, the flux passing through the centre of a superconducting ring can be shown to be quantised, the smallest elementary unit being the fluxon $\Phi_0 = h/2e = 2.07\times10^{-15}$ Wb. Here, h is Planck's constant and e is the negative charge of one electron.

1.2.4 The BCS theory

A big breakthrough in the understanding of superconductivity came in 1957 when John Bardeen, Leon Cooper and Robert Schrieffer published what is now called the BCS theory. Their theory explains the nature and origin of the superconducting state using quantum mechanics. It shows that below T_c, normal electrons start forming coherent electron pairs, called Cooper pairs, which carry the supercurrent. They

remain correlated over a distance called the coherence length. The number of Cooper pairs is a function of temperature. The electrons of the Cooper pair are bound together with an energy 2Δ, called the energy gap. When this energy is exceeded by the photon energy (hf) at high frequencies, the Cooper pairs break up. The upper frequency limit for superconductivity in YBCO is about 7 THz for temperatures well below T_c [6].

A superconductor shows a resistance when passing a time-varying current because some of the current is carried by normal electrons and not by the Cooper pairs. This effect also follows from the two-fluid model. For most ac applications, the resistance is usually much lower than that of good normal conductors.

The BCS theory is able to explain the observation that good conductors make poor superconductors and vice versa. Bardeen, Cooper and Schrieffer received the 1972 Nobel Prize in Physics.

1.2.5 The Josephson effect

In 1962, Brian Josephson, a research student at the Cavendish laboratory in Cambridge, proposed that Cooper pairs could tunnel through a thin insulating barrier placed between two superconductors (now called a Josephson junction) [5]. He predicted two effects, now known as the dc and ac Josephson effects.

The dc Josephson effect predicts that tunnelling will occur without resistance and produce a dc current through the junction without the application of a voltage, or more simply,

$$v = 0 \text{ for } i < I_c , \tag{1.4}$$

where I_c is the critical current of the junction.

The ac effect states that if a dc voltage is applied to the junction, an alternating current will flow through it, that is

$$i = I_c \sin\left[\frac{2\pi Vt}{\Phi_0} + \varphi(0)\right], \tag{1.5}$$

where $\varphi(0)$ is an arbitrary phase constant and t is the time.

Initially his ideas were not that clearly formulated and they were received with much scepticism. Soon afterwards, however, John Rowell and Philip Anderson verified his predictions in their experiments [4]. Josephson received the 1973 Nobel Prize for his work.

1.2.6 High-T_c superconductors

High-temperature superconductivity was discovered in 1986 by Georg Bednorz and Karl Alex Müller who jointly won the 1987 Nobel Prize. They found that a ceramic consisting of a lanthanum oxide, barium and copper had a critical temperature of about 30 K [2]. The critical temperatures of the pure metals are in the range 0.01–9.15 K.

In early 1987, a group headed by C. W. Chu and M. K. Wu created the substance $YBa_2Cu_3O_7$ (YBCO) which has a critical temperature above 90 K. It was the first material with a critical temperature high enough to be maintained in the superconducting state by liquid nitrogen. This was a tremendous breakthrough which suddenly made superconductor applications potentially viable commercially. Liquid nitrogen boils at 77 K. It is cheap, readily available and can be stored for prolonged periods. The critical temperatures of some materials are now reported to exceed 125 K. At present, the mechanism for superconductivity at high temperatures is not completely understood.

1.3 Applications of superconductors

1.3.1 Bulk superconductors

The potential applications of superconductors cover the entire spectrum of engineering fields. High field, high current electromagnets is one of the applications to which superconductors are most suited. They dissipate no heat during operation and once charged, can be kept operational by power from an ordinary wall socket. Electromagnets are made from type II superconductors because they have higher critical magnetic fields. Another consideration in the choice of the material is mechanical strength because forces on the solenoid's superconducting wire can be considerable. Commercial magnets with fields in excess of 10 T have been constructed [4].

Large magnets are used in electric motors, bubble and spark chambers for particle detection, the containment of plasmas in controlled nuclear fusion and for levitating high-speed trains [1]. They are also used to provide the large magnetic field necessary for magnetic resonance imaging (MRI). Although there are at present better ways of storing energy, there are applications where very short, high bursts of power are required and superconducting storage solenoids are ideal for this purpose.

The use of superconducting cables in power transmission systems is very attractive because there are no losses at dc. Cables can be made much thinner than is possible with conventional copper wires. Another attractive feature is their low working voltage. Savings can therefore be made on electrical insulation. It is not necessary to step up the voltage with transformers to minimise cable loss. Ac superconducting cables are not quite as ideal. There can be significant losses, even at 50 Hz [7]. Reliability and fault tolerance are potential problems for both ac and dc transmission cables. If a single part of the line loses superconductivity, that small section can

cause a runaway heating effect, destroying superconductivity along the line and possibly destroying the cable itself.

The Meissner effect makes superconductors good materials for shielding against low-frequency (< 1 kHz) magnetic interference. Instead of shielding by diverting the magnetic fields into materials of high permeability, screening currents generate opposing fields which cancel out the effects of the interfering fields.

1.3.2 Electronic devices

Josephson junctions are being used to create logic gates, memory cells and analogue-to-digital converters which have extremely high switching speeds and low-power dissipation (e.g. [8]). These are likely to find use in digital signal processing. Josephson junctions are also used as the basis for a highly accurate primary voltage standard by utilising the ac Josephson effect.

Superconducting quantum interference device (SQUID) magnetometers are available which can measure magnetic fields of the order of 10^{-14} T [2]. The earth's magnetic field is $0.2 - 0.7 \times 10^{-4}$ T for comparison. With these magnetometers, it is possible to detect biomagnetic fields such as those of the human brain which are too small to be measured by any other technology. There are two types of activity which are of interest, namely spontaneous activity such as that of epilepsy, and evoked responses to stimuli such as audible tones of varying frequency. In electromagnetically quiet environments, SQUIDs can be used without shielding to measure the earth's magnetic field with greater accuracy than is possible with conventional devices.

There has been some experimental work carried out on making extremely sensitive metal detectors for underwater operation [9, 10]. A low-frequency magnetic transmitter is used in conjunction with a SQUID gradiometer receiver to form a kind of magnetic radar. This system is particularly advantageous in situations where conventional detection techniques cannot be used.

Superconducting measurement systems find use in fundamental physics experiments. Gravity wave antennas are used to search for the pulse of gravitational radiation which is expected to be emitted when a star collapses [11]. A SQUID is used to measure the minute displacements such a pulse would cause to a Weber bar gravity wave antenna. The same displacement transducer can be used to measure small gradients in the earth's gravitational field.

A SQUID coupled to a superconducting ring can be used to detect the possible existence of magnetic monopoles [12]. The passage of a magnetic dipole or electrically charged particle through the ring causes a momentary change in the ring flux. A magnetic monopole, on the other hand, would cause a step change in the flux which would remain indefinitely.

It is possible to measure absolute temperature down to the millikelvin region by measuring thermal noise directly, using a SQUID as a very sensitive preamplifier [12]. Because low temperatures and small losses reduce the noise in a system,

superconductors are used in the first stages of amplification of very small signals such as in radio astronomy receivers.

The cellphone industry is now using low noise, low insertion loss superconducting front-end filters on its base stations. This allows cellphones' output power to be dropped in the interests of safety and extended battery life.

Josephson junctions are natural voltage-controlled oscillators. Arrays of junctions can be utilised as high-frequency sources up to frequencies of several THz [13]. Superconductor-insulator-superconductor (SIS) junctions exploit tunnelling by quasi-particles and not Cooper pairs. They can be used to construct very high sensitivity detectors and mixers in the millimetre wave region for use in radio telescopes, for example.

The cooling of superconducting devices is not as problematic as it was in earlier years, especially for high-temperature superconductors. It is now over ten years since the fabrication of the first superconductor which could be cooled by liquid nitrogen. It is becoming more financially viable to use superconductors in a variety of applications. It is also becoming increasingly difficult to fabricate faster silicon-based integrated circuits and superconducting electronics have already been tested at clock speeds greater than 10 GHz. At present, superconducting devices are still predominantly used in specialised and controlled environments but the next few years should see an increasing number of applications making their way from the laboratory to the real world.

1.4 Aims and overview of thesis

The aim of this thesis is to attempt the fabrication of a SQUID magnetometer at the University of Stellenbosch. The magnetometer should be relatively low-cost so existing facilities should be used as much as possible. In addition, the magnetometer should be able to operate in a relatively unshielded environment. This would eliminate the need for expensive magnetic shielding and make it more useful in a variety of non-laboratory applications. In the ideal case, it should be sensitive enough to detect biomagnetic fields, yet robust enough to be used in magnetic flaw detection.

The foundations for this thesis were laid by Jaco Maritz [14] and Ewan Conradie [15] with their work at the National Accelerator Centre (NAC). Their work involved characterising the process used to deposit superconducting YBCO films using laser ablation. With that process working reliably, it is possible to deposit high quality thin films which can be fashioned to make superconducting devices.

In this chapter, a brief overview has been given of the history and applications of superconductivity. In Chapter 2, the simplest mathematics of Josephson junctions leading up to the most basic governing equations of a dc SQUID are described. In addition, a number of SQUID read-out schemes described in the literature are discussed. Chapter 3 gives a detailed procedure which describes how to go about designing a high-T_c dc SQUID gradiometer. The effect of thermal noise on the SQUID sensitivity as well as the current opinion on the mechanism and contribution

of flicker noise are included. The complete SQUID fabrication process is described in Chapter 4. All the problems and the optimisations which had to be carried out are also described. In Chapter 5, a Josephson junction test circuit is constructed. The measurement set-up for determining the critical currents and normal resistances of the Josephson junctions is given together with the measurement results. Chapter 6 details what has been achieved in this thesis and what remains to be done. Recommendations for future attempts at SQUID fabrication are also made. The appendices give detailed information on a number of topics. This includes recipes for some of the chemicals used and precise instructions for operating the fabrication equipment.

Chapter 2

Superconductor device mathematics and SQUID read-out schemes

In this chapter, Josephson junction devices are examined in more detail. The first section deals with the properties of Josephson junctions and how they can be modelled. The second section discusses SQUIDs as magnetometers, devices which use these junctions as building blocks. A model of the dc SQUID which can be used in the SPICE simulation package [16] is also developed. Lastly, several popular SQUID read-out schemes are discussed.

2.1 The Josephson effect

If an insulating layer is inserted between two pieces of normal metal or superconductor as shown in Figure 2.1, one expects that no dc current can flow through this junction unless electrical breakdown occurs. However, there is a small but non-zero probability that an electron can tunnel through an insulator which has a higher energy potential barrier than the energy of the electron. If the insulator is made very thin and there are many charge carriers (as is true in a metal), a measurable dc current can indeed flow through the insulator.

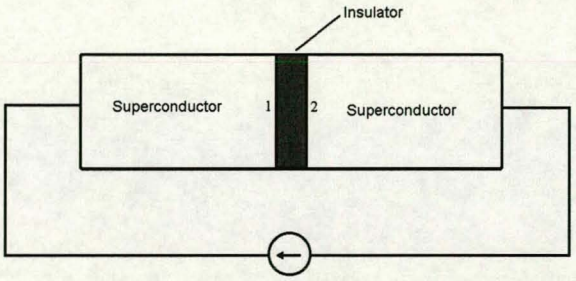

Figure 2.1 Josephson junction made by inserting a thin insulating layer between two superconductors.

Using the BCS theory, Josephson calculated that the probability of a Cooper pair (in a superconductor) tunnelling through the barrier can be comparable to that for a single electron [2]. A dc current of these pairs can flow through the junction without generating a voltage across it. The maximum current density that can exist in the junction without generating a voltage is known as the Josephson critical current density. It will be denoted j_c to avoid confusion with the critical current density of a superconductor J_c. The value of j_c changes in the presence of a magnetic field.

If the current through a junction is constrained never to exceed the Josephson critical current I_c (which is obtained by integrating j_c across the junction area), a relatively simple model can be used to describe the junction's behaviour. Such a junction is

termed a basic Josephson junction. If, however, the current is allowed to exceed I_c, a number of additional elements must be added to the model.

2.1.1 Basic Josephson junctions [4]

The junction current is related to the gauge-invariant phase difference φ by

$$i = I_c \sin\varphi \tag{2.1}$$

and the gauge-invariant phase difference is related to the voltage across the junction by

$$\frac{d\varphi}{dt} = \frac{2\pi}{\Phi_0} v . \tag{2.2}$$

The gauge-invariant phase difference is related to the phases of the wave function on both sides of the junction by

$$\varphi = \theta_1 - \theta_2 - \frac{2\pi}{\Phi_0}\int_1^2 \mathbf{A}\cdot d\mathbf{l} , \tag{2.3}$$

where $\mathbf{A}$ is the magnetic vector potential.

From these relations, it can be seen that a constant current can flow through the junction without generating a voltage (dc Josephson effect) and if a constant voltage is imposed across the junction, the current will oscillate at a frequency of 483.60 MHz/μV (ac Josephson effect).

The circuit symbol of a Josephson junction is given in Figure 2.2.

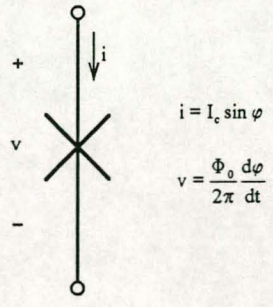

Figure 2.2 Symbol of a basic Josephson junction.

Tunnel junctions are not the only structures that exhibit the Josephson effect. Weak links (micro bridges) and grain-boundary junctions (GBJs) show the same behaviour.

2.1.2 Generalised Josephson junctions

The most important additional parameter is a non-linear resistance which is often approximated with the piecewise-linear function

$$R(v) = \begin{cases} R_{sg}(T) & \text{if } |v| < 2\Delta(T)/e \\ R_N & \text{otherwise} \end{cases}. \tag{2.4}$$

With the addition of this approximation of the resistance, the model is called the non-linear resistively shunted junction (NRSJ) model. Below the gap voltage $V_g = 2\Delta/e$ (where 2Δ is the energy required to break up a Cooper pair), at $T = 0$, the value of the resistance is infinite. However, at a finite temperature, it takes on a value called the subgap resistance R_{sg}. This contribution is caused by the fact that at finite temperatures there exist normal electrons which can tunnel. Above the gap voltage, the resistor takes on the value of the normal resistance of the junction. At this point, the voltage is high enough to break all the Cooper pairs into normal electrons.

The non-linear resistance can be approximated by a constant resistance R_N. This is known as the resistively shunted junction (RSJ) model. It eases the intensive computational requirements imposed by the non-linearity when the junction response is simulated using a time-domain, differential equation solver such as SPICE. It is an acceptable approximation for temperatures just below T_c.

The junction capacitance is calculated in the same way as for a parallel plate capacitor; i.e., $C = \varepsilon A/d$ where ε, A and d are respectively the permittivity, cross-sectional area and thickness of the insulator.

The Stewart-McCumber parameter defined by

$$\beta_c = \frac{R_N C}{\tau_J}, \text{ where } \tau_J = \frac{\Phi_0}{2\pi I_c R_N}, \tag{2.5}$$

is a measure of the effect of the junction capacitance. The junction is termed hysteretic if $\beta_c >> 1$.

The NRSJ and RSJ models are shown in Figure 2.3.

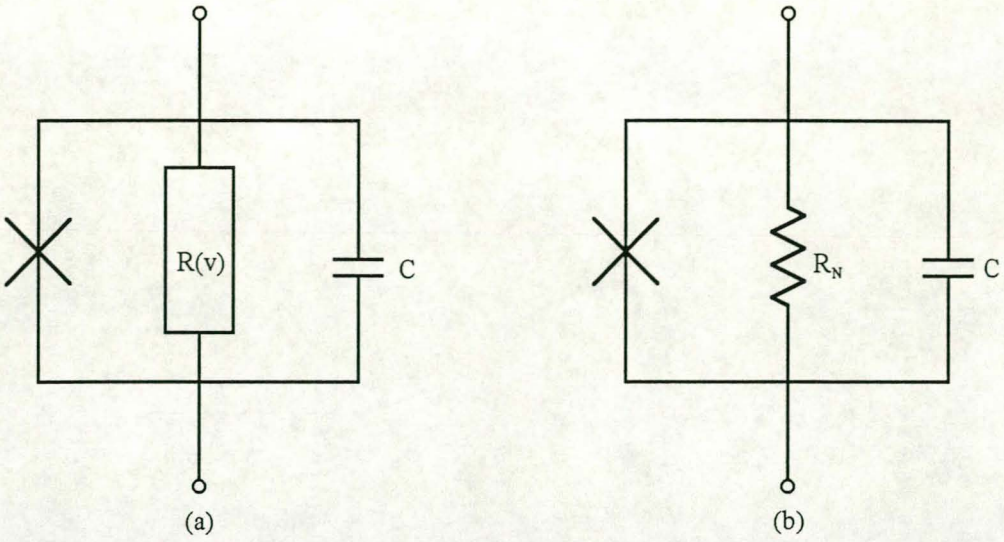

Figure 2.3 Generalised Josephson junction models. (a) NRSJ model. (b) RSJ model.

Average voltage versus current curve

If the junction current is increased from zero, no voltage is observed until the critical current is exceeded. The voltage then increases from zero to the subgap voltage. Hereafter, the voltage is related to the current by $v = iR_N$ where R_N is the normal resistance of the junction. If the current is now decreased towards the critical current, the same path is followed in reverse. What happens as the current is further reduced is determined by the value of β_c which is proportional to the capacitance of the junction. For $\beta_c << 1$, the voltage just follows the same path as when the current was increased. For $\beta_c >> 1$, the voltage is maintained until just before the current reaches zero, showing significant hysteresis. These characteristic curves are plotted in Figure 2.4.

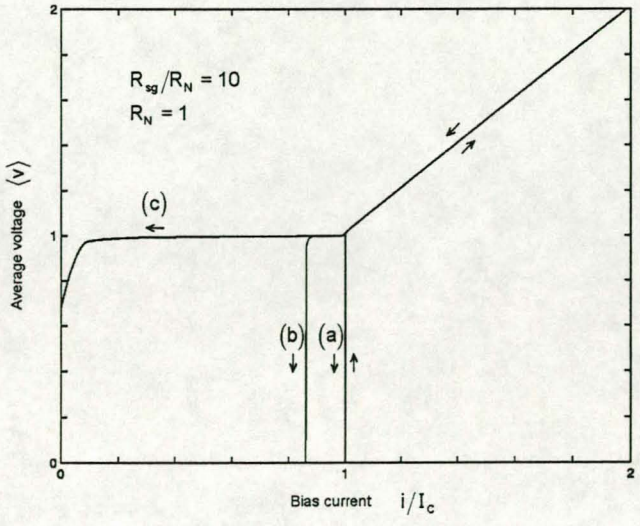

Figure 2.4 Average voltage versus current curve for (a) $\beta_c << 1$ (b) $\beta_c \approx 1$ and (c) $\beta_c >> 1$.

High-temperature superconductor grain-boundary junctions are not usually hysteretic. The exception is when such junctions fabricated on substrates with a high dielectric constant (e.g. $SrTiO_3$) are operated at temperatures below 30 K [17].

Average current versus voltage curve

At zero applied voltage, the current can take on any value between zero and the critical current. If the voltage is increased from zero, the Cooper pairs move back and forth across the junction, creating an alternating current with a zero dc average. For the NRSJ model, the only contribution is the current through the subgap resistance $i = v/R_{sg}$. Above the gap voltage, the average current is related to the voltage by $i = v/R_N$. If the voltage is now decreased to zero, the average current follows exactly the same path as on the upward sweep. No hysteresis is exhibited, irrespective of the value of β_c. This behaviour is plotted in Figure 2.5(b). Figure 2.5(a) shows the behaviour of the RSJ model and (c) gives a plot of the behaviour of a physical junction for comparison.

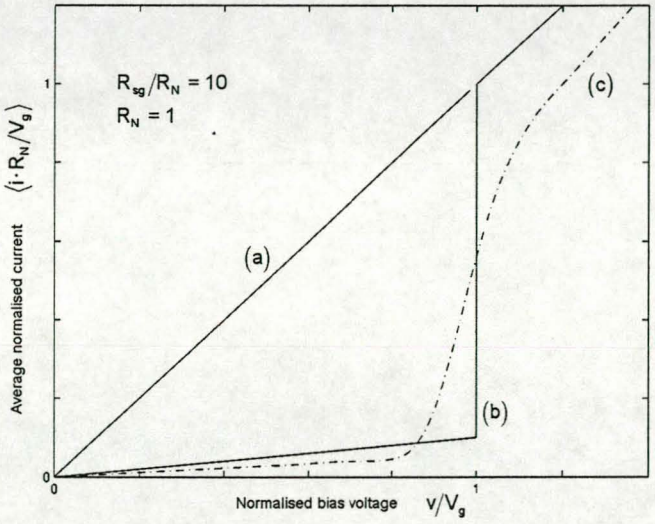

Figure 2.5 Average current versus voltage characteristic for (a) RSJ model, (b) NRSJ model and (c) physical measurement [18].

2.2 Superconducting quantum interference devices

Superconducting quantum interference devices (SQUIDs) are created by placing one or two Josephson junctions in a superconducting loop. These devices were first studied in the mid-1960's and they are widely used today as magnetic sensors.

2.2.1 RF SQUIDs

An rf SQUID is just a single Josephson junction in a superconducting loop. It has no connection leads and the read-out is done magnetically. It is biased and read out by

coupling it to an rf source or tank circuit. It will not be discussed further since it is not relevant to the topic of the thesis.

2.2.2 DC SQUIDs

Dc SQUIDs have two identical Josephson junctions in the superconducting loop. They are biased with a dc current source at slightly above twice the critical current of an individual junction. The output is simply the voltage between the current bias points. The symbol and a typical layout are given in Figure 2.6.

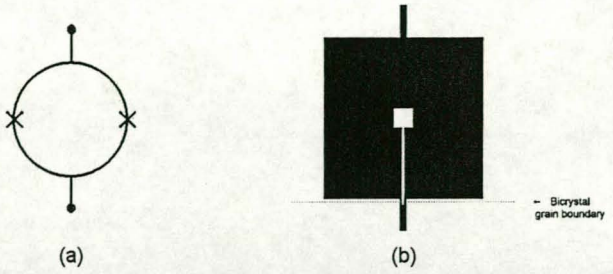

Figure 2.6 A dc SQUID. (a) Symbol and (b) typical layout.

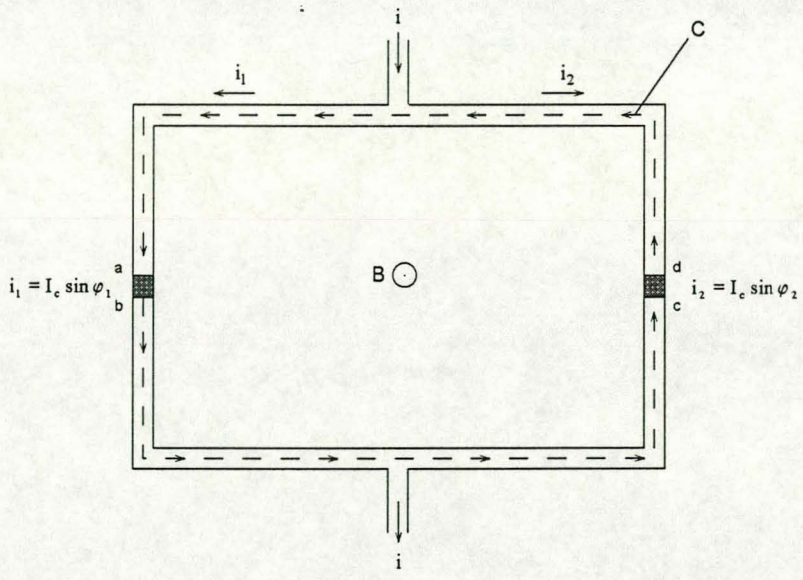

Figure 2.7 Diagram of a dc SQUID. The Josephson junctions are shown by the shaded areas and the contour of integration by the dashed line C.

The following is a brief summary of the mathematics leading up to the equations governing the dc SQUID as given in [4].

For now, the Josephson junctions are assumed to be described by Equation 2.1. The current through each junction in Figure 2.7 is given by Equation 2.1. Under the assumption of identical junctions, the total current is then

$$\begin{aligned} i &= i_1 + i_2 \\ &= I_c \sin\varphi_1 + I_c \sin\varphi_2 . \end{aligned} \tag{2.6}$$

Integrating the gauge-invariant phase difference around the loop along the contour C must give a multiple of 2π since there can only be one value of the wave function for each point around the loop. This means that

$$\begin{aligned} \oint_C \nabla\theta \cdot d\mathbf{l} &= (\theta_b - \theta_a) + (\theta_c - \theta_b) + (\theta_d - \theta_c) + (\theta_a - \theta_d) \\ &= 2\pi n . \end{aligned} \tag{2.7}$$

Using Equation 2.3, the phase differences across the junctions can be written as

$$\begin{aligned} \theta_b - \theta_a &= -\varphi_1 - \frac{2\pi}{\Phi_0}\int_a^b \mathbf{A}\cdot d\mathbf{l} \\ \theta_d - \theta_c &= \varphi_2 - \frac{2\pi}{\Phi_0}\int_c^d \mathbf{A}\cdot d\mathbf{l} . \end{aligned} \tag{2.8}$$

The supercurrent equation describing the superelectron current density in a superconductor is given by

$$\mathbf{J} = -\frac{1}{\Lambda}\left[\mathbf{A} + \frac{\Phi_0}{2\pi}\nabla\theta\right]. \tag{2.9}$$

The phase differences across the superconducting sections of the loop can then be written as

$$\begin{aligned} \theta_c - \theta_b &= \int_b^c \nabla\theta \cdot d\mathbf{l} \\ &= -\frac{2\pi}{\Phi_0}\int_b^c \Lambda\mathbf{J}\cdot d\mathbf{l} - \frac{2\pi}{\Phi_0}\int_b^c \mathbf{A}\cdot d\mathbf{l} \end{aligned}$$

$$\begin{aligned} \theta_a - \theta_d &= \int_d^a \nabla\theta \cdot d\mathbf{l} \\ &= -\frac{2\pi}{\Phi_0}\int_d^a \Lambda\mathbf{J}\cdot d\mathbf{l} - \frac{2\pi}{\Phi_0}\int_d^a \mathbf{A}\cdot d\mathbf{l} . \end{aligned} \tag{2.10}$$

The contour integral of the magnetic vector potential is equal to the flux enclosed by the loop, that is

$$\oint_C \mathbf{A}\cdot d\mathbf{l} = \Phi . \tag{2.11}$$

Substituting Equations 2.8, 2.10 and 2.11 into Equation 2.7 gives

$$\varphi_2 - \varphi_1 = 2\pi n + \frac{2\pi\Phi}{\Phi_0} + \frac{2\pi}{\Phi_0}\int_{C'} \Lambda \mathbf{J}\cdot d\mathbf{l}\,, \tag{2.12}$$

where C' is the same as contour C except that it does not include the insulators.

In a superconductor thicker than a few penetration depths, all the current flows near the surface so that if C is taken deep inside the superconductor, the contour integral of the current density is zero and

$$\varphi_2 = \varphi_1 + 2\pi n + \frac{2\pi\Phi}{\Phi_0}\,. \tag{2.13}$$

For thin superconductors, this is no longer necessarily true. However, in the case of a SQUID made out of a superconducting thin film, most of the current flows on the inside of the loop, minimising its inductance. Thus, if the integration contour is taken near the outside of the loop where the current is almost zero, the same result should be obtained.

The flux enclosed by the loop is related to the externally applied flux by

$$\Phi = \Phi_{ext} + LI_{cir}\,, \tag{2.14}$$

where $I_{cir} = \frac{1}{2}(i_1 - i_2)$ is the current circulating around the loop.

Equation 2.2 can be rearranged to give the gauge invariant phase difference across one junction in terms of its voltage as

$$\varphi_1 = \frac{2\pi}{\Phi_0}\int v\,dt\,. \tag{2.15}$$

Equations 2.1 and 2.13–2.15 are quite complex and are best solved in the time domain using SPICE. For high-temperature SQUIDs with grain-boundary junctions, the capacitor in the model is ignored. The RSJ model is used for ease of computation. The circuit of such a SPICE model is given in Figure 2.8 and the full text version in Appendix A.

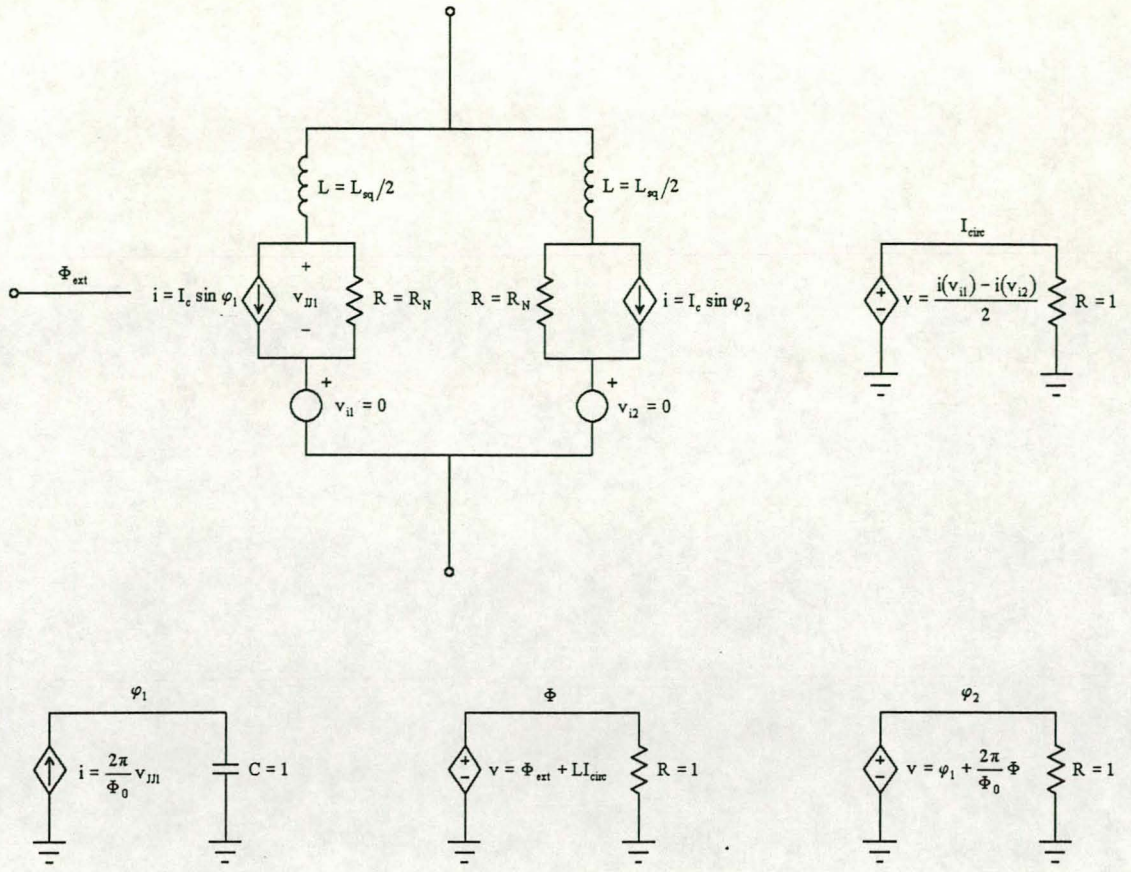

Figure 2.8 SPICE circuit model of the dc SQUID.

If the approximation is made that the SQUID inductance is negligible, the input current of the SQUID can be written by using Equation 2.1 as

$$i = I_c \sin\varphi_1 + I_c \sin\varphi_2 + \frac{2v}{R_N}, \tag{2.16}$$

where the phases are related by Equation 2.13.

By defining a new phase

$$\varphi = \varphi_1 + \frac{\pi\Phi}{\Phi_0}, \tag{2.17}$$

Equation 2.16 can be rewritten as

$$i = I_c' \sin\varphi + \frac{v}{R_N'},$$

$$\text{where } I_c' = 2I_c \cos\left(\frac{\pi\Phi}{\Phi_0}\right) \text{ and } R_N' = \frac{R_N}{2}. \tag{2.18}$$

Equation 2.18 is merely the description of a single Josephson junction. For this reason one can view a SQUID as a junction whose critical current is modulated by the applied magnetic field. This is demonstrated in Figure 2.9. In Figure 2.9(a), the curve on the right is traced out when the enclosed flux is an integer multiple of a fluxon. The other curve is for half-integer values. The average value of the SQUID voltage varies between the points where the bias-current line crosses these two curves. This happens in a roughly sinusoidal fashion with increasing enclosed flux as shown in Figure 2.9(b). The value of the bias current is chosen to maximise the amplitude of the voltage modulation. One point that must be mentioned is that the enclosed flux is related to the externally applied flux by Equation 2.14. This means that the two values will only coincide for very small SQUID inductances.

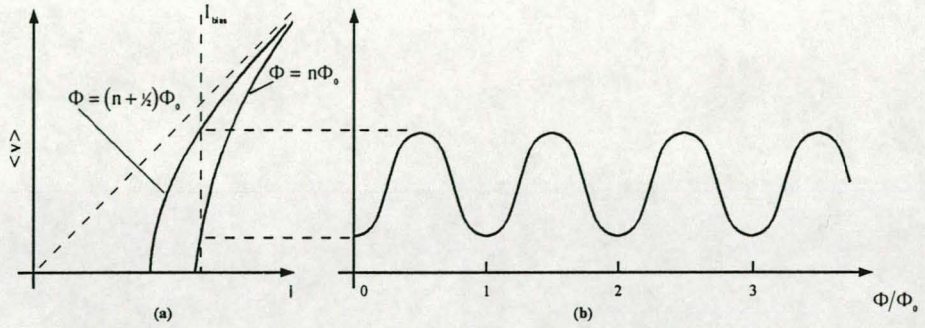

Figure 2.9 Average voltage curves as a function of (a) current and (b) applied flux, to explain the operation of a dc SQUID.

For $i > 2I_c$, the average SQUID voltage can be written in terms of the enclosed flux as

$$\langle v(t) \rangle = R_N' \sqrt{i^2 - I_c'^2}$$
$$= \frac{R_N}{2} \sqrt{i^2 - \left[2I_c \cos\left(\frac{\pi\Phi}{\Phi_0} \right) \right]^2} . \qquad (2.19)$$

This is often a useful equation to use for simulating low-inductance SQUIDs since it is considerably less computationally intensive than the full dynamic equation.

2.3 Dc SQUID read-out schemes

2.3.1 Introduction

Dc SQUIDs are very sensitive flux-to-voltage converters. Unfortunately, they are also extremely non-linear with very small output voltages. Great care must be taken when designing their read-out electronics to make full use of their high sensitivity. A simulated SQUID waveform is given in Figure 2.10(a). It contains high-frequency, non-sinusoidal oscillations. After lowpass-filtering, the waveform is as plotted in Figure 2.10(b). To obtain a linear flux-to-voltage transfer function from this curve, a

configuration called a flux-locked loop (FLL) is usually used. This section deals with the various types of FLL.

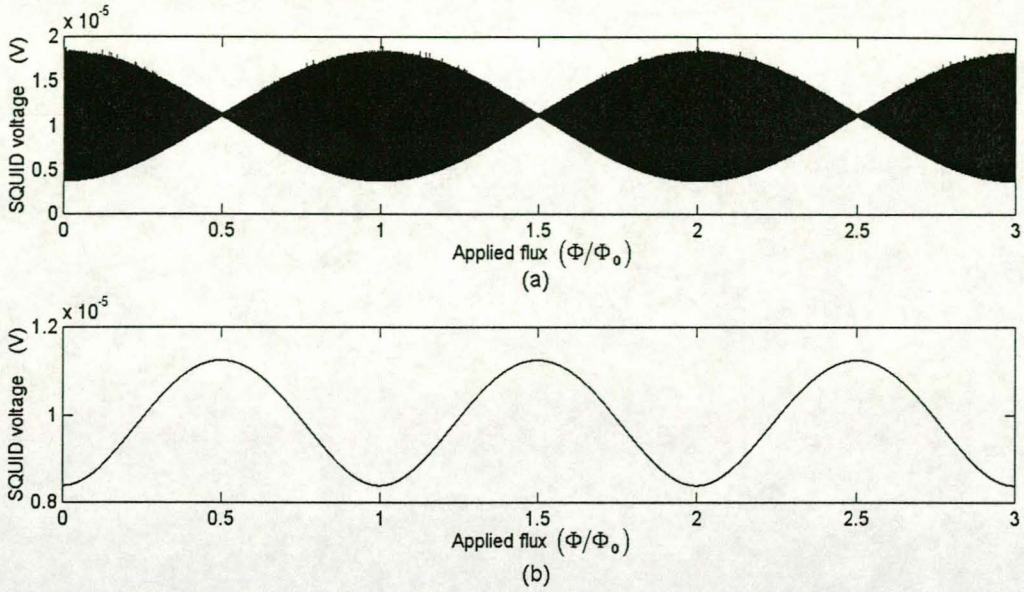

Figure 2.10 (a) Voltage versus flux graph of a dc SQUID (b) Time-averaged voltage versus flux curve.

2.3.2 Ideal flux-locked loop

The principle of this method is to keep the magnetic flux through the SQUID loop constant by applying an opposing flux with a feedback coil. The current flowing in the coil is then linearly related to the externally applied flux.

The SQUID voltage is amplified, dc shifted to have no offset, integrated and fed back through a feedback coil. This configuration is shown in Figure 2.11. The loop is locked onto the steepest part of the voltage versus flux curve, where the enclosed flux is $(n+1/4)\Phi_0$. The system works in the following way. If the externally applied flux is increased, the averaged SQUID signal will increase. This increases the integrator output and the feedback flux. Because the direction of the feedback flux is opposite to that of the external flux, the flux enclosed by the SQUID is kept fixed. The magnitudes of the applied flux and the flux generated by the feedback coil thus differ by a constant. There are a number of variations on the basic flux-locked loop which can improve its performance.

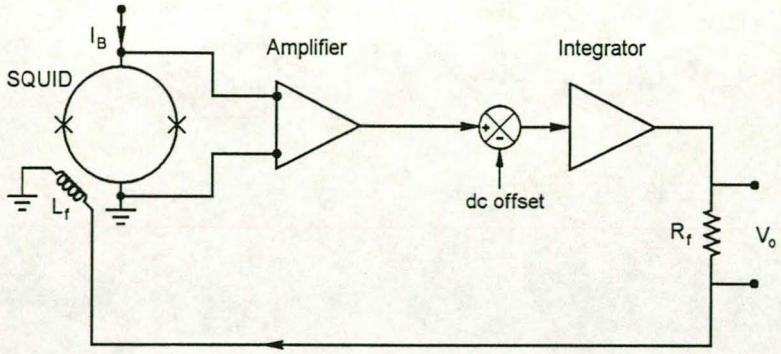

Figure 2.11 Basic flux-locked loop.

2.3.3 Flux-modulation flux-locked loop [19,20]

The problem with the ideal FLL is that the SQUID signal is small and very noisy. One way to get around this is to add a small alternating flux of $\pm 1/4\,\Phi_0$ to the feedback flux. The non-linear transfer function of the SQUID starts to generate a second harmonic of the modulating signal whenever its enclosed flux strays from $(n + 1/4)\Phi_0$. Figure 2.12 shows how this harmonic is created.

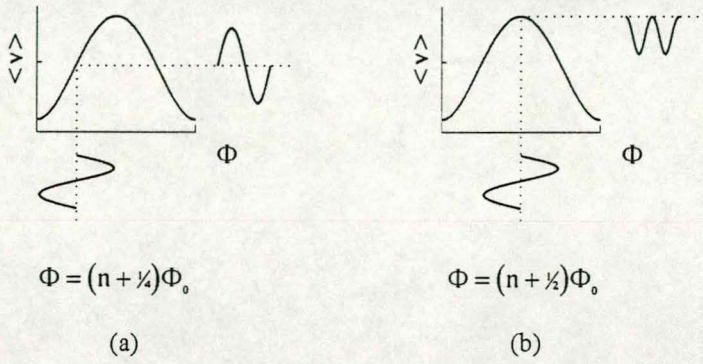

Figure 2.12 Diagram showing how a second harmonic of the modulating signal is created by the SQUID transfer function when the applied flux of (a) is increased towards that of (b).

A lock-in amplifier is used to detect the second harmonic. The detector output is integrated and fed back via the modulation coil to keep the enclosed flux constant. The configuration of the flux-modulation FLL is shown in Figure 2.13. Because the SQUID output impedance is very low, a transformer is needed to match the amplifier to the SQUID. The disadvantage of this method is the complexity of the read-out electronics.

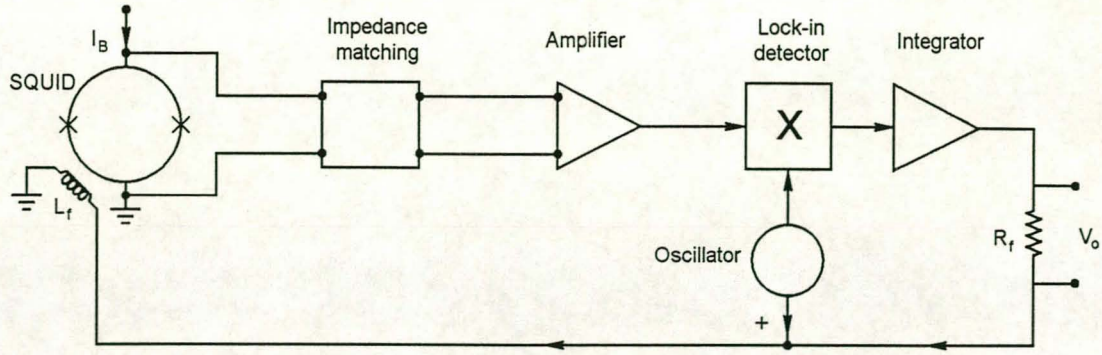

Figure 2.13 Flux-modulation FLL.

2.3.4 Relaxation-oscillation (ROS) and double relaxation-oscillation (DROS) SQUIDs [21–23]

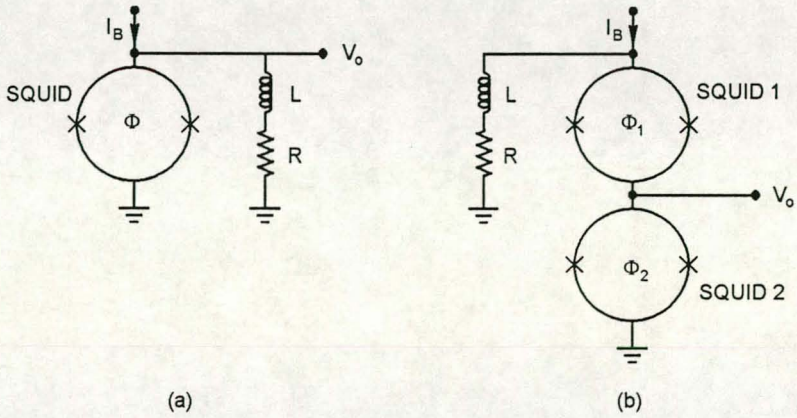

Figure 2.14 (a) Relaxation-oscillation SQUID. (b) Double relaxation-oscillation SQUID.

Low-temperature SQUIDs often have hysteretic ($\beta_c > 1$) tunnel junctions. To minimise the effect of the hysteresis, the junctions can be shunted by low-value resistors but this significantly reduces the SQUID's output voltage. The inherent hysteretic behaviour of unshunted junctions can be put to good use in relaxation-oscillation SQUIDs.

The entire SQUID is shunted by a series inductor and resistor as shown in Figure 2.14(a). The critical current is dependent on the applied flux (modulo Φ_0) and the SQUID oscillates at a frequency which is dependent on the critical current. Commercial FM devices can be used to demodulate the signal. The average voltage of the ROS is also a function of the applied flux, so a ROS can be used as both a flux-to-voltage and a flux-to-frequency converter.

A DROS (shown in Figure 2.14(b)) is constructed using two SQUIDs, a sensing and a reference SQUID. The flux to be sensed is applied to the first SQUID and a reference flux is applied to the second SQUID. Each flux sets the critical current of its own

SQUID. Only the SQUID with the smaller critical current will oscillate, and the other one will be in the zero voltage state. If, for instance, the critical current of the reference SQUID is initially slightly larger than that of the sensing SQUID, and the flux applied to the sensing SQUID is increased by an amount just large enough to reduce this SQUID's critical current below that of the reference SQUID, then the output voltage will change from zero to an oscillation whose average value is positive. This results in a very high flux-to-voltage ratio around the point where the applied flux is equal to the reference flux.

The outputs of both ROS and DROS oscillate between the voltage state ($V_o = V_g$) and the superconducting state ($V_o = 0$). ROS's with flux-to-voltage ratios of 4 mV/Φ_0 and DROS's with 10–30 mV/Φ_0 have been fabricated by Adelerhof et al. [21]. Relaxation-oscillation SQUIDs are operated as part of a flux-locked loop.

High-temperature Josephson junctions are not hysteretic, so they cannot be used in relaxation-oscillation SQUIDs. Theoretically it should be possible to increase capacitance by fabricating plates on either side of the junction. However, this is not the only problem. Successful operation of (D)ROS's depends on accurate control of parameter values. At present, this is not possible for high-temperature devices.

2.3.5 Additional positive feedback (APF) [24–28]

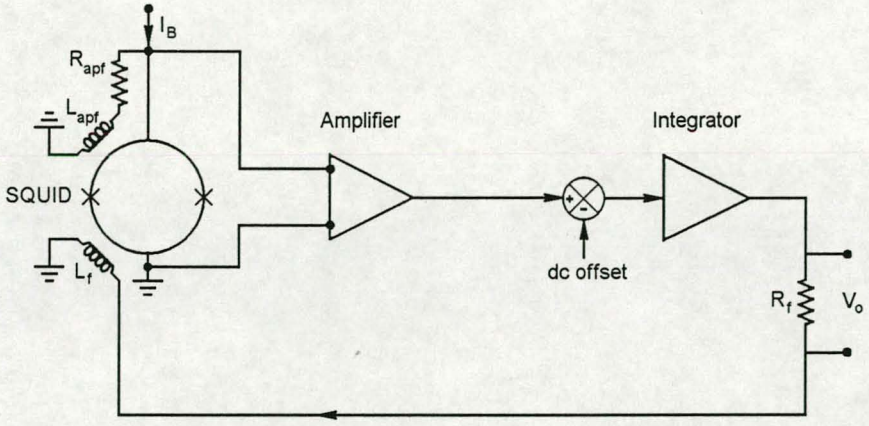

Figure 2.15 FLL with additional positive feedback.

The SQUID is shunted by a resistor connected in series with an external feedback coil as shown in Figure 2.15. If an increasing external magnetic field is applied to the SQUID, the average SQUID voltage increases initially. This couples more flux to the SQUID via the positive feedback coil, further increasing the output voltage. This means that the slope of the voltage versus flux curve ($dV/d\Phi$) can be increased dramatically. If the applied field is further increased, the SQUID output starts to decrease. However, the positive feedback prevents it from decreasing too rapidly, thus lowering $dV/d\Phi$. The average flux versus voltage curve of a SQUID with APF has a saw-tooth waveform as shown in Figure 2.16. APF is used as part of an FLL operating on the steepest part of the curve.

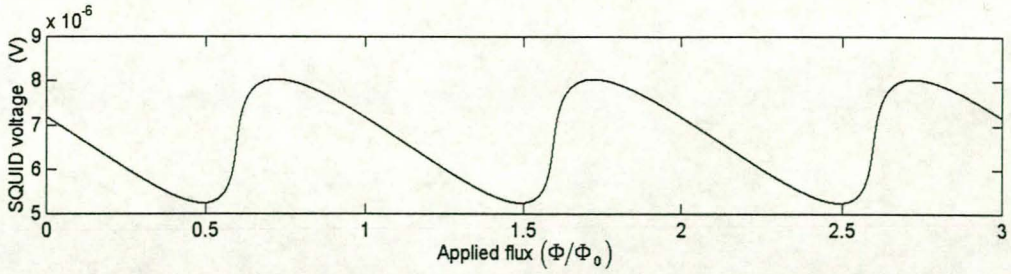

Figure 2.16 Time-averaged voltage versus flux graph of a dc SQUID using APF.

The advantage of this method is that the SQUID has a high flux-to-voltage ratio (which increases noise immunity) and large dynamic resistance. Consequently it is not necessary to use a matching transformer. Bias current feedback (BCF) is sometimes used in conjunction with APF to reduce the dynamic resistance of the SQUID at the working point. In this configuration, the bias current passes through a coupling coil before entering the SQUID. An increased bias current reduces the SQUID flux, which in turn reduces the voltage change corresponding to the original bias current change. A bias-reversal scheme can be used in conjunction with APF to reduce low-frequency noise, but this increases the complexity of the system because of the asymmetry of the waveform.

2.4 Conclusion

In this chapter, the basic equations governing Josephson junctions and SQUIDs have been introduced. Certain approximations which can be made to simplify the design and simulation of Josephson junction devices have been described. Of the various SQUID read-out schemes mentioned, the one that appears to hold the most promise is APF operating within a flux-locked loop. Its simplicity is likely to make it easier to design, construct and operate. The only drawback is that its complexity increases rapidly if it is used together with a bias-reversal scheme. If computing power permits, the full dynamic equations of the SPICE circuit model can be used to simulate the operation of the read-out electronics. However, design of these electronic circuits should only be performed once a SQUID has been fabricated and measured.

Chapter 3

Design of a directly coupled SQUID gradiometer

High-temperature superconducting devices are considerably more difficult to fabricate than those made of low-temperature superconductors. The short coherence length means that the standard tunnel junction is very difficult to fabricate with high-T_c materials [29]. In addition, the anisotropic nature of the ceramic high-temperature superconductors limits the production of multi-layer devices. High-temperature superconductors must be produced with a very pure crystal structure to obtain acceptable device performance. Even the smallest structural defects show up because of the small coherence length. In fact, deliberately created defects in the crystal structure are used to manufacture high-T_c Josephson junctions.

This chapter covers the entire design process of a SQUID gradiometer from the basics, such as the principles of high-T_c junctions and directly coupled SQUIDs, to a complete geometrical layout. The performance and electrical parameters are also estimated.

3.1 Basic concepts

3.1.1 High-temperature Josephson junctions

The earliest high-T_c Josephson junctions were produced by fabricating a thin section of superconductor from a polycrystalline film across one or more naturally occurring grain boundaries. This is shown in Figure 3.1(a). The polycrystalline film has randomly orientated grains which meet at grain boundaries of varying misorientation angles. Because of the short coherence length, grain boundaries with misorientations of more than about 10° act as Josephson junctions [30]. SQUIDs made this way suffer from excessive flux noise and hysteresis in their voltage-flux response because of the presence of grain boundaries in the SQUID loop itself [31].

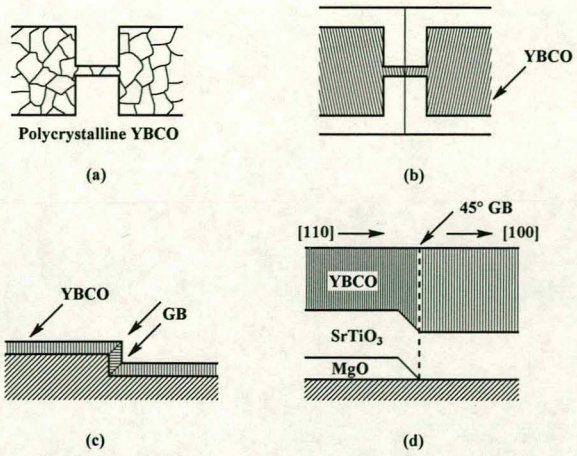

Figure 3.1 Types of high-T_c, thin-film Josephson junctions (adapted from [36]). (a) Naturally occurring grain-boundary (GB) junction and (b) bicrystal grain-boundary junction (top view). (c) Step-edge junction and (d) bi-epitaxial grain-boundary junction (side view).

The bicrystal grain-boundary junction (Figure 3.1(b)) has the advantage that there is only one grain boundary and it's position is well-defined. This is the type of junction that will be utilised as part of the SQUID gradiometer designed in this chapter. The superconductor used is $YBa_2Cu_3O_7$ (YBCO) which has a maximum critical temperature of about 92 K.

The unit cell of YBCO is orthorhombic ($a \neq b \neq c$, $\alpha = \beta = \gamma = 90°$) with $a = 0.383$, $b = 0.388$ and $c = 1.171$ nm [12]. Superconductivity in YBCO is highly anisotropic. The coherence length ($\xi_{ab} = 3.1$ nm and $\xi_c = 0.51$ nm) and the critical current density are much higher in the (001) plane than in the [001] direction [32]. For these reasons, the YBCO film must be c-axis orientated, i.e. the long axis of the unit cell must lie perpendicular to the plane of the substrate onto which it is deposited.

The gradiometer will be designed for fabrication on a 10 × 10 × 0.5 mm (100) MgO bicrystal substrate with a 24° misorientation angle. MgO substrates are not as suitable as those made of $SrTiO_3$ because their crystal structure does not match that of YBCO as closely. Their lattice mismatch with respect to YBCO is 9% as compared with the 2% of $SrTiO_3$ [33]. However, they are considerably less expensive and will be used for this reason. The 24° misorientation angle was chosen mainly because this is the most easily available and commonly used angle for MgO bicrystals. It strikes a balance between the critical current density and the normal resistance of Josephson junctions which are fabricated across the grain boundary. These two parameters respectively decrease and increase with increasing misorientation angle. MgO has a cubic unit cell ($a = b = c$, $\alpha = \beta = \gamma = 90°$) with $a = 0.4213$ nm [34]. During the deposition process, the a- and b-axes of the YBCO unit cell align themselves with the corresponding axes of the MgO unit cell. The corresponding faces of their unit cells match quite closely. The crystal structure of the substrate thus acts as a template for the growth of the YBCO crystal.

The first step in manufacturing a bicrystal substrate with a misorientation angle θ is to grow a long section of pure crystal [35]. A piece with a square cross-section of 10

× 10 mm is cut out of this such that the edge of the square forms an angle of $\theta/2$ with the a-axis of the crystal. The angle is formed about the c-axis. The resulting piece is shown in Figure 3.2(a). The c-axis of the substrate is parallel to the z-axis of the diagram. The a- and b-axes are shifted by an angle of $\theta/2$ relative to the x- and y-axes. The length in the z direction is actually much longer than shown. The block is then cut down the middle along the y-z plane and one piece rotated by 180° about the x-axis. The two pieces are fused together at high temperature and high pressure to produce a bicrystal with the two crystals misorientated by an angle θ. This is shown in Figure 3.2(b). The bicrystal is then sliced along the x-y plane to produce a number of substrates which are polished on one side.

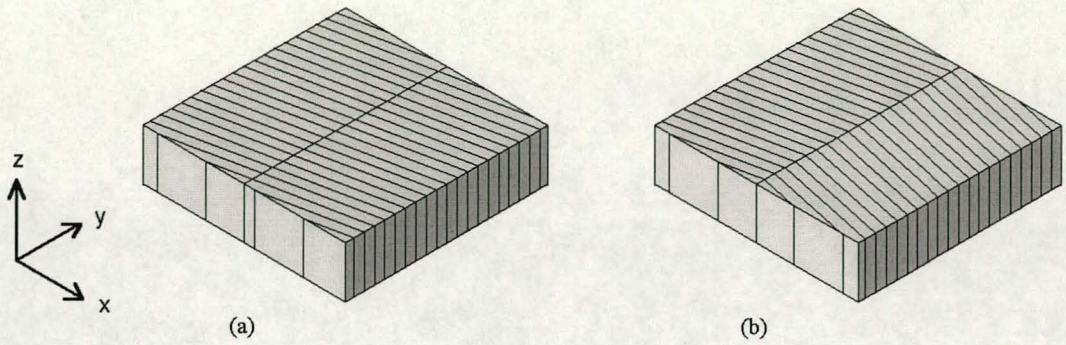

Figure 3.2 Method used to manufacture bicrystal substrates

There are a few other methods of producing high-T_c Josephson junctions. A step-edge junction, shown in Figure 3.1(c), is created by depositing a superconducting thin film across a sharp (> 45°) step which has been etched in a crystal substrate [36]. The film is a-axis orientated on the step, forming two grain boundaries with the rest of the film which is c-axis orientated.

In order to fabricate a bi-epitaxial grain-boundary junction, a thin seed layer of MgO is initially deposited on a substrate such as sapphire [31]. This is removed from part of the substrate by conventional photolithography and then a buffer layer of $SrTiO_3$ is deposited over the whole substrate. A c-axis orientated YBCO film is grown epitaxially on the $SrTiO_3$. The epitaxial directions of MgO and $SrTiO_3$ differ when deposited on r-plane sapphire. This means that a 45° grain boundary is always formed at the edges of the MgO layer. The layout of this junction is shown in Figure 3.1(d). An advantage of this method is that junctions can be fabricated at arbitrary places on the substrate, making it ideal for integrated circuits.

3.1.2 Magnetometers and gradiometers

Low-temperature SQUID magnetometers and gradiometers make use of superconducting flux transformers to couple flux from external pick-up loops of almost arbitrary shape to the SQUID itself. Since one is restricted to planar devices when using a high-T_c superconductor, a flux transformer can be fabricated on a separate substrate and glued to the SQUID chip in a flip-chip configuration.

However, there are problems with this method such as increased low-frequency noise and fabrication difficulties [37]. A solution is to connect the external pick-up loop directly to the SQUID loop. An applied magnetic field induces a current in the pick-up loop which also flows around the SQUID loop, inducing magnetic flux there. This configuration is shown in Figure 3.3(a). The SQUID loop is shown proportionally larger for clarity. In reality, its area is negligible compared with that of the pick-up loop. In the gradiometer configuration, illustrated in Figure 3.3(b), a uniform applied field causes currents to flow on the outside of the pick-up loops, effectively screening the SQUID. If a magnetic field gradient is applied, the pick-up loops are unbalanced and the SQUID is affected in the same way as for a uniform field applied to the magnetometer configuration.

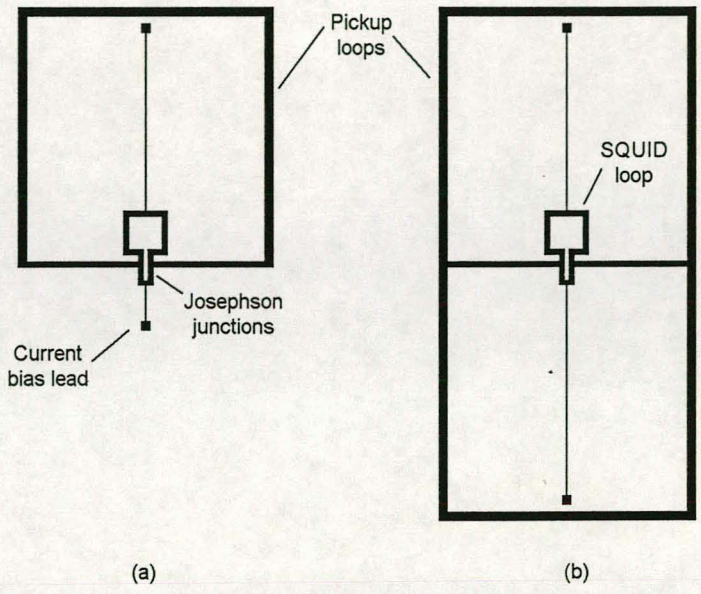

Figure 3.3 Directly coupled SQUID (a) magnetometer and (b) gradiometer (not drawn to scale).

Suppose a uniform magnetic field B_z is applied perpendicular to the plane of the magnetometer in Figure 3.3(a). The total magnetic flux intercepted by the pick-up loop of area A_p is

$$\Phi_p = B_z A_p \,. \tag{3.1}$$

A screening current (I) flows around the pick-up loop to generate an opposing flux

$$\Phi_p = L_p I \,, \tag{3.2}$$

where L_p is the inductance of the loop. This current also flows through the SQUID loop, inducing a flux

$$\Phi_{sq} = kL_{sq} I \,, \tag{3.3}$$

where k is approximately equal to the proportion of the SQUID inductance through which the current flows, and L_{sq} is the SQUID inductance. The SQUID flux can also be expressed as

$$\Phi_{sq} = B_z A_{eff} , \tag{3.4}$$

where

$$A_{eff} = \left(k \frac{A_p}{L_p} L_{sq} \right) \tag{3.5}$$

is the effective area of the SQUID. For the gradiometer configuration, a similar argument [38] can be followed to find the SQUID flux as

$$\begin{aligned} \Phi_{sq} &= \frac{\partial B_z}{\partial y}(\Delta y) k \frac{A_p}{L_p} L_{sq} \\ &= \frac{\partial B_z}{\partial y}(\Delta y) A_{eff} , \end{aligned} \tag{3.6}$$

where Δy is the gradiometer base-line, and A_p and L_p are for both sides of the pick-up loop put together. In both magnetometer configurations, the effective area A_{eff} must be maximised to increase the amount of applied flux coupled to the SQUID. This obviously increases the sensitivity of the device.

3.2 Design of a gradiometer

In this section, the dimensions of the various parts of the gradiometer are determined. These are the pick-up loop, the SQUID loop, the lines connecting the pick-up loop to the SQUID, the Josephson junctions and the feedback coils. The eventual choice of a specific dimension is usually based on a trade-off between conflicting objectives. As far as is known, there has not been an attempt in the literature to provide a complete and detailed design procedure for directly coupled SQUID magnetometers or gradiometers. Most authors concentrate on a particular aspect of SQUID design, leaving out any other details.

3.2.1 Pick-up loop

Scaling the pick-up loop's dimensions scales its inductance and area in a linear and quadratic fashion respectively. This means that making the pick-up loop as large as possible will result in a large effective area. Another way of increasing the ratio A_p/L_p is to make the width of the line forming the pick-up loop very thick [37]. Because the current flows on the inside of the loop, the inductance is quite small. The

loop area is larger than the physical hole size because of the flux-focusing effect [39]. The former method will be used here.

Leaving enough space for feedback coils, the outer dimensions of the pick-up loop are chosen as 6.6 × 8.2 mm. Ideally, the gradiometer should be able to operate effectively in an unshielded environment. This means that the pick-up loop must at least be able to carry enough current to screen out the locally uniform magnetic field of the earth. Equations 3.1 and 3.2 can be combined to give the maximum screenable magnetic field B_{max} in terms of the loop line width w as

$$B_{max} = \frac{L_P J_c w t}{A_P}. \tag{3.7}$$

The superconductor film thickness on the substrate is chosen as $t = 200$ nm, mainly because this is a typical value mentioned in the literature. A thicker film would necessitate narrower Josephson junctions which are more difficult to fabricate. A thinner film would result in increased line widths.

Formulas for the inductance of coplanar lines and single-turn rectangular planar inductors (in [40] and [41] respectively) are used to calculate the inductance of the pick-up loop. These formulas, given in Appendix B, are for normal metal inductors at low frequencies, so penetration depth is not taken into account. This is not considered a problem in view of the low accuracy required, typically 20%. The parameters of the Josephson junctions are expected to exhibit a greater variation within a single substrate.

The pick-up loop line width is chosen as 1 mm. The calculated loop inductances are then 16.5 and 17.6 nH for the respective formulas. The maximum screenable field is 0.82–0.87 G ($1\,G = 10^{-4}$ T) if the critical current density of the film is assumed to have a minimum value of $J_c = 10^5$ A/cm^2 at 77 K. This is larger than the earth's maximum magnetic field of about 0.7 G. The contour defining the area of the pick-up loop is taken in the centre of the line, giving an area of about 40 mm^2.

3.2.2 SQUID loop

The SQUID inductance must be made as large as possible to maximise the effective area. However, Enpuku et al. [42] have shown that the SQUID inductance should be less than about 200 pH to avoid significant degradation of the transfer function by thermal noise. Koelle et al. [43] have found experimentally that for $L > 40$ pH, the SQUID transfer function scales as $1/L_{sq}^{\,2}$ rather than as $1/L_{sq}$. For these reasons, the SQUID inductance is chosen as approximately 50 pH.

The SQUID inductance can be estimated by dividing it into three major parts [40],

$$L = L_{hole} + L_{par} + L_{kin}. \tag{3.8}$$

The inductance of the square hole in the SQUID centre, under the assumption that the inner diameter of the washer is smaller than its width, is

$$L_{hole} = 1.25\mu_0 d\,. \tag{3.9}$$

The inductance of two parallel coplanar lines used for the SQUID slit and legs is

$$L_{par} = \mu_0 \frac{K(k)}{K(k')} l_{par}\,, \tag{3.10}$$

where $k = \frac{s}{(s+2w)}$, $k' = \sqrt{1-k^2}$,s and w are defined as in Figure 3.4, and K is a complete elliptical integral of the first kind. The parallel line inductance is calculated separately for the various line widths along the slit, $l_{par} = l_{slit}$ and $l_{par} = l_J$. These dimensions are shown in Figure 3.4.

The kinetic inductance of the legs is estimated as

$$L_{kin} = \mu_0 \left(\frac{\lambda_L{}^2 2 l_J}{tw} \right). \tag{3.11}$$

Kinetic inductance is the contribution to the total inductance of a superconductor associated with the kinetic energy of Cooper pairs in thin sections.

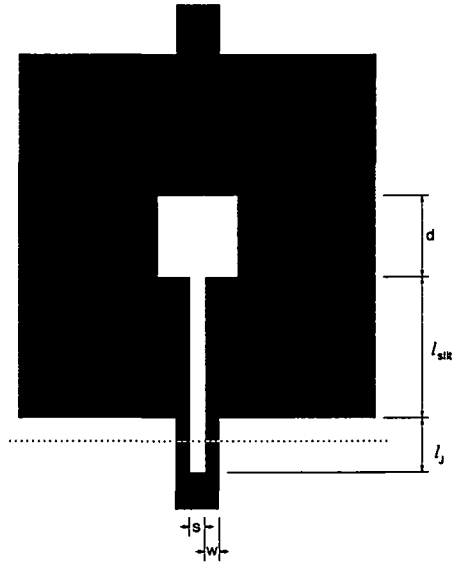

Figure 3.4 SQUID layout with symbolic dimensions.

In a directly coupled SQUID, the connections to the external pick-up loop are made on the SQUID legs. The inner and outer dimensions of the SQUID washer and the length of the SQUID legs must be adjusted to obtain the desired SQUID inductance of about 50 pH. The SQUID legs must be made as long as possible to increase the likelihood that during fabrication, the bicrystal grain boundary can be positioned to

pass through them to create the Josephson junctions. Unfortunately, an increase in leg length also increases the SQUID inductance dramatically.

The factor k, defined in Equation 3.3, is decreased by increasing the leg length. A small ratio means inefficient coupling between the pick-up loop and the SQUID, resulting in a low effective area. As a compromise, a 15 μm leg length is chosen which yields a value of $k = 0.73$. This SQUID layout is shown in Figure 3.5(a). However, this structure is difficult to fabricate without quite sophisticated equipment. For this reason, the SQUID loop has been redesigned to give the layout shown in Figure 3.5(b). It is not as efficient as the previous design, having a coupling factor of $k = 0.66$, but it is considerably easier to fabricate. The SQUID inductance is about 52 pH. The width of the coupling lines is determined in the following section.

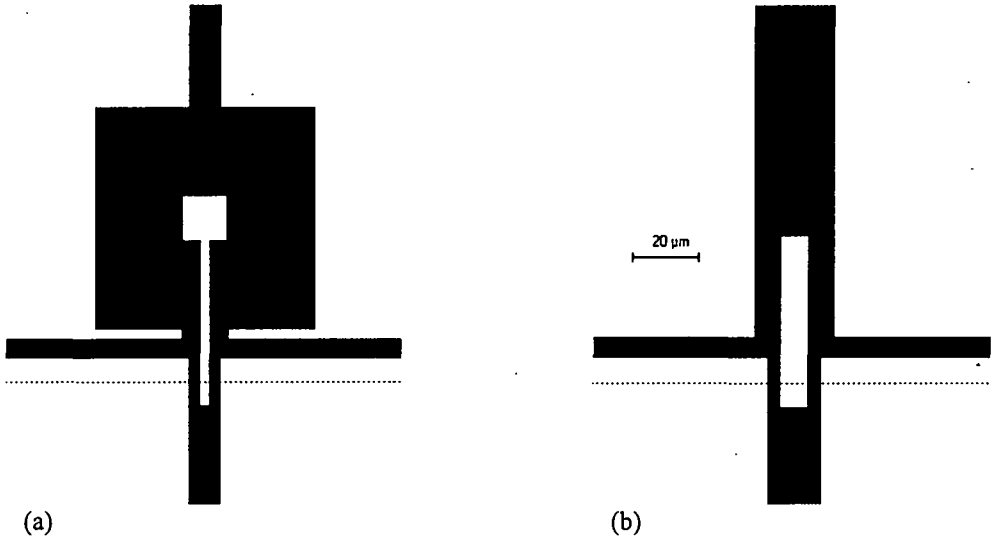

Figure 3.5 Layout of a directly coupled SQUID. (a) Original design. (b) Modified final design.

The effective area of the gradiometer can now be calculated from Equation 3.5 as $A_{eff} = 0.081\ mm^2$. If the base-line is estimated to be 3.6 mm, the flux coupled to the SQUID is approximately $\Phi_{sq} = 1.4 \times 10^5 \frac{\partial B_z}{\partial y} \Phi_0$ using Equation 3.6.

3.2.3 Connecting lines

The lines connecting the pick-up loop to the SQUID must be able to carry enough current to couple a desired field gradient to the SQUID. To calculate what this current could typically be, the source of the field gradient is taken as a current-carrying wire at a distance R from the centre of the gradiometer loop. This is shown in Figure 3.6.

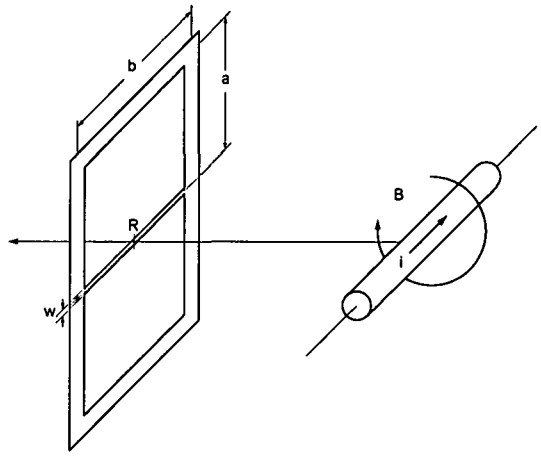

Figure 3.6 Diagram used to calculate the magnetic field, of a current-carrying wire, passing through the gradiometer.

The magnetic flux density is given by

$$B = \frac{\mu_o i}{2\pi r}. \tag{3.12}$$

from Ampere's law, where r is the distance from the centre of the conductor. Integrating over the appropriate regions gives the flux intercepted by both gradiometer loops as

$$\Phi_B = \frac{\mu_o i b}{2\pi}\left[\ln\left(\frac{R^2 + a^2}{R^2}\right)\right]. \tag{3.13}$$

The flux coupled to the SQUID will then be

$$\begin{aligned}\Phi_{sq} &= \frac{\mu_o i b L_{sq}}{\pi L_p}\left[\ln\left(\frac{R^2 + a^2}{R^2}\right)\right] \\ &= 3\,440 i \ln\left(1 + \left(\frac{0.0036}{R}\right)^2\right)\Phi_0\end{aligned} \tag{3.14}$$

for the chosen dimensions.

For a current of $i = 100$ mA at $R = 0.05$ m, $\Phi_{sq} = 1.6\Phi_0$ which is very small. If the SQUID is to be used in a flux-locked loop configuration, the SQUID flux will always be kept in the vicinity of $\pm\frac{1}{4}\Phi_0$. To test the gradiometer operation and balance, it will be necessary to operate the SQUID without feedback. For a maximum SQUID flux of $n\Phi_0$, the minimum connecting wire thickness is

$$w = \frac{n\Phi_0}{L_{sq} J_c t}. \tag{3.15}$$

A width of 6 μm is chosen which gives a maximum SQUID flux of $31\Phi_0$. Further away from the SQUID, the line must be made thicker for ease of fabrication and so that additional Josephson junctions are not created where lines cross the bicrystal grain boundary. This width is chosen to be 200 μm.

3.2.4 Josephson junction width

Vonderbeck et al. [44] obtained a Josephson critical current density of $j_c = 2\times10^4$ A/cm^2 on MgO bicrystals with a 24° misorientation angle. Values of $1-2\times10^4$ A/cm^2 have been reported on $SrTiO_3$ substrates [38, 45–47].

The coupling energy between the junctions must be made much larger than the thermal energy at 77 K [48] to enable the junctions to remain coupled in the presence of noise. Thus

$$\frac{I_c\Phi_0}{2\pi} >> k_B T \tag{3.16}$$

or $I_c >> 3.2\times10^{-6}$ A, say 30 μA. The minimum junction width is then 750 nm for a 200 nm film with j_c taken as 2×10^4 A/cm^2.

The junction width must be less than four times the Josephson penetration depth for ideal RSJ behaviour [49],

$$w \le 4\lambda_J . \tag{3.17}$$

The Josephson penetration depth is given by Nilsson [47] as

$$\lambda_J = \sqrt{\frac{\Phi_0}{2\pi\mu_0 j_c (t+2\lambda_L)}} . \tag{3.18}$$

By using a barrier thickness $t \approx 0$ for bicrystal junctions, this simplifies to

$$\lambda_J = \sqrt{\frac{\Phi_0}{4\pi\mu_0 j_c \lambda_L}} . \tag{3.19}$$

An assumption of two-fluid model dependence for $\lambda_L(T)$ gives [4]

$$\lambda_L(T) = \frac{\lambda_L(0)}{\sqrt{1-(T/T_c)^4}} . \tag{3.20}$$

Considerably differing London penetration depths are mentioned in the literature. Using $\lambda_L(0) = 140$ nm [40] in Equation 3.20, gives $\lambda_L(T = 77) = 218$ nm for $T_c = 88$ K (the expected practical value). Other values given for $\lambda_L(T = 77)$ are 145 nm [47], 300 nm [50] and 206–320 nm [51]. The penetration depth is taken to be 250 nm which is a typical value. Using Equation 3.19, $\lambda_J = 1.6$ μm and the maximum junction width is then $w_{max} = 6.5$ μm from Equation 3.17. The junction width must therefore be in the range 0.75–6.5 μm. A value of 4 μm is chosen because this is wide enough to fabricate without too much difficulty. The critical current is then $I_c = 160$ μA.

Values for the junction's normal resistance times area of $\rho_N = 0.61 \times 10^{-8}$ Ωcm^2 [44] on MgO substrates, and 10^{-8} [45] and 1.2×10^{-8} Ωcm^2 [46] on $SrTiO_3$ have been reported. The normal resistance of a 4 μm junction will be about 1.25 Ω for $\rho_N = 10^{-8}$ Ωcm^2.

3.2.5 Voltage modulation

To obtain an optimal (noise) response, the dimensionless screening parameter β_L should be close to one [52], where

$$\begin{aligned} \beta_L &= 2LI_c/\Phi_0 \\ &\approx 1. \end{aligned} \tag{3.21}$$

For the current design, $\beta_L = 8.0$ which is quite far from optimum. However, it is not practical to change it in this case for the following reasons. Reducing the critical current requires thinner Josephson junctions. Lowering the inductance, in this design, means reducing the size of the SQUID loop as well as the efficiency of the coupling between the pick-up loop and the SQUID. In addition, choosing $j_c = 1 \times 10^4$ A/cm^2, which has also been reported in the literature, halves this estimate of β_L which means that it might not be so far from optimum after all.

When the SQUID bias current is near the critical current, the voltage modulation can be estimated as [42]

$$\Delta V = \frac{7 I_c R_N}{\pi^2 (1 + \beta_L)} \left(1 - 3.57 \frac{\sqrt{k_B T L_{sq}}}{\Phi_0} \right), \tag{3.22}$$

giving $\Delta V \approx 9.3$ μV.

3.2.6 Feedback coils

The feedback loops are chosen to be 0.2 mm wide and separated by 0.2 mm from the pick-up loop. This leaves a blank strip, 0.5 mm wide, along the substrate edge. The mutual inductance between the feedback loop and one side of the pick-up loop was found by using the Maxwell 3d Parameter Extractor simulation program [53] and modelling the loop material as a perfect conductor. This value was checked by approximating the pick-up and feedback loops as two coplanar wires, infinite in length and multiplying the simulated mutual inductance per unit length by the effective distance that the lines run next to one another.

The mutual inductance found in this manner is $M = 2.5$ nH and the self-inductance of the feedback loop as $L_f = 1.6$ nH. The Parameter Extractor was also used to confirm the value estimated for the pick-up loop inductance. An effective mutual inductance between the feedback loop and the SQUID loop can be expressed as

$$M_{eff} = \frac{\partial \Phi_{sq}}{\partial I_f} = \frac{2kML_{sq}}{L_p}, \tag{3.23}$$

which is about 10.1 pH or 4.9 Φ_0/mA. The critical current of the feedback loop is 40 mA and the maximum SQUID flux that can be cancelled by feedback is then $195\Phi_0$.

The electrical parameters of the whole device are summarised in Table 3.1. The layout of the gradiometer is shown in Figure 3.7 with the finer detail of the SQUID given in Figure 3.5(b).

Table 3.1 Summary of the estimated electrical parameters of the gradiometer.

Symbol	Description	Value	Units
A_p	Area of entire pick-up loop	40	mm^2
L_p	Inductance of entire pick-up loop	17	nH
L_{sq}	Inductance of SQUID loop	52	pH
k	Coupling factor	0.66	
A_{eff}	Effective area	0.081	mm^2
Δy	Gradiometer base-line	3.6	mm
$\frac{\partial \Phi_{sq}}{\partial\left(\frac{\partial B_z}{\partial y}\right)}$	Transfer function of flux density gradient to SQUID flux	$1.4\times10^5\Phi_o$	$Wb/(T/m)$
L_f	Feedback loop inductance	1.6	nH
M	Mutual inductance between feedback coil and one half of pick-up loop	2.5	nH
M_{eff}	Effective mutual inductance between feedback loop and SQUID loop	10.1 4.9	pH Φ_0/mA
J_c	Minimum critical current density of film	10^5	A/cm^2
j_c	Critical current density of Josephson junction	2×10^4	A/cm^2
$\lambda_L(T=77)$	London penetration depth	250	nm
λ_J	Josephson penetration depth	1.6	μm
I_c	Josephson junction critical current	160	μA
$2I_c$	SQUID critical current	320	μA
R_N	Josephson junction normal resistance	1.25	Ω
β_L	Screening parameter	8.0	
ΔV	Voltage modulation depth	9.3	μV

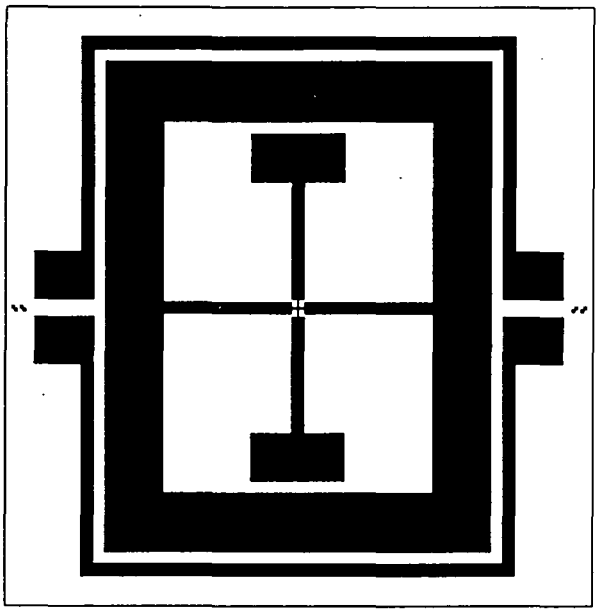

Figure 3.7 Layout of the gradiometer.

3.3 The effect of noise on YBCO dc SQUIDs

The sensitivity of a SQUID is determined by the noise it generates in the absence of any signal. There are several different types of noise which are classified according to their frequency spectra. Thermal noise and flicker noise are the most important for high-T_c SQUIDs.

3.3.1 Thermal noise

This noise, also known as Johnson or Nyquist noise, is produced by the random motion of thermally excited free electrons in a conducting medium such as a resistor. The power spectral density of thermal noise is given from thermodynamic and quantum mechanical considerations as [54]

$$S_n(f) = \frac{2h|f|}{e^{h|f|/k_BT} - 1}, \tag{3.24}$$

which is defined for negative and positive frequencies. Here h is Planck's constant and k_B is Boltzmann's constant.

This can be approximated as

$$S_n(f) = 2k_BT \tag{3.25}$$

for $f << k_BT/h$, i.e. $f << 1.6$ THz at 77 K and $f << 88$ GHz at 4.2 K. This means that it is a good approximation for most applications.

By integrating over the bandwidth of interest B, the mean-square voltage and current respectively in a resistor R can be calculated as [55]

$$\left\langle v_n^{\,2}(t)\right\rangle = 4k_B TBR \tag{3.26}$$

and

$$\left\langle i_n^{\,2}(t)\right\rangle = 4k_B TB/R\,. \tag{3.27}$$

The voltage and current spectral densities are then

$$S_V(f) = \frac{\left\langle v_n^{\,2}(t)\right\rangle}{B} = 4k_B TR \tag{3.28}$$

and

$$S_I(f) = \frac{\left\langle i_n^{\,2}(t)\right\rangle}{B} = 4k_B T/R\,, \tag{3.29}$$

which are defined for positive frequencies only.

In the RSJ SQUID model, the noise is produced in the normal resistances of the junctions. To complete the model, noise current sources, each with the spectral density of Equation 3.29 should be placed in parallel with the normal resistances. The resulting voltage noise spectral density at the terminals of the SQUID can be found for low frequencies, $\omega << R_N/L_{sq}$ (i.e. $f << 4$ GHz for the design of this chapter), by summing the contributions of the parallel and circulating currents to give [17]

$$S_V(f) = \left(2R_d^{\,2} + \frac{L_{sq}^{\,2}}{2}V_\Phi^{\,2}\right)S_I(f)\,, \tag{3.30}$$

where $R_d = \dfrac{\partial V_{sq}}{\partial I_{sq}}$ is the dynamic resistance of the SQUID as seen from its terminals and $V_\Phi = \dfrac{\partial V}{\partial \Phi}$ is the flux-to-voltage transfer function of the SQUID.

The first term can be regarded as the spectral density of the voltage noise across the SQUID and the second term, the spectral density of the flux noise in the SQUID loop. In the limit of zero SQUID transfer function, the noise is just that of a single junction of dynamic resistance $\sqrt{2}R_d$. The second term is a maximum when $\Phi_{sq} = \frac{1}{2}\left(n+\frac{1}{2}\right)\Phi_0$ and zero when $\Phi_{sq} = \frac{1}{2}n\Phi_0$. This allows one to determine the dominant noise source experimentally by varying the applied flux at a fixed bias current.

The mean-square magnetic flux noise is related to the mean-square voltage noise by the applied flux-to-voltage transfer function of the SQUID [17], that is

$$S_\Phi(f) = \frac{S_V(f)}{V_\Phi^{\,2}}. \tag{3.31}$$

The energy resolution, which is often used as a measure of a dc SQUID's noise performance, can be written as

$$\begin{aligned}\varepsilon(f) &= \frac{S_\Phi(f)}{2L_{sq}} \\ &= \frac{S_V(f)}{2L_{sq}V_\Phi^{\,2}}.\end{aligned} \tag{3.32}$$

The energy resolution is limited by the Heisenberg uncertainty principle to a minimum of $\hbar$. Substituting Equations 3.29 and 3.30 into Equation 3.32 gives

$$\varepsilon(f) = \frac{2k_BT}{L_{sq}V_\Phi^{\,2}R_N}\left(2R_d^{\,2} + \frac{L_{sq}^{\,2}}{2}V_\Phi^{\,2}\right). \tag{3.33}$$

It has been found by numerical simulation [56] that the energy resolution of an optimised dc SQUID ($\beta_L \approx 1$), operated where its transfer function is maximised, is

$$\varepsilon(f) \approx \frac{9k_BTL_{sq}}{R_N}. \tag{3.34}$$

This can also be obtained from Equation 3.33 by making the approximations $R_d \approx R_N/\sqrt{2}$ and $\frac{\partial V}{\partial \Phi} = R_N/2L_{sq}$.

The spectral density of the SQUID voltage noise has been found by simulation to be [57]

$$S_V(f) \approx 16k_BTR. \tag{3.35}$$

This is a factor of 8 more than would be obtained using Equation 3.28 if the SQUID were merely modelled as two parallel resistors for this calculation. This means that although the noise is only generated in the resistive parts of the SQUID, the total voltage noise cannot be found without viewing the SQUID as a whole.

Determining the sensitivity of the gradiometer

The SQUID parameters $I_c = 160\ \mu A$, $L_{sq} = 52$ pH, $R_N = 1.25\ \Omega$ and $\beta_L = 8.0$ are used to estimate the sensitivity of the gradiometer designed in the previous section.

The energy resolution at 77 K is calculated as $\varepsilon(f) = 3.98 \times 10^{-31}$ J/Hz by using Equation 3.34. The mean-square flux noise can be determined as $S_\Phi(f) = 4.14 \times 10^{-41}$ Wb^2/Hz by substituting this value into Equation 3.32. The flux noise is often expressed in the form $\sqrt{S_\Phi(f)} = 3.11 \times 10^{-6}$ $\Phi_0/\sqrt{Hz}$. The mean-square voltage noise can be obtained from the mean-square flux noise with Equation 3.31 if the SQUID transfer function is known.

There are a number of different formulas for the transfer function. Enpuku et al. [42] find that

$$V_\Phi = 4\frac{I_c R_N}{\Phi_0(1+\beta)}\left(1 - 3.57\frac{\sqrt{k_B T L_{sq}}}{\Phi_0}\right)$$
$$= \frac{4\pi^2}{7\Phi_0}\Delta V \qquad (3.36)$$

and Clarke [57] finds that

$$V_\Phi = \frac{R_N}{L_{sq}}. \qquad (3.37)$$

If the voltage flux response is assumed to be sinusoidal, one obtains

$$V_\Phi = \frac{\pi}{\Phi_0}\Delta V. \qquad (3.38)$$

Equations (3.36), (3.37) and (3.38) give 52.8, 49.8 and 29.4 $\mu V/\Phi_0$ respectively. Equations 3.36 and 3.37 agree within 10% but Equation 3.38 is about half the value, probably because it is derived under the assumption that the SQUID response is sinusoidal. Using the first two values in Equation 3.31, the mean-square SQUID voltage $S_V(f)$ is obtained as 2.70×10^{-20} and 2.39×10^{-20} V^2/Hz. Calculating $S_V(f)$ using Equation 3.35 gives 2.13×10^{-20} V^2/Hz at 77 K which is very similar, showing that the noise equations given above are at least more or less consistent with one another.

From the mean-square flux noise, the mean-square field gradient noise can be estimated as

$$S_{\frac{\partial B}{\partial y}}(f) = \frac{S_\Phi(f)}{\left(\frac{\partial \Phi_{sq}}{\partial\left(\frac{\partial B_z}{\partial y}\right)}\right)^2}. \qquad (3.39)$$

The parameters relevant to the noise performance of the gradiometer are listed in Table 3.2.

Table 3.2 Summary of the estimated noise parameters of the gradiometer at 77 K.

Symbol	Description	Value	Units
$\varepsilon(f)$	Energy resolution	3.98×10^{-31}	J/Hz
V_Φ	SQUID flux to voltage transfer function	49.8	$\mu V/\Phi_0$
$\sqrt{S_\Phi(f)}$	Magnetic flux noise	3.11×10^{-6}	$\Phi_0/\sqrt{Hz}$
$\sqrt{S_{\frac{\partial B}{\partial y}}(f)}$	Magnetic field gradient noise	22.2	$(pT/m)/\sqrt{Hz}$
$\sqrt{S_V(f)}$	Voltage noise	1.6×10^{-10}	$V/\sqrt{Hz}$

Good measured values for the energy resolution are usually in the range $1-10\times10^{-30}$ J/Hz, with one report as low as 2×10^{-31} J/Hz [37]. Corresponding values for magnetic flux noise range from 10^{-6} to 10^{-4} $\Phi_0/\sqrt{Hz}$. The magnetic field gradient noise is usually in the range $50-100\,(pT/m)/\sqrt{Hz}$. In comparison, the estimated parameters in the table appear quite good. However, measured values are usually quite a bit worse than the predictions. In addition, flicker noise (discussed in the next section) usually dominates the thermal noise by several orders of magnitude.

3.3.2 1/f noise

This noise, also known as flicker noise, dominates at low frequencies and its magnitude is inversely proportional to the operating frequency. Its origin is not completely understood. It can arise from a number of mechanisms, namely critical current and normal resistance fluctuations, and the motion of magnetic flux quanta in the SQUID body [17, 49, 58–63].

Critical current and resistance fluctuations

The dominant mechanism responsible for 1/f noise is normally fluctuations in the critical currents and normal resistances of the Josephson junctions [49, 59].

The critical current fluctuations in high-T_c bicrystal grain-boundary junctions are caused by localised defect states in the insulating grain-boundary barrier with fluctuating electron occupation [59, 61]. As electron trapping sites in the grain-boundary barrier fill and empty, the local value of the critical current density around each trapping site changes [58]. This is similar to what happens in the dielectric of low-T_c tunnel junctions [61], except that in this case there is a much greater density of trapping sites [60]. Annealing the device in oxygen reduces the number of trapping sites at the grain boundary.

An increase of barrier height by charge trapping causes a decrease of I_c and simultaneously an increase of R_N which means that the changes in I_c and R_N are anti-phase correlated [61].

If the voltage noise $S_V^{1/2}$ of a single junction is measured as a function of bias current, it initially increases very rapidly to a sharp peak at $I_b \approx I_c$. After decreasing to a local minimum, it increases linearly with increasing bias current. The noise peak is ascribed to the effect of the critical current fluctuations and the linear region to resistance fluctuations [60, 61, 63]. This is logical since below the average critical current, a voltage cannot be produced unless the critical current momentarily drops below the level of the bias current. Well above the average critical current, changes in the critical current should not affect the junction voltage. However, normal resistance fluctuations change the gradient of the voltage-current curve. The normalised fluctuation of the critical current and normal resistance are almost independent of temperature and misorientation angle [61].

Apparent flux noise

Flux noise is another source of 1/f noise. Its effect is that of a fluctuation in the applied flux, from which it cannot be distinguished [58]. It is believed to be caused by the thermally activated motion of flux quanta trapped in the SQUID body [59]. This changes the exact flux applied to the SQUID [58]. Its contribution to the total 1/f noise increases with temperature, dominating close to T_c [17, 60, 62]. However, its effect on a bare SQUID is usually very small at 77 K.

In superconducting YBCO thin-film samples, the magnitude of 1/f noise attributed to magnetic flux motion depends strongly on the microstructure of the samples [62]. The noise magnitude is also highly anisotropic, being much larger for currents parallel to the c-axis than in the a-b plane. This is especially important in the transition region $T \approx T_c$. Highly orientated thin films are required for practical applications if a high level of 1/f noise is to be avoided.

General

The magnitude of the 1/f noise in a GBJ SQUID is very close to that of a single Josephson junction, showing that the source of noise is probably in the junctions themselves [17]. The theory for predicting 1/f noise is not very well developed at present and the noise performance is highly dependent on film quality, especially the formation of a- and b-axis orientated particles [59]. Figure 3.8, taken from [17], gives some typical levels of low-frequency noise.

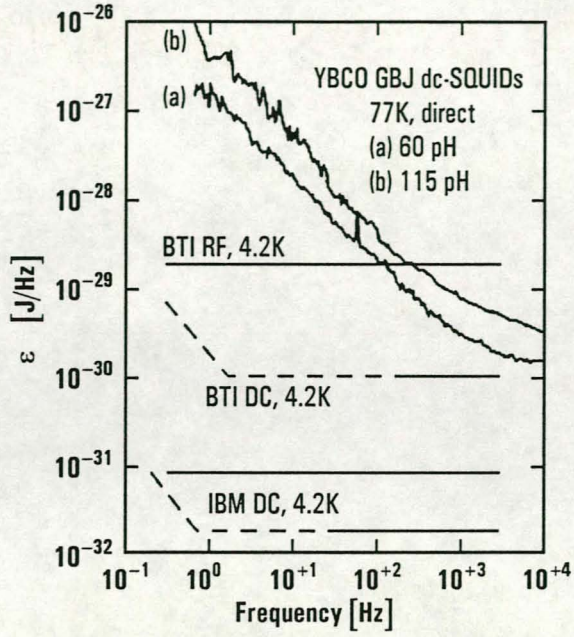

Figure 3.8 Measured energy resolution of 60 and 115 pH GBJ dc SQUIDs at 77 K [17]. For comparison, the energy resolution of low-temperature, commercial rf and dc SQUIDs is also shown. The data for SQUIDs using modulations schemes to reduce low-frequency noise is shown as dashed.

An effective method to minimise 1/f noise is to reverse-bias the SQUID. This involves changing the direction of the biasing current at a rate of 100 Hz – 10 kHz. This cannot, however, remove apparent flux noise since it is impossible to distinguish from a true applied flux signal [58, 63]. In the flux-locked loop configuration, the bias flux can also be modulated.

Ac biasing reduces the 1/f noise that is assumed to result from the out-of-phase critical current fluctuations of the two junctions [64]. This method does have some disadvantages. The digital circuits necessary for bias-reversal increase flux noise. In addition, when the SQUID's junctions do not have equal critical currents, ac biasing increases the white noise level because the operating points of the SQUID are no longer symmetrical.

3.4 Conclusion

This chapter introduces directly coupled SQUID magnetometers and gradiometers. A design procedure which takes care of the most important considerations has been developed with the use of the relevant literature. This procedure has been used to design a gradiometer and estimate its electrical parameters. The design has been modified to allow for fabrication difficulties.

The theory for the estimation of thermal noise is well developed and is used in the same way as for low-temperature SQUIDs. However, 1/f noise dominates at low frequencies, in the region where the SQUID is most likely to be used. Its origin is not completely understood and its contribution is difficult to predict, especially since it is so dependent on film quality.

Chapter 4

Superconducting device fabrication

4.1 Introduction

The fabrication of a SQUID gradiometer was initially thought to be a relatively simple task. In principle, the processes involved are not complicated but the infrastructure needed to make such small structures easily did not exist. This included a lack of practical knowledge and experience, and the fact that very little up-to-date equipment was available. This meant that it was necessary to figure out many of the processes almost from scratch and that the limits on the processes had to be pushed as far as possible. The optimisation of the fabrication process became a major part of the work undertaken.

The entire fabrication process can be summarised briefly as follows. An YBCO film is deposited onto a bicrystal substrate by pulsed laser deposition. The film is fashioned into the desired shape by photolithography and wet etching. Gold contact pads are laser-deposited on top of the YBCO and these are wire-bonded to an external printed circuit board (PCB) for testing.

4.2 Deposition of the YBCO film

4.2.1 A very simplified description of pulsed laser deposition

There are a number of ways of depositing YBCO thin films, such as evaporation, dc and rf sputtering, and pulsed laser deposition (PLD). Pulsed laser deposition, which is also known as laser ablation, is used here since such a system is available. It has been used in the past specifically for depositing YBCO films with a reasonable degree of success [14, 15]. A pulsed excimer laser is focused onto a target (e.g. YBCO) inside a vacuum chamber. A plume of particles expands outwards from the heated area on the target and deposits onto a substrate which is fixed a short distance away. The film is built up layer by layer on the substrate, each time the laser is pulsed. The configuration of the PLD system is shown in Figure 4.1. The laser beam comes in at about 45° with respect to the target surface and the axis of the plume is directed at more or less 90°.

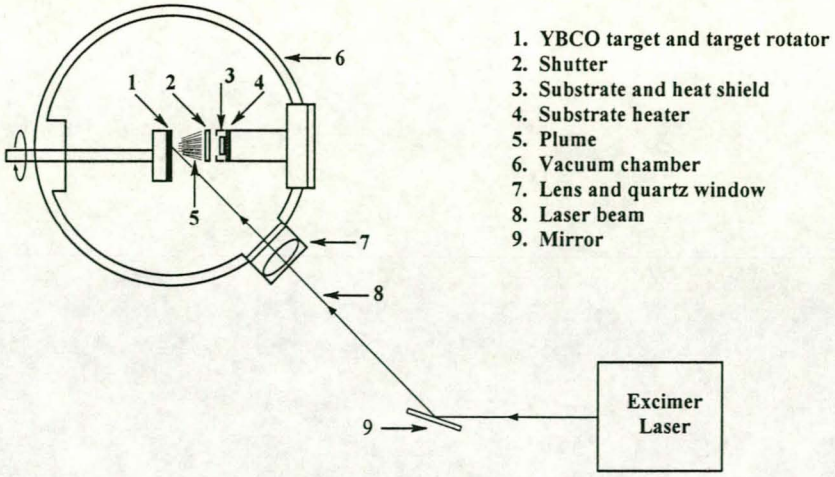

Figure 4.1 The configuration of the pulsed laser deposition system.

4.2.2 The use of the pulsed laser deposition system of the National Accelerator Centre to deposit superconducting thin films

This system was originally developed at the National Accelerator Centre (NAC) by Maritz et al. [14] in 1995. He used it to deposit YBCO films on a number of different substrate materials including MgO and $SrTiO_3$.

The laser presently in use is a XeCl excimer laser (Lambda Physik EMG 203 MSC) which can produce pulse energies of up to 300 mJ. Each pulse is approximately 30 nS in duration. The pulse repetition rate can be set up to 100 Hz although it is normally kept at 10 Hz for depositions. Most of the beam's energy lies in the ultraviolet part of the spectrum (308 nm) although it also contains enough longer wavelength light to make it visible. Ultraviolet lasers are desirable for laser ablation because they produce much better quality films than lasers with longer wavelengths [65].

The pulse energy is measured with a pyro-electric detector in conjunction with an oscilloscope. Because the detector has a large time constant, the energy is always measured at 2 Hz. It is assumed that the energy does not differ substantially at 10 Hz. The output energy can be controlled to a limited extent by varying the laser's supply voltage in the range 18–25 kV. If this voltage is reduced below the lower limit, the energy becomes irregular, changing from pulse to pulse. Too low a voltage can also cause corrosion of the laser electrodes.

From the laser, the beam is reflected off a mirror after which it passes through the lens and window of the chamber. The beam is focused to a small spot on the target. The position of the lens determines the spot size.

The target material is mounted in a steel holder and held in place by small screws. This holder, in turn, is attached to a carousel with space for a total of six targets. The active target can be changed under computer control, allowing one the option of depositing a series of different materials without breaking vacuum. The removal of a steel lid on top of the chamber permits access to the targets.

The shutter, heat shield, substrate and substrate heater are mounted together on the heater assembly which slides out horizontally. The substrate is attached to the substrate heater with conductive silver paint to ensure good thermal contact. Poor thermal contact can cause poor and unrepeatable results. The vacuum chamber is sealed with rubber O-rings. In addition the heater assembly is tightened with bolts but the top lid is aided only by gravity. Vacuum grease is not used on the seals to avoid any possible contamination. The chamber is evacuated overnight to a pressure of around 2×10^{-6} mbar with two turbo-molecular pumps which are used in conjunction with a rotary vane pump. This is done to remove any possible contaminants such as atmospheric humidity and solvents in the silver paint. During deposition, only one of the turbo-molecular pumps is used and it pumps through a bypass. Oxygen is bled into the chamber through a finely adjustable needle valve which is used to adjust the pressure to the desired level. The substrate is maintained at the correct temperature by the substrate heater which contains a coaxial heating element. A K-type thermocouple provides the temperature read-out and a variac allows manual adjustment of the temperature. A heat shield is placed over the substrate and heater. It has a hole in its centre to allow the plume to pass through it to the substrate. The heat shield is necessary to maintain the substrate at a constant temperature and it also helps reduce the time taken to heat the substrate and prevents unnecessary heating of other parts of the chamber.

If the laser beam continually hit the target in one place, it would burn a hole. This could pull the plume off-centre by as much as 20° and cause unwanted boulder formation on the substrate instead of the desired epitaxial growth [15]. To prevent this, the target is rotated by a stepper motor, sweeping a circular band of the target surface into the path of the beam. After each deposition, the target must be resurfaced with sandpaper to expose a fresh layer of material. In addition, a pre-ablation of a minute or two should be performed just prior to deposition to remove any impurities on the target surface and dislodge any large loose particles. To start the deposition, the shutter is opened which allows the plume to come into contact with the substrate. Two windows, one on the lid and the other on the side of the chamber, allow one to check the horizontal and vertical alignment respectively of the plume. This must be done every time a deposition is performed. If necessary, the alignment can be adjusted in one of two ways. To correct small misalignments, it is possible to change the angle of the mirror slightly. Care must be taken that the beam still passes through the centre of the lens. If larger adjustments are necessary, the entire vacuum chamber must be shifted about its central axis. A more comprehensive description of how to operate the system is given in Appendix D5. A photograph of the PLD system is given in Figure 4.2 together with a close-up of the interior of the vacuum chamber.

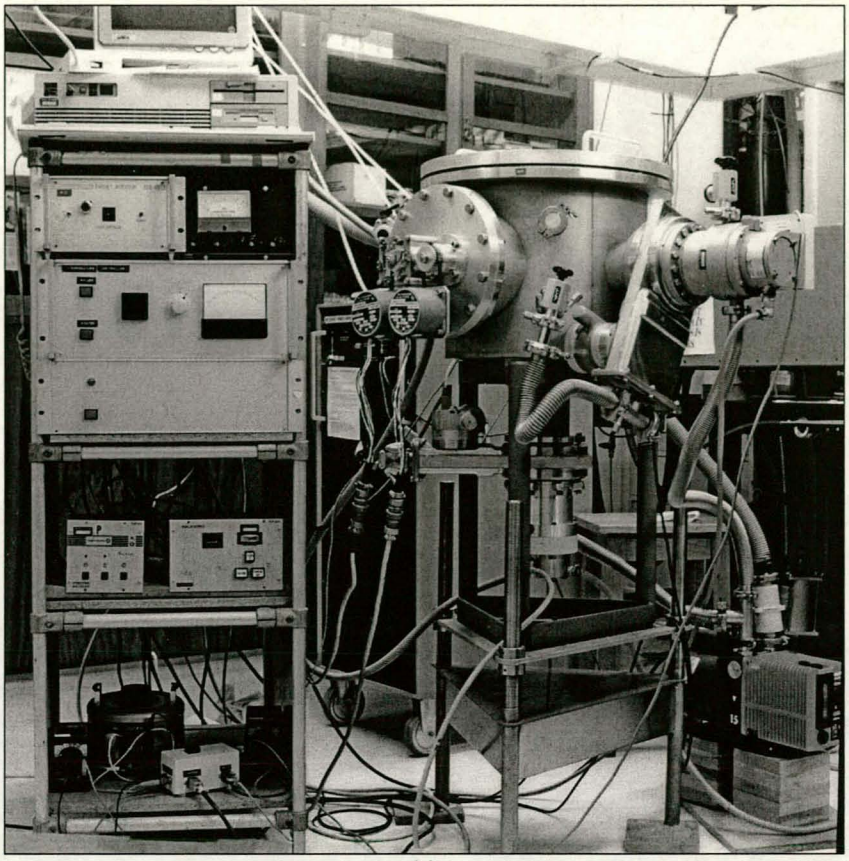

(a)

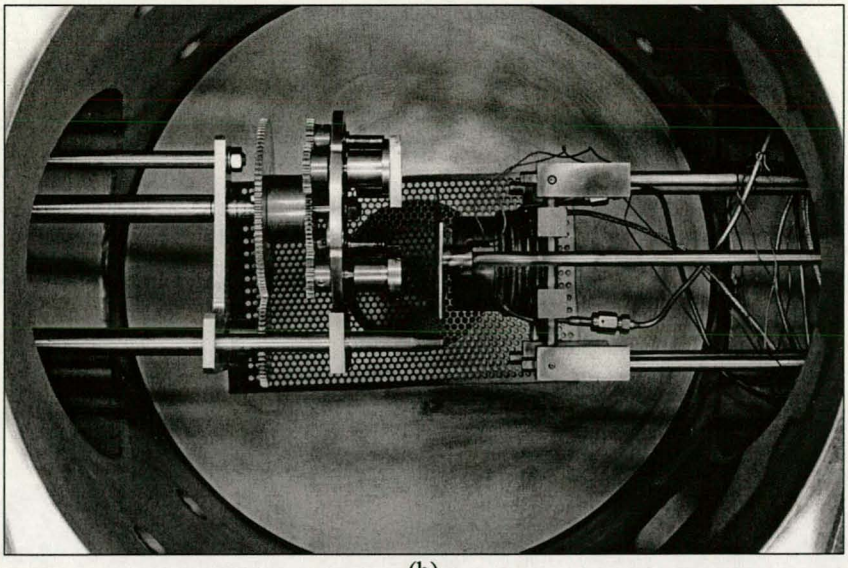

(b)

Figure 4.2 Photograph of the NAC pulsed laser deposition system. (a) The vacuum chamber with its associated pumps and valves. The control rack is on the left. (b) The chamber as viewed from above with the lid removed. The target carousel and its gearing are on the left. The heater assembly with the shutter (in the closed position) and heat shield can be seen on the right. The opening where the laser enters the chamber is at the bottom right.

4.2.3 Methods for characterising superconducting thin films

Good superconducting films have high critical temperatures, high critical currents, good surface morphology and a c-axis orientated crystal structure. Four measurement types are described here, namely resistivity and permeability measurements, RBS analysis and AFM scanning. These measurements are used to characterise a deposited film, enabling one to select the best deposition parameter set. Another measurement not mentioned here which can provide useful information is X-ray diffraction. This can determine whether the crystal structure of the film is c-axis orientated. However, this is usually the case given good resistivity and permeability measurements.

The first two measurements, which are used to measure the temperature properties of a superconductor, are carried out in a cryo-cooler. The operation of the cryo-cooler is as follows. A water-cooled refrigeration unit compresses helium which is piped to a heat exchanger in the cryo-cooler itself. A cold-finger equipped with a platinum-wire temperature sensor can reach temperatures as low as 10 K. A computer with an A/D converter is used to gather experimental data, namely voltage as a function of temperature. Every measurement is performed twice, once on cooling down and once on warming up. The two measurements are then plotted together on the same set of axes. If they correspond to within 1 K, the measurement is deemed to be sufficiently accurate. A vacuum maintained by a rotary vane pump thermally isolates the cryo-cooler's cold-finger from the outside. Good measurements are usually obtained if the pressure is reduced to about 2×10^{-2} mbar before cooling down begins. This value is almost the lowest that can be obtained with the existing vacuum pump. If higher starting pressures are used, the cool-down and warm-up curves are likely to exhibit significant hysteresis.

The biggest problem encountered when performing these measurements is the erratic behaviour of the temperature sensor. This is probably due to poor thermal contact and is worsened by the fact that the sensor is prone to self-heating effects. Good thermal contact is also important between the substrate and cold-finger but this is less likely to be a problem because of the flat shape of the contact surfaces. Thermal contact is established with vacuum grease. Although not designed to be thermally conductive, it is more effective than heat-sink paste, maintaining its flexibility at low temperatures and pressures.

Resistivity measurement

A four-point resistivity measurement is performed on the film by attaching fine copper wires to its corners with conductive silver paint. Two adjacent wires are used to bias the film with a small dc current (typically 10 mA) and the other wires are used to read out the resulting voltage. The voltage (representing resistivity) is plotted as a function of the temperature. Such a resistivity graph is given in Figure 4.3.

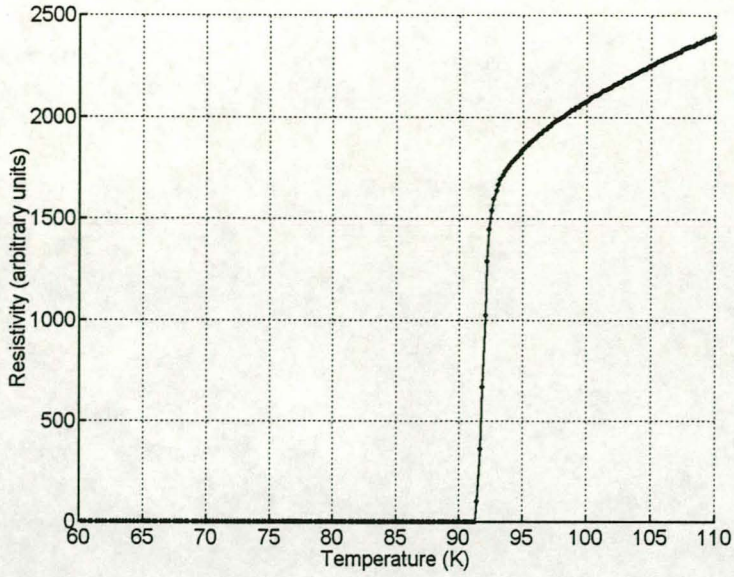

Figure 4.3 The resistivity graph of a commercial YBCO thin film.

The most important parameter obtained from the graph is the critical temperature T_c. Since the behaviour of the film is not ideal and there is a finite transition width, some sort of convention must be decided upon to define the critical temperature. The linear part of the curve above the critical temperature can be extended down to the left until it meets a line which is drawn tangential to the near-vertical part of the curve. The resistivity value of the intercept point is noted. The temperatures corresponding to 10% and 90% of this value on the resistivity curve are noted as T_1 and T_2 respectively. The critical or transition temperature is then defined as

$$T_c = \frac{(T_1 + T_2)}{2} \tag{4.1}$$

and the transition width as

$$\Delta = T_2 - T_1 . \tag{4.2}$$

A high transition temperature usually indicates a high quality film. A narrow transition width is associated with film homogeneity.

A drawback of using resistivity to characterise superconductors is that it is a best-case measurement. The current flows along the path of least resistance, showing a film to be of good quality if there is the smallest of superconducting paths. Although the silver paint used for the contacts causes minimal surface damage and can mostly be removed with acetone or methanol, a resistivity measurement should not be performed on a sample destined for etching. Small pieces of silver from the paint often find their way onto other parts of the film, causing photoresist adhesion problems. It should be mentioned that although this measurement is conceptually simple and needs relatively simple read-out electronics, it can sometimes be tricky to make good and reliable contact with the film surface. If older silver paint is used or too thick a layer is applied, electrical contact can be broken at a critical time, say

below 150 K. This means that sample has to be raised to room temperature before the offending contact can be repaired. Occasionally, making and breaking of contact occurs at the same temperature on both warm-up and cool-down curves, producing a measurement which at first glance appears plausible.

Permeability measurement

This measurement approximately relates the magnetic flux density B inside the superconductor to the imposed magnetic field intensity H. The sample is placed on top of a small spiral coil attached to the cold-finger of the cryo-cooler. This coil is driven by an ac current of the order of 100 mA. The frequency can be varied between 1 kHz and 100 kHz. A small pick-up coil is positioned directly above the film without touching it. This detects the magnitude of the magnetic flux passing through the film. Initially, the cryo-cooler could only be used to perform resistivity measurements. An amplifier and precision rectifier were constructed which convert the ac voltage output to a dc value. This can be logged by the existing data-acquisition system. The relevant parts of the measurement set-up are shown in Figure 4.4.

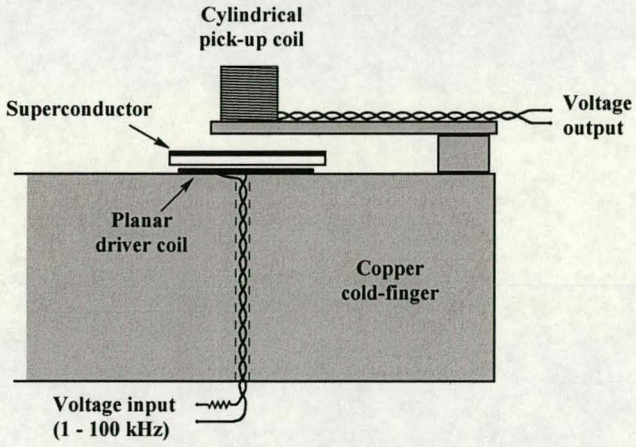

Figure 4.4 The experimental set-up for a permeability measurement.

The measurement can be interpreted in two ways. It can be regarded as the degree to which the Meissner effect is able to expel magnetic fields, or as the ability of the film to support circulating currents which oppose an applied field. A permeability measurement provides a more realistic reflection of the film quality than one of resistivity since it makes a measurement over a larger area. If a small section of the film is defective, the measurement is likely to reflect this since the circulating currents must flow in a certain way to counteract the applied field effectively. The start of the transition is almost always at a lower temperature than for resistivity measurements but the general shape of the curve is approximately the same. The permeability curve corresponding to the resistivity measurement of Figure 4.3 is given in Figure 4.5.

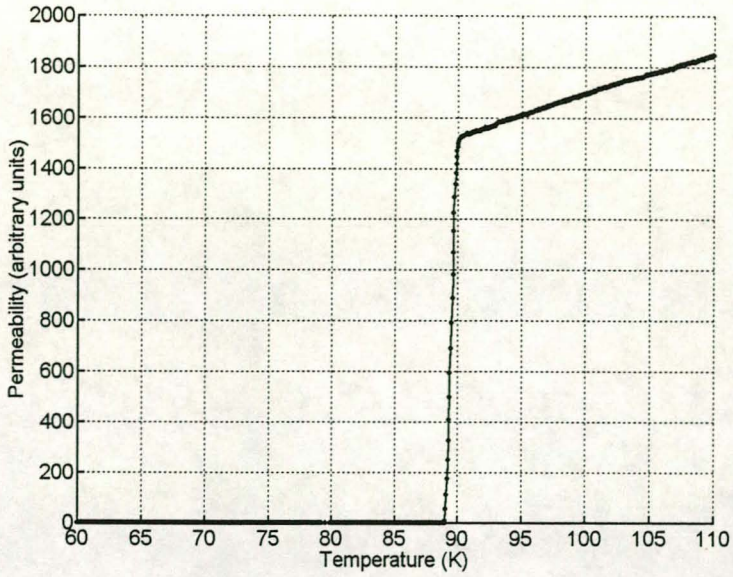

Figure 4.5 The permeability graph of a commercial YBCO thin film.

The transition width is not as meaningful as in the case of the resistivity measurement where the resistance is identically zero at some point below the transition temperature. Here, the ability of the film to support sufficiently large currents to screen out the applied field continues to improve, even far below the transition temperature. It is therefore the start of the transition which is more important. A problem with this measurement type is that the transition temperature is highly dependent on the magnitude of the applied field. Smaller applied fields produce higher transition temperatures. Thicker films show the same discrepancy, even if the film quality is the same. The major advantage of a permeability measurement is that it is completely non-destructive. In addition, it is easy to perform since no electrical connections to the film are necessary.

Rutherford backscattering spectrometry (RBS)

The film is placed in a vacuum and bombarded with beam of mono-energetic charged particles, in this case alpha particles. The particle beam produced by the Van der Graaf accelerator at NAC is collimated by electromagnets to a cross-sectional area of about 2 × 2 mm. Low beam currents are used to limit damage to the film. When low energies (typically in the range 2–4 MeV) are used in order to avoid nuclear reactions, the collisions with the film's atomic nuclei are elastic [15]. The particles scattering off heavier elements have higher energies than those off the lighter elements. Heavy atoms also have a larger scattering cross-section since they have large nuclei. The numbers of backscattered particles at the various energies are recorded, enabling one to produce a Rutherford backscattering spectrum.

RUMP [66] is a software package which simulates the Rutherford backscattering spectrum for the beam parameters of the actual experiment*. The structure of the film is entered as a series of layers of various chemical compositions. RUMP allows one to plot the simulated and measured data on the same graph for comparison. Such a graph for an YBCO thin film on an MgO substrate is given in Figure 4.6.

The individual chemical elements of the film each contribute a roughly rectangular pulse of varying amplitude to the spectrum. The sum of these pulses produces the staircase pattern of Figure 4.6. Moving from right to left, the first step is the contribution of the heaviest element Ba. The next is the sum of the contributions of Ba and Y, and so it continues towards the lighter elements. When the energy is below the lower limit for a specific element in the film, a reducing staircase pattern is obtained. The thicker the film, the wider the individual spectral pulse and thus the larger the range of energies over which a specific element will contribute to the spectrum.

* According to the operating manual, the name RUMP can stand for practically anything, including "Rutherford Universal Manipulation Program", "Random Utility for Making Pictures", "Rather Unusual Masochistic Package" and "Really Ugly and Mangled Procrastination tool"!

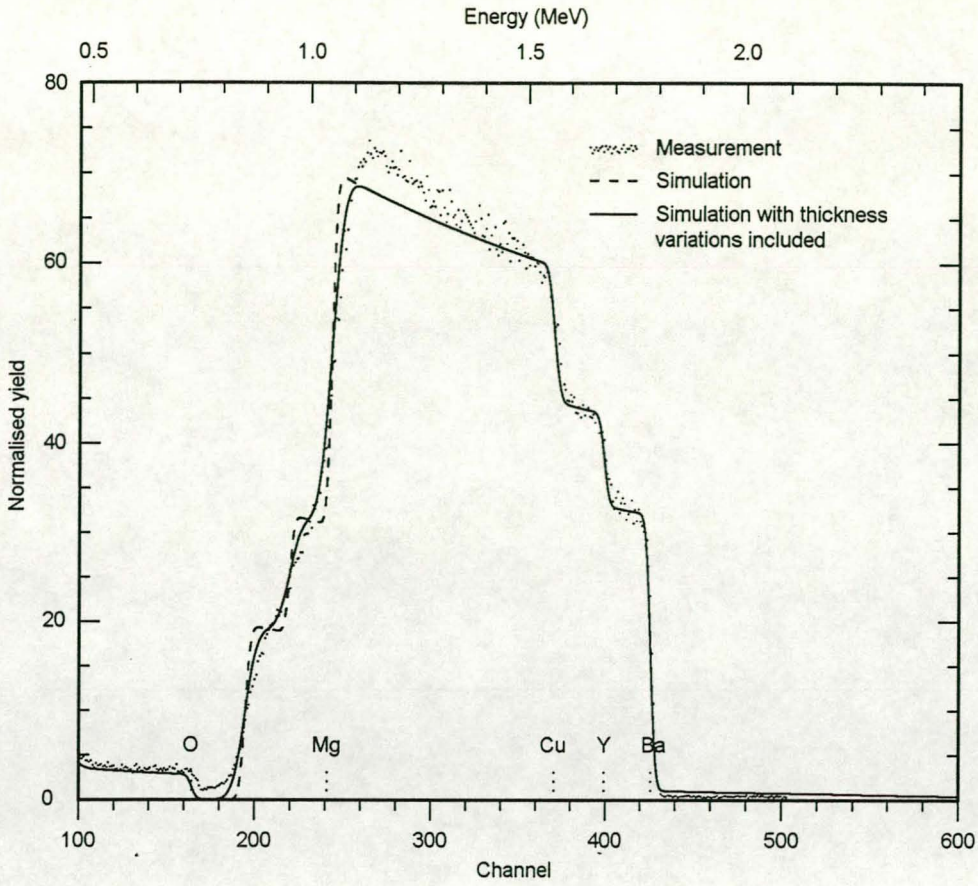

Figure 4.6 RBS spectrum of an YBCO thin film deposited on an MgO substrate. The simulation shows a better fit to the experimental data if variation in film thickness is taken into account. The elements contributing to the steps in the pattern are indicated at the appropriate positions along the energy (channel) axis. The alpha particle beam used for the measurement had particle energies of 2 MeV and a total charge of 20 μC at 127 nA. Each channel is associated with an energy variation of about 4 keV.

For each batch of measurements, an iridium-silicon standard is measured. It has well-defined spectral peaks which allow one to normalise the experimental measurements to coincide with the theoretical spectrum. The film thickness and chemical composition are varied in simulation until the experimental and simulated spectra match as closely as possible. This matching can be done manually as well as with the aid of a subroutine within RUMP which searches for an acceptable fit to the experimental data. The match on the energy axis is determined primarily by the film thickness, and the magnitude of the normalised yield by the ratios between the chemical elements. It is possible and necessary to enter the density of YBCO and MgO in terms of atoms/cm^3. If this is not done, RUMP estimates the atomic density and obtains erroneous results.

Because the read-out electronics cannot measure particle energies less than 300 keV [15], it is not possible to determine the oxygen content in the film because of its low scattering energy. It is also difficult to distinguish between the oxygen in the film and the substrate. However, sufficient oxygenation of the film is usually reflected in the resistivity and permeability measurements.

In Figure 4.6, the correspondence between simulation and measurement is extremely good except for a small region at the top of the peak. Poor correlation could possibly be caused by film-substrate interdiffusion. Mixing of the film with the substrate can occur at the high temperatures used during deposition [67]. It is also possibly due to some inhomogeneity in the ratios of Ba, Y or Cu in the film.

Atomic force microscopy (AFM)

Atomic force microscopy (AFM) [68] is used to produce accurate topographical measurements of a film's surface. The operation of an atomic force microscope is illustrated in Figure 4.7. When operating in contact mode, the tip is raster-scanned across the sample surface, coming into direct physical contact. A laser beam is reflected off the rear of the cantilever into a multi-section photodetector. The differing heights of features on the sample deflect the cantilever and so the path of the laser beam. The output of the photodetector is fed back in a control loop to maintain a constant cantilever deflection by means of a piezoelectric actuator. The signal used to maintain the constant force is read out to give height data with nanometre resolution. The data can be manipulated on a computer to produce three-dimensional plots with special effects like simulated lighting and vertical-scale exaggeration.

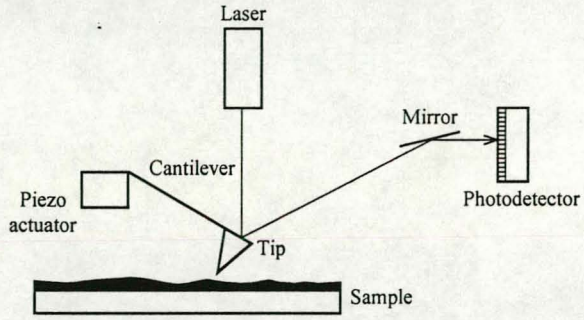

Figure 4.7 Operation of atomic force microscope operated in contact mode.

This imaging method is relatively non-destructive since the force on the probe tip is of the order of nanonewtons. The maximum scan area is 130 μm × 130 μm and the height variation of the surface features must be less than 9.7 μm.

The surface roughness and the size of large particles is a good indication of the film quality. Good quality films have small surface features and their total surface area is very close the scan area. Large particles make etching of the film into any particular shape more difficult. In addition to obtaining information about the film surface, it is also possible to measure the film thickness with AFM. The YBCO is removed from part of the substrate by etching and the change in height across the resulting step is measured. A shortcoming of this method is that erroneous thickness measurements will be obtained if the etch used to remove the YBCO also removes some of the substrate material. AFM is used in Chapter 5 to image important sections of a Josephson junction test circuit.

4.2.4 Optimisation of the PLD parameters for obtaining good quality YBCO films

There are four deposition parameters which strongly affect the properties of the YBCO film, namely partial oxygen pressure, laser energy density on the target surface, target-substrate separation distance and substrate temperature. The optimisation of these parameters with respect to critical current density, critical temperature and surface smoothness is by far the most difficult and time-consuming part of the process of producing superconducting thin films. Together with the design of the entire pulsed laser deposition system, this optimisation was first carried out by Maritz [14] for his PhD thesis. Conradie [15] also performed similar optimisations. For a given PLD system, a number of parameter sets will give good results [69].

Maritz was only able to perform a single deposition for this project before his contract with NAC was terminated and he was forced to find work elsewhere. This meant that it was necessary to learn and become experienced in the entire process personally. Because of this, a great deal of experience and knowledge of the finer points of the process were lost and had to be gained from scratch. Unfortunately, a two month time limit, a shared PLD system and a limited number of available substrates prevented a comprehensive optimisation from being carried out. Depositions were performed on a total of twelve single-crystal substrates, the last two of which were used to confirm that the final set of parameters would yield consistent results. Single-crystal substrates were used for the characterisation because they are identical to bicrystals as far as the growth of superconducting films is concerned and they are infinitely cheaper. It was not initially appreciated that although the operation of a PLD system is conceptually simple, it is actually an extremely complex physical process and there are many non-idealities that can influence results. The deposition of YBCO films by PLD is not simply a matter of blasting particles off a target and onto a substrate. The ejected material forming the plume is a plasma consisting of molecules, atoms, ions and electrons [15, 70]. The deposition conditions must be precisely correct for these particles to recombine on the substrate surface with the correct chemistry and crystal structure.

During deposition, the film grows during each laser pulse, reproducing the crystal structure of the substrate. The deposition rate for YBCO is of the order of 0.1 nm per pulse but is influenced by the target-substrate distance and the size and shape of the plume. Immediately after deposition, the film is semiconducting and must be annealed in 900 mbar oxygen at 490 °C for about 30 minutes [14, 71]. This changes its crystal structure from the tetragonal ($a = b \neq c$, $\alpha = \beta = \gamma = 90°$) to the oxygenated orthorhombic phase ($a \neq b \neq c$, $\alpha = \beta = \gamma = 90°$) which exhibits superconductivity [72]. The anneal is performed slightly below atmospheric pressure so that the chamber remains sealed. During the deposition itself, it is necessary to introduce as much oxygen as possible. This reduces the amount of structural change that takes place during annealing which could give rise to structural defects such as twinning and dislocation [72]. Of the four primary deposition parameters, two were held constant at values suggested by [14, 71]. The oxygen pressure was kept at 0.3 mbar and the substrate temperature at 795 °C. The high temperature is necessary to provide sufficient surface activation for the formation of good tetragonal structures [72]. In

the attempt to find an optimal parameter set, the target-substrate distance and the energy density were adjusted.

The shape and length of the plume are determined by the laser energy density, spot size and oxygen pressure. Since the oxygen pressure was kept fixed, the plume shape was only dependent on the properties of the spot on the target. According to [70], the distance between target and substrate should be approximately equal to the plume length.

The target-substrate distance was varied between 30 mm and 34.5 mm. The longer distance, which was approximately the maximum allowed by the system, yielded the best results as far as resistivity and permeability measurements were concerned. The film deposited at the shorter distance could be seen to be rough and irregular, even with the naked eye. However the ratios of its constituent chemical elements, as deduced from RBS measurements, were closer to the correct values. If the target-substrate distance is too small, energetic atoms and ions can cause sputtering damage to the substrate [69].

The shape and energy density of the spot on the target proved to be the most problematic part of the depositions. Originally it was thought that the pulse energy could merely be measured and only the deposition time adjusted to compensate for the change in deposition rate. The excimer laser's output pulse energy gradually drops as the gas mixture ages and the laser must be filled every now and again. When it became apparent that this energy variation had a more serious effect, the pulse energy was held constant at 114 mJ by varying the laser voltage. It was later necessary to raise this value to 150 mJ to allow depositions when the laser had just been refilled.

In order to calculate the energy density of the spot, it is necessary to know what proportion of the laser energy actually reaches the target. The total optics loss, including that of the mirror, lens and window, varies between 30% and 50 %, depending on the cleanliness of the quartz window at the time. When it exits the laser, the shape of the beam cross-section is roughly rectangular. It is focused by the lens to a spot of about 2–4 mm by 0.5–1 mm on the target. The dimensions of this spot were determined by gluing a piece of photographic paper to a dummy target and triggering the laser manually. Ideally this should yield a nice uniform rectangular spot. The energy density is greatest near the centre of the spot and gradually diminishes towards the edge. This non-uniformity means that photographic papers with differing threshold energies register differing spot sizes. For the same reason, the apparent spot size also changes with the laser energy. This is a bit of a problem since the energy density is usually calculated as the laser pulse energy minus the optical losses, divided by the area of the spot. This ambiguity in the determination of laser energy density makes it difficult to compare the results of different workers.

Since the apparent spot size was seen to vary so dramatically, the laser was allowed to discharge partially before being triggered. This reduced the pulse energy drastically, recording only the most intense part of the spot on the photographic paper. This reduced area was then used to estimate the energy density on the target. It was assumed that the low energy did not change the actual normalised energy distribution

in the spot, although this might not strictly be true. It is also not known whether the energy density distribution changes as the laser gas mixture ages.

The energy density at the target strongly affects both the morphology and composition of the deposited film [73] since it determines the composition of the plume as well as where the particles are located within the plume. For each target material, there is a lower limit on the permissible energy density, called the energy threshold, below which the chemical composition of the target material is not reproduced. This is about 1 J/cm^2 for YBCO [73].

It was attempted to keep the energy density on the target constant at 2.6 J/cm^2 since this had been found as an optimum for this specific PLD system [15]. However, this is definitely easier said than done.

It is also possible to change the energy density on the target by varying the position of focusing lens. This does not have the same effect as changing the laser energy since a larger spot size results in a narrower, more directed plume. This, in turn, makes alignment of the plume and substrate more difficult with the result that the thickness of the deposited film may be non-uniform. The normalised energy density distribution on the target may also differ. When the laser energy was maintained at 150 mJ and the reduced area used to calculate the energy density, the density was far above the desired 2.6 J/cm^2. To remedy this, it was necessary to unfocus the spot further by moving the lens outwards from the original 4.7 mm position to the 11 mm position. This somewhat improved the electrical characteristics of the film but the narrower plume gave alignment problems.

Initially, it had been attempted to optimise the film parameters by depositing films of the order of 200 nm. However, the measurements of these films were so disastrous that it was often not even possible to see a transition temperature. Thereafter the deposition time was held at 12 minutes to make sure that enough YBCO for an acceptable measurement was deposited on the substrate.

The film with the most promising resistivity and permeability was measured, with the help of RBS, to be 1100 nm thick. The deposition time was then reduced to 2.5 minutes to obtain a film of 230 nm which is close to the desired thickness of 200 nm. All other deposition parameters were kept constant. The deposition parameters are given in Table 4.1.

Table 4.1 Deposition parameters for the 230 nm YBCO film.

Parameter	Value	Units
Laser pulse rate	10	Hz
Outside pulse energy (excluding optics loss)	150	mJ
Lens position	11	mm
Base pressure	3×10^{-6}	mbar
Oxygen pressure	0.3	mbar
Deposition temp	795	°C
Deposition time	2.5	min
Anneal time	30	min
Anneal temperature	490	°C
Anneal oxygen pressure	900	mbar

The resistivity and permeability measurements of both the 1100 nm and the 230 nm films are reproduced in Figure 4.8. It can be seen that both measurements are quite good for the thicker film ((a) and (b)), having transition temperatures unambiguously above 80 K and sharp transition widths. The measurements of the thinner film ((c) and (d)) are not as good. The resistivity graph exhibits a lower critical temperature and a larger transition width. The shape of the permeability graph is very dependent on the magnitude of the applied field. Curves (ii) and (iii) were generated by reducing the driving-coil current by a factor of 10 and 100 respectively. The curve (iv) was produced at 10 kHz instead of the usual 100 kHz and the coil current was about one tenth of the usual value. These measurements suggest that although superconductivity is exhibited at 77 K, the film is of poor quality and cannot support large currents. It is also likely to be inhomogeneous. At some point during these experiments, the oscilloscope used to measure the signal from the energy detector went out of calibration, giving a reading of about 10% too low. It is not known whether this contributed to the deterioration of the film's properties.

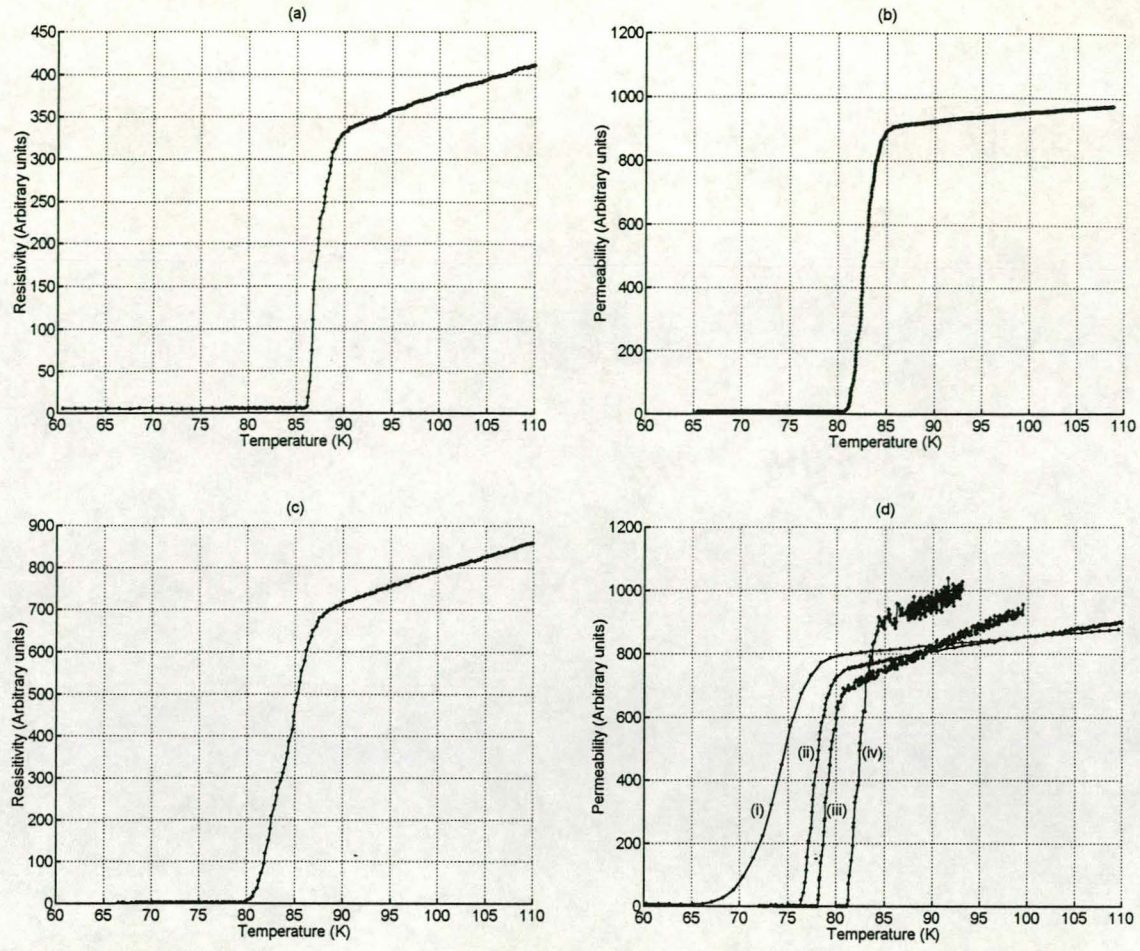

Figure 4.8 Resistivity and permeability graphs of two thin films. In (a) and (b), the film is about 1100 nm thick. In (c) and (d) the deposition time was reduced substantially to obtain a thinner film estimated at 230 nm. The thinner film's measurements are considerably worse, with the permeability curve very dependent on the strength of the applied magnetic field.

4.2.5 Possible reasons for poor results and recommendations to obtain better quality thin films by PLD

The laser used for these depositions was not the same laser as that used previously by Maritz and Conradie [14, 15] for the optimisation of the laser energy density. The previous laser provided lower pulse energies. The energy density distribution in its beam is not known. The profile of the beam used for these experiments was not Gaussian. It had bright bands along the two longer edges of the beam cross-section, probably caused by a slight misalignment of the internal mirrors.

It is perhaps an idea to use a circular diaphragm to limit the beam size. This would make the energy density on the target much more uniform and allow one to make a more accurate estimate of the energy density. Dam et al. [73] was able to obtain stoichiometric (i.e. having the correct chemical composition and ratios between elements) YBCO films by using projection optics to deliver a spatially uniform energy density, just above the threshold value, to the target. An approximately round spot would produce a symmetrical plume. A smaller spot size would result in a wider

plume, making alignment less critical. There would therefore be less thickness and quality variation within a single film.

On several films, a mat finish was noticed on the part of the substrate in line with the centre of the plume. It is thought that this was caused by the deposition of large particles as a result of insufficient pre-ablation of the target. The effect was probably exaggerated because of the narrow plume. The presence of the large particles makes it difficult to etch small features accurately.

The use of the more expensive $SrTiO_3$ substrates would enlarge the range of parameters over which good quality films can be deposited because of the substrate's good lattice match with YBCO [69]. This would increase the likelihood of success and potentially improve the electrical characteristics of the film.

Lastly, if more than one person is using the PLD system, small changes made by other users can cause undesirable and unreproducible results, especially if completely different experiments are being performed. The changes that can be made to the deposition set-up are also more limited.

4.3 Patterning of the film

The photolithography and etching can be summarised as follows. It will be described in more detail later. The circuit is drawn in AutoCAD [74] and cut into a sheet of Rubylith [75]. This is photographed onto a glass plate which acts as a mask. The YBCO film is covered with a photoresist, illuminated with ultraviolet light through the mask, and the exposed parts of the resist removed with a developer. The unprotected parts of the YBCO film are etched away with a dilute acid and the remaining resist removed with a solvent.

4.3.1 Making a contact mask

Preparing the artwork – creating a 20:1 negative film image

The outline of the design to be etched is drawn using AutoCAD. It is plotted on a Rubylith sheet using a 90° sharpened metal point in place of the plotter pen. The red layer is peeled off inside or outside the outline of the device to create a negative or positive image respectively. Red is equivalent to black here since the photographic emulsions used are not sensitive to the red part of the spectrum. The largest part of the design is plotted at a scale of 40:1 and peeled to create a positive image. The smallest sections of the device are plotted at a scale of 200:1 as a negative. They are then shrunk to 20% with a reduction camera onto black and white film to make a positive image. This is done to reduce the inaccuracies of the plotting process. The small sections are cut out, aligned correctly by means of alignment marks and then stuck down with adhesive tape onto the 40:1 Rubylith. The resulting artwork is reduced by 50% to form a 20:1 negative image.

Removal of an environmentally dangerous substance in the Rubylith by the manufacturers has recently caused Rubylith to become brittle and more difficult to cut and peel. For this reason it was necessary to find old stock to use the above-mentioned method successfully.

Producing the contact mask – making a 1:1 positive image on a glass plate

The negative 20:1 artwork is taped to the front of a light-box which illuminates it from behind with white light. A camera body, which has been designed to accept glass photographic plates, is set up at about 4.5 m from the artwork with a 210 mm Mamiya-Sekor medium-format lens attached. The focusing is done on a ground-glass screen which temporarily takes the place of the photographic plate.

A Millimask [76] 2" × 2" × 0.06" glass plate negative is placed in the camera with the emulsion side facing the artwork and exposed by switching on the light-box for the desired time. The negative is removed from the camera for developing under red light.

The plate is rinsed in deionised water for 2 minutes and then developed using Kodak D8 developer diluted 1:3 (with deionised water) at 20 °C. This developer is home-made and the recipe is given in Appendix C. After the plate has developed sufficiently, it is cleaned off in deionised water for 1 minute and fixed using Acufix fixer diluted 1:3 for 2.5 minutes. The developed negative is now rinsed with running tap water and then with deionised water for 5–10 minutes. The mask created in this way is black where the YBCO layer should be and transparent where it is to be etched away.

Initially, the plates were exposed at f/11 for 3–3.5 minutes as this was given as optimum by previous users of the equipment. A mask of a SQUID, with hole and slit dimensions of 14 μm and 3 μm respectively, appeared acceptable when viewed under the microscope of the mask-aligner. It was only when the structure could not be reproduced by the next step of the process that the mask was examined more carefully under a better microscope using transmitted instead of reflected light. Both the SQUID hole and slit appeared greyish instead of clear, and the lines out of focus and granular.

To try and remedy this, the exposure times were first decreased and then increased around 3 minutes with the f-stop kept the same. Of these, the 3 minute exposure was the best. To try and improve the depth of focus and therefore also the sharpness of the image projected onto the photographic plate, the camera aperture was systematically stopped down to f/32 with the exposure time doubled for every f-stop. The plates began to look increasingly underexposed as the aperture size was decreased and the emulsion brown instead of the desired grey or black. This could not be remedied by an increase in development time or developer concentration. The optimal exposure energy of the emulsion is probably a decreasing function of light intensity and only constant at high light intensities. To compensate for this, the emulsion was exposed for longer times, on occasion up to an hour. This corrected the exposure but the smallest features looked even more out of focus and very granular.

In desperation, precisely the opposite approach was followed, one that theoretically should give the worst possible results. The plate was exposed for 25 seconds at f/4, the largest possible aperture. This gave a surprising result. The mask image was the sharpest yet obtained at that stage but looked as though a light had been shining on the image from one side, casting a shadow. The aperture was then decreased, with a number of exposure times tested for each f-stop. A 1 minute exposure at f/8 gave the sharpest image without a significant shadow. It was later discovered that this behaviour is to be expected since most commercial lenses are optimised at f/8. A larger aperture gives less depth of focus and a smaller one introduces diffraction effects.

Although this mask was an improvement on the previous attempts, it was not good enough. A number of possible sources of error were considered, namely poor focus, chromatic aberration, halation, irradiation and poor developer contrast.

Because the camera does not have a view-finder, the image must be focused on a photographic plate which has been ground on the one side. The available ground plate was too course for the size of the images and it was necessary to grind another one using a finer abrasive powder. In addition, a 60× microscope was mounted behind the camera so that the smallest features of the image projected onto the ground glass could be seen. During focusing, the lens moves through the in-focus position extremely quickly (an angle of about 2°), making it difficult to focus accurately.

No refracting lens is strictly achromatic. This means that the spectral components of white light are brought to focus at different points, causing enlargement of point or line images. The peak response of the photographic emulsion is to light of 525 nm wavelength and the manufacturers recommend that a filter with a transmission peak at this frequency be used. Such a filter could not be obtained locally so a blue plastic sheet was placed inside the light-box. Although this does not have the correct filter response (since 525 nm light is green), it provides some form of band-limiting. Despite this, no improvement could be seen on the developed image but it was easier to focus the lens since the chromatic aberrations of the microscope were not as pronounced. Unfortunately, the blue plastic also reduced the light intensity of the light-box which meant that the correct exposure time had to found once again by trial and error.

When light from the lens passes through the emulsion, some of it reflects off the back of the photographic plate. It then hits the emulsion for a second time, causing a ring-shaped halo about point sources. This effect, known as halation, was once a problem in astrophotography. The back of the plate was painted mat black to reduce the reflection but there was no noticeable improvement.

Irradiation is the scattering of light within the emulsion [77]. Emulsion grains adjacent to those directly illuminated are also exposed, causing a spread of the recorded image. If the emulsion grains were independent of one another, there would be enough of them per unit area to reproduce the image faithfully. There is no way of removing this effect except by buying photographic plates with a thinner emulsion layer or no grain. In this set-up, it is the most important factor limiting the resolution

of the image. It is, however, possible to reduce its effect to some extent by underexposing the emulsion.

A commercial high-contrast developer was tested to see whether it would yield improved results, but its action was found to be inferior to that of the home-made Kodak D8. To reduce the effect of irradiation, the underexposed emulsion was developed until it became a darkish grey colour. Normally a high-contrast developer turns all of the exposed emulsion dark black. Stopping the development at this point limits the development of areas which have been exposed by scattered light. Using undiluted developer and omitting the predevelopment soak in deionised water yielded improved results, the idea being to develop only the surface layer of the emulsion.

In all the preceding experimentation, the emulsion was developed until the exposed areas looked dark enough. Since all development is done under red light, deciding this is rather difficult. The development time can not be used as a guide because it is very dependent on the manner of agitation in the developer. The amount of development is as important as the exposure time, so a slight overdevelopment can make the plate look as though it has been overexposed.

One factor which has not been mentioned is the age of the plates. When the agents were contacted, they said that their last remaining stock had been dumped eleven years ago when it was beyond its expiry date. The plates used here had been kept sealed in a fridge. Although they do not appear to be fogged at all, it is not known what other effects ageing might have.

A summary of the possible problems and the steps taken to remove their effects is given in Table 4.2.

Table 4.2 Possible limiting factors of the mask-making process.

Possible Error	Action taken to remove effect of error	Level of importance
Poor focus	Ground finer ground-glass focusing screen. Focused on ground glass through microscope. Stopped camera aperture down to f/8 after focusing.	High. Although large structures may appear in focus, smaller ones are not necessarily so. Can be removed.
Chromatic aberration	Band-limited light source with filter.	High, but has minimal effect with good achromatic lens. Colour shifts of microscope can prevent accurate focusing.
Irradiation	No cure for given emulsion. Emulsion underexposed and underdeveloped to limit secondary effects. Tried to develop surface layer only by using concentrated developer (1:1) and omitting presoak.	Very high. Probably the most important limiting factor. Thinner emulsion or finer/no grain would improve resolution.
Halation	Painted back of plate with mat black spray paint.	Medium. Could be a problem if irradiation could be prevented.
Poor contrast due to developer	Tried alternative high-contrast developer but original developer worked better.	High contrast important to limit effects of irradiation.

4.3.2 Professional manufacture of a chrome mask

A 2.5" chrome mask was manufactured professionally [78] to try and improve the reliability and quality of the fabrication process. This was not done initially because of the expense involved and the (mistaken) belief that it was possible to obtain sufficient resolution using the existing facilities. The features were much clearer and sharper than those of the home-made masks. Chrome masks are also more resistant to damage than those of emulsion. The parameters for the photolithography needed to be optimised for the new mask. The removal of the edge bead is still done using the emulsion mask.

A phenomenon was observed with the new mask which had not been noticed previously. At every convex 90° corner, the developed resist had a symmetrical pattern consisting of a main lobe on either side of the corner followed by several smaller lobes. It is thought that this is an interference pattern similar to that of a double slit, where the resist has been eaten away at the points of constructive interference. It is likely that the interference takes places in the resist layer, perhaps aided by secondary reflections off the shiny chrome of the mask. It was attempted to

reduce the resist thickness and so the distance over which interference could occur by spinning the resist on at 10 000 rpm. This did not yield any visible improvement. This is perhaps not surprising since the manufacturer's graph of resist thickness versus spin speed appears to level off at higher spin speeds. It would probably be advisable to use a less viscous resist to reduce the layer thickness.

4.3.3 Photolithography and etching

Initially a very old (more than 10 years) positive photoresist, Shipley TF20 was used but it was especially viscous, long UV exposure times were necessary and fine detail could not be produced. A more recent resist, Hoechst AZ1140 was obtained from Plessey SA [79] which was a big improvement. However, new supplies of Shipley S1818 positive resist, MF319 developer and 1165 remover were purchased soon afterwards and used for all further experimentation.

Spinning on the resist

The substrate with its layer of YBCO is placed on an O-ring in the centre of a resist spinner. Resist is dropped onto it with a syringe making sure that the entire surface is covered. It is spun at 5 000 rpm for about 90 seconds to give a layer of about 1.6 μm, according to manufacturer's data sheets. The centrifugal force moves excess resist to the substrate edge and the resist viscosity determines the degree of this movement. Hereafter, the substrate is allowed to stand for about 10 minutes for the resist to dry. A very basic guide to the use of the most important laboratory equipment is given in Appendix D.

Soft bake

The coated substrate is now baked on a controlled hot plate at 100 °C for 30 minutes. The baking removes excess solvents. Underbaking increases developer attack on unexposed resist. Overbaking reduces the resist's photosensitivity and can actually destroy part of the resist [80]. Originally the substrates were baked in a circulated oven but the oven was found to exhibit large temperature variations, requiring a long settling time. Opening the oven to put in the substrate would upset the equilibrium. A thick aluminium plate was placed in the oven to act as a thermal load onto which the substrates could be placed. This method was later abandoned in favour of the hot plate which reached its operating temperature in under 30 minutes and exhibited minimum temperature fluctuations (±1 °C). The baking time could also be reduced if necessary because of the substrate's direct contact with the plate [81].

Illuminating the photoresist

The glass contact mask, produced in Section 4.3.1, is placed above the sensitised substrate in a mask-aligner, with the emulsion side facing downwards. The substrate is moved with micrometer screws until it is correctly aligned with the mask and then

pressed into contact with the bottom of the mask. The alignment is performed under the aligner's high-power microscope. The mask is exposed to the aligner's ultraviolet light source. The exposure time is dependent on the thickness of the resist, the reflectivity of the surface to be etched and the quality of the mask. The grey and not black colour of the mask, caused by its deliberate underexposure, does not completely block the UV light. This limits the resist's exposure time.

Developing

The substrate is immersed in MF319 developer which dissolves the sections of resist exposed to the ultraviolet light. The development is then stopped by immersion in deionised water and the substrate dried with compressed nitrogen. The soft bake and exposure time were adjusted to give a development time of the order of 30 seconds. This time is critical for accurate line control. Too short a development time prevents the complete removal of exposed resist. Overdevelopment causes small features to be eaten away.

Hard bake

The substrate is baked on the hot plate at 110 °C for 30 minutes. In addition to hardening the resist, making it more resistant to attack by the etchant, it allows it to flow slightly, filling in pinholes and thinner areas.

Etching and removing resist

The substrate is submerged in an etching solution and placed in an ultrasonic bath to aid the etching process. The etching action is stopped by rinsing in deionised water when the film has been completely removed from the exposed areas. The remaining resist is dissolved with Shipley 1165 remover, after which the substrate is rinsed in ethanol and blow-dried with compressed nitrogen.

Optimisation with test pattern

In order to optimise the entire process including the mask-making, the test pattern shown in Figure 4.9 was designed. It contains shapes which are typically found in a SQUID design, such as square washers, pairs of parallel lines, and single lines. The numbers in the diagram refer to the line-widths which range from 30 μm down to 1 μm. Unfortunately, the quality of the Rubylith at the time of manufacture set the limit on the sizes of the various structures at 5 μm for the square washers, 2 μm for the parallel lines and 1 μm for the single lines. The reduction on film was good except for a slight rounding of sharp edges. Many trial runs were done on uncoated MgO single-crystal substrates. The last few tests were done on coated substrates to correct the ultraviolet exposure time for the less reflective surface, and to see the effects of different etching times.

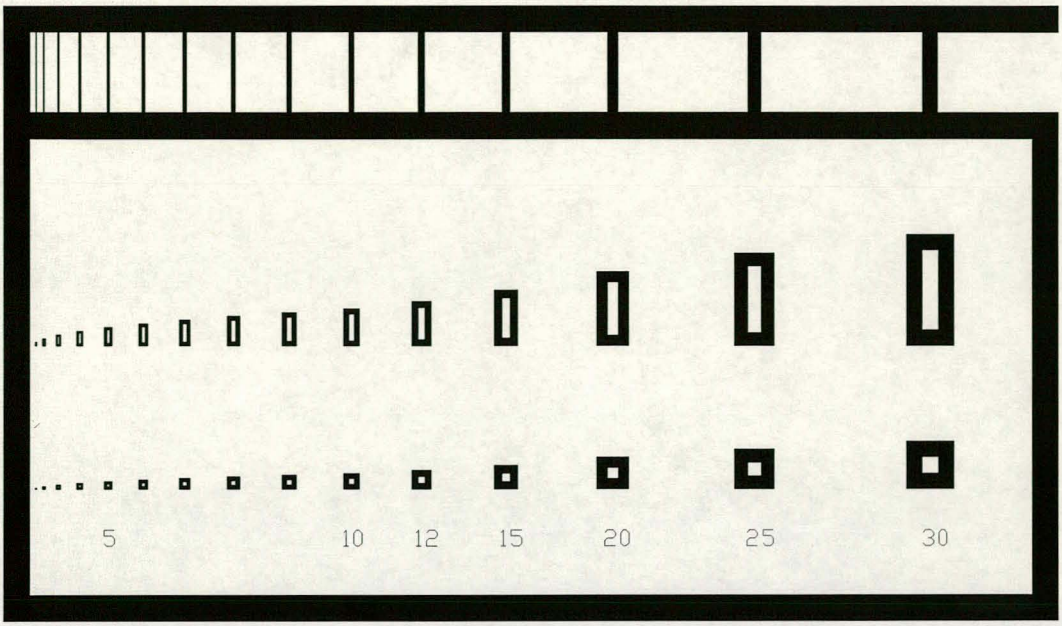

Figure 4.9 Test pattern for optimising fabrication process.

4.4 Process used to make Josephson junctions or SQUIDs

This section gives a description of how the photolithographic process is applied to the manufacture of Josephson junctions or SQUIDs. Figure 4.10 shows the various steps involved in the manufacturing process.

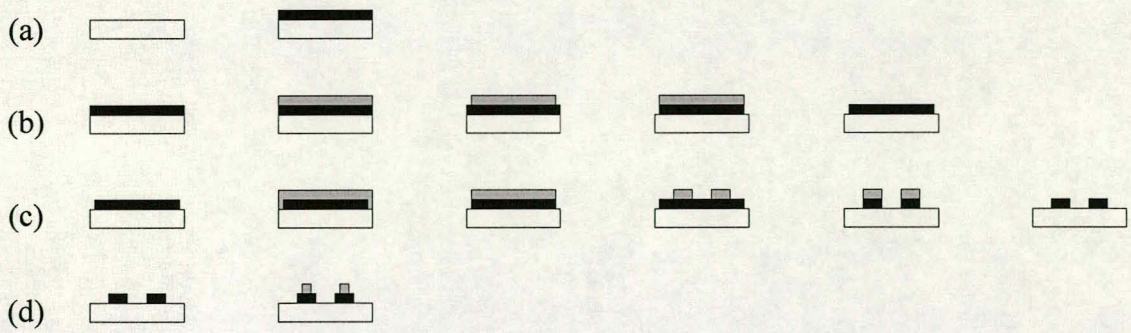

Figure 4.10 The various steps in the manufacturing process. (a) YBCO deposition. (b) Exposure of bicrystal line. (c) Etching of YBCO film. (d) Deposition of contact pads.

4.4.1 Deposition of the YBCO film (a)

An YBCO film is deposited on an MgO bicrystal substrate by pulsed laser deposition as was described in Section 4.2.

4.4.2 Highlighting the bicrystal line (b)

The film is coated with resist, soft-baked and exposed through a mask to remove a 0.4 mm strip of resist along the edges of the substrate. It must be exposed for longer than usual (about 3 minutes) to compensate for the edge bead that forms because of the resist's surface tension. Marks that just touch the substrate edge when correctly aligned are used to position the substrate prior to exposure. After development, the resist is hard-baked and the exposed part of the YBCO removed with a citric acid solution. The MgO substrate is then etched with a 1% HF solution in an ultrasonic bath for 5 minutes to make the bicrystal grain boundary visible. All the remaining resist is then removed.

4.4.3 Etching the Josephson junction device (c)

The resist edge bead is removed in the same way as mentioned above. The remaining resist is now exposed for a short time through the mask made of the device layout. The mask and substrate are carefully aligned by using the (now) visible parts of the bicrystal line and another set of marks on the mask. The alignment has to be extremely accurate as the SQUID legs, which the grain boundary must cross, are only 15 μm long. After development, the substrate is hard-baked and the exposed YBCO etched away with citric acid. The resist covering the remaining YBCO sections is then removed. The precise details of the photolithographic process are given in Appendix E.

4.4.4 Deposition of the contact pads (d)

The contact pads can also be deposited using the PLD system if the usual YBCO target is replaced by one of gold. A thin aluminium mask is fastened over the YBCO device. The mask has holes drilled at the positions where the contact pads are to be deposited. The substrate fits into a depression milled into an aluminium block and the mask is clamped down over it with screws. The whole assembly is stuck to the heater surface with Prestik. The deposition is performed at room temperature and at as low a pressure as possible (about 10^{-5} mbar). The deposition time should be much greater than for YBCO since thick contact pads are desirable for wire-bonding and gold's high atomic mass makes for a lower deposition rate.

4.4.5 Connection to measurement devices

The substrate is stuck to a PCB with epoxy glue and further secured with beryllium copper clips. When suitably annealed, beryllium copper retains its elasticity at low temperatures. Tightening the clips excessively can crack the substrate so they should be omitted if the surfaces are suitable for gluing with epoxy. Contact pads corresponding to those on the YBCO are etched on the PCB. Small gold pads are placed on top of these with a ribbon-bonder since gold wire-bonding can not be done on copper or solder. The pads on the chip are connected to those on the PCB by wire-bonding. Thicker copper wires are soldered to the PCB which lead to external

electronics. Provision is made for a coil under the substrate to investigate the effect of the magnetic field on the Josephson junctions or SQUID. The PCB fits inside a permeable metal shield [82] which screens dc magnetic fields. The completed device is stored in a desiccator to prevent water vapour from degrading the YBCO. One step which has been omitted here is the deposition of some kind of passivating layer over the device. This must be done to prevent degradation of the YBCO if the device is to be used for any length of time.

4.5 Conclusion

The process described in this chapter requires several months of optimisation. Once the process is optimised, the fabrication of the complete device takes a few days. It is difficult to fabricate small structures using home-made contact masks. However, such masks are quite sufficient for fabricating devices that do not require quite the resolution of a Josephson junction, such as microwave filters. Features larger than about 20 μm can be fabricated with relative ease. Because the greatest resolution limitation lies in the mask-making, having this done professionally dramatically improves the quality of the devices fabricated and eliminates the need for spending large amounts of time achieving an acceptable mask quality.

Chapter 5

Measurement of Josephson junctions

5.1 Introduction

In Chapter 3, the design of a SQUID gradiometer was carried out with typical parameter values taken from the literature. Unfortunately, there is a large variation in these values, especially those of the Josephson junctions, such as j_c and ρ_N. For this reason, it would be advantageous to fabricate a test circuit which contains Josephson junctions of varying widths. One would then be able to judge the accuracy of the predictions and observe the variation in parameters within a single substrate. The measured parameters would enable one to finalise the design of the SQUID gradiometer for one's own fabrication process. In addition, a successful measurement of Josephson behaviour would confirm that Josephson junctions can indeed be fabricated using the method described in Chapter 4, and that the measurement system is successful.

5.2 Construction of a Josephson junction test circuit

5.2.1 Layout

The layout of the circuit that was designed to characterise the junctions is given in Figure 5.1. The relevant detail is shown magnified in Figure 5.2. The circuit contains two junctions of each integer width from 4–7 μm and a single 50 pH SQUID with 4 μm junctions. Each junction is connected to two sets of contact pads so that a four-point measurement can be made. The resistances of the contacts and wire-bonds will then not influence the measurement of a junction. If this method is not used, these parasitic resistances can dominate the measurement to such an extent that it is not even possible to see whether the junctions exhibit superconductivity.

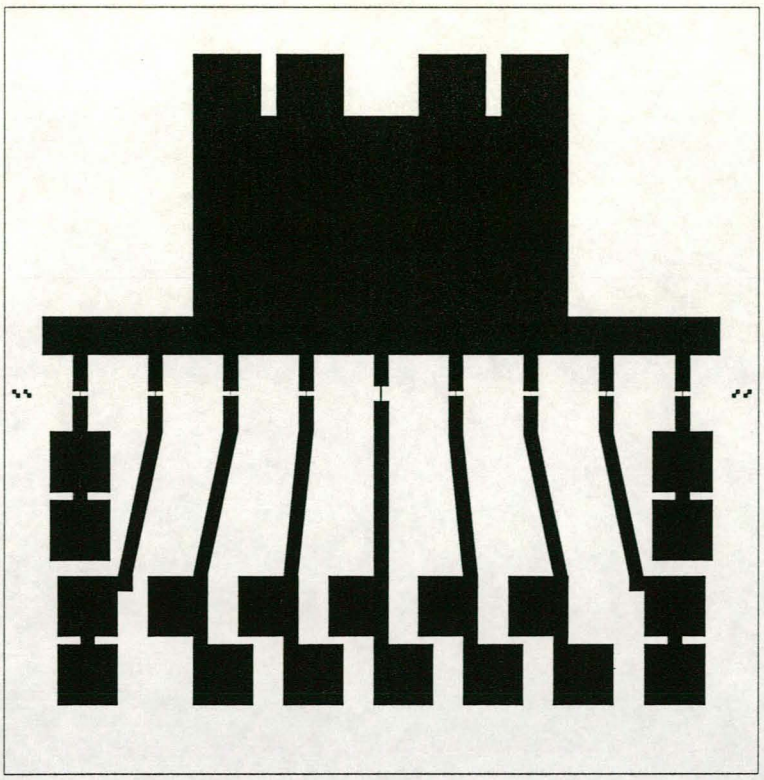

Figure 5.1 Layout of the Josephson junction test circuit for a 1 cm × 1 cm substrate (10:1 scale).

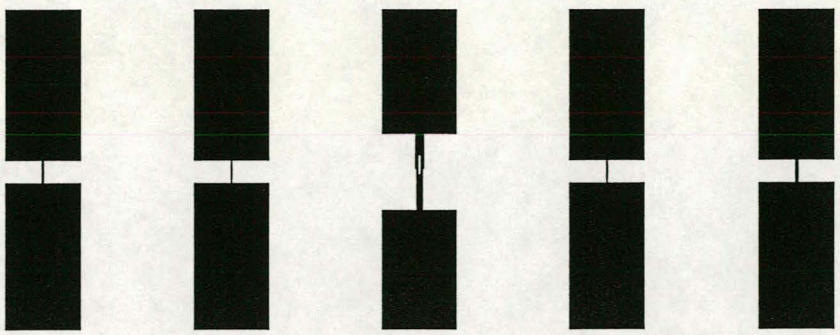

Figure 5.2 Detail of the Josephson junctions and SQUID (50:1 scale). From left to right, the junction widths are 6, 4, 4 (SQUID), 5 and 7 μm.

5.2.2 First fabrication attempt

The bicrystal substrate for this test circuit had been used by another worker in an earlier unsuccessful attempt at fabricating Josephson junctions [15]. The gold contact pads were removed with a non-acid gold etch (see Appendix C4) to prevent damage to the substrate, and the remaining YBCO film was removed with citric acid. Both etchings were done in an ultrasonic bath. The substrate was washed off in deionised water, dried with compressed nitrogen and then baked at a low temperature to remove any remaining moisture.

A 200 nm film was laser-deposited by Maritz for 10 minutes with an outside laser energy of 68 mJ. The lens position was 5 mm and all the other parameters were the same as those given in Table 4.1. The superconducting properties of this film were not measured so it is not known how it compares with the final film of Chapter 4.

The film was patterned using photolithography and wet etching. The home-made emulsion contact mask was used for the photolithography. The final etching took considerably longer than had been necessary with other films. Because of either a misunderstanding about the desired thickness or a mistake in the calculation of the deposition time, the gold for the contact pads was deposited for only 20 minutes. The aim was to deposit pads at least 1 μm thick.

The MgO substrate was then attached by means of glue and clips to a PCB which had a square, 20-turn copper coil glued to its underside. The coil could provide an estimated magnetic field of about 80 G with a 4 A current [83]. The gold pads proved to be too thin for proper wire-bonding. The bonding wires were tacked onto these pads with the wire-bonder, and then secured with silver epoxy. The other ends were wire-bonded to the gold pads on the PCB, and the whole assembly was heated slightly in an oven to cure the epoxy. This connection work was done at Tellumat [79]. The completed test circuit is shown in Figure 5.3.

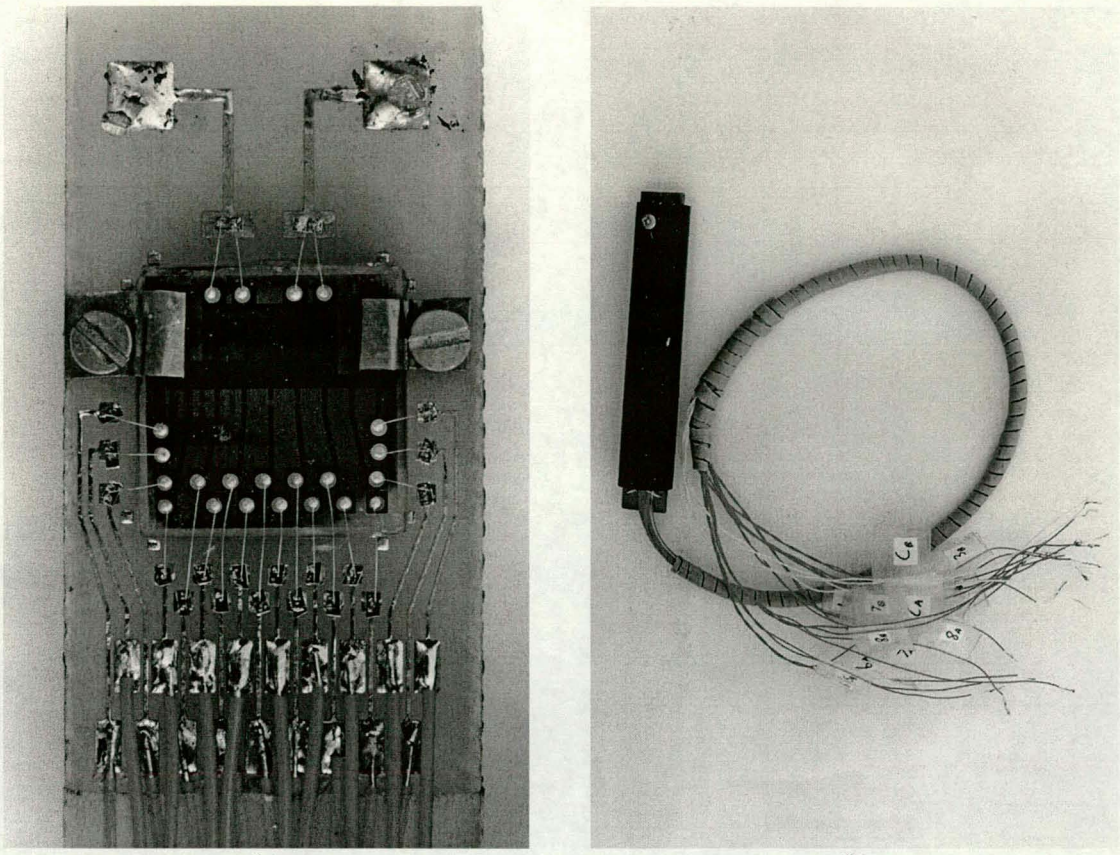

(a) (b)

Figure 5.3 The fully constructed Josephson junction test circuit. (a) At the centre of the picture is the MgO substrate with its etched YBCO layer and gold contact pads. The substrate is held tightly in place on the PCB by two beryllium copper clips. Thin gold wires (from the wire-bonding) connect the gold pads on the substrate to those on the PCB. At the bottom, thicker copper wires lead out to the measurement electronics. The magnification factor is about 3.5. (b) The PCB of (a) is shown fixed inside its magnetic shield. The magnification is 0.4.

5.2.3 Measurements of the first attempt

The device is cooled down to 77 K by suspending it in a dewar of liquid nitrogen. A bias current is injected between two of the pads and the resulting voltage measured between two others. The bias current is provided by an unearthed signal generator producing a 1 kHz triangular voltage waveform. The current through the junction is set by the resistor R_I to approximately V/R_I since the resistances of the junction and the contacts are expected to be relatively small. A non-inverting operational amplifier with gain of 100 is used to amplify the voltage between the other set of pads. This set-up is shown in Figure 5.4. The output voltage V_2 is displayed as a function of V_1 by making use of an oscilloscope's X–Y function.

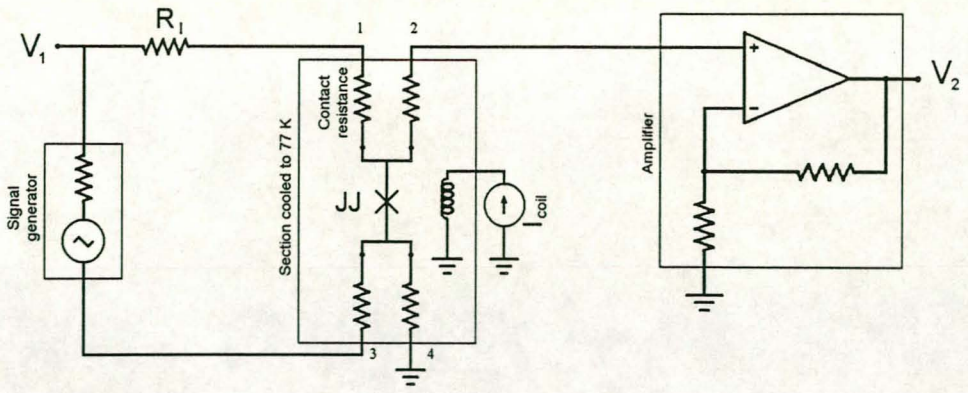

Figure 5.4 Set-up to measure Josephson junctions.

The voltage stayed approximately zero with increasing current until a point after which it started to increase in a roughly linear fashion. The bias current at this point is the critical current. The critical current was measured for each junction. The measurement was not easy to make. The amplified voltage signal was very noisy and the transition point poorly defined. It was also not possible to prevent the 50 Hz signal of the mains from coupling into the measurement circuit to some extent. The measured critical current values were in the range 1–46 mA. This was considerably larger than the expected range of 160–280 μA. In addition, the variation of the critical currents with an applied field appeared to show a linear decrease instead of the $|\sin(x)/x|$ behaviour expected from a Josephson junction. The applied field was increased to about 80 G at which point the critical current was a third of its maximum value and still decreasing. The single SQUID acted in the same manner as the junctions. Normal resistances of 6–60 mΩ were measured (using the gradient of the curve) instead of the expected 0.625–1.25 Ω. The heating effect of the large currents needed to measure the resistance was observed as hysteresis in the voltage versus current curve. This was accompanied by increased boiling of the liquid nitrogen. It was not attempted to observe the high-frequency oscillation of the junctions on a spectrum analyser since the signal was expected to be below the noise floor. To obtain such a measurement it would be necessary to redesign the test circuit for high-frequency operation with the necessary matching and low-noise amplifier.

The conclusion drawn from these observations is that the fabricated junctions were merely superconducting, having a J_c of at least 10^5 A/cm^2. They did not exhibit any Josephson behaviour. This could be attributed to a number of factors. The most basic possible error is that the bicrystal line might not have passed through the junctions. Alternatively, the junctions could have been too large or too thick at the point of intersection with the bicrystal line. Lastly, the substrate might have been damaged to some extent by the previous deposition and etching. It was thought that this would not be a problem since the damage should be slight and the crystal structure of the YBCO film should follow that of the substrate during deposition. The crystal structure of the substrate should not be changed by the damage. The first two possibilities were discounted after the junctions were examined under a light microscope.

The resistance of the contacts was measured by shorting points 1 to 2 and 3 to 4 in Figure 5.4. At bias currents below the critical current, the contact resistances

combine in series and parallel to give an equivalent resistance which has the same value as the individual resistances, namely about 0.4 Ω per pad. This includes the resistances of the gold pads, bonding wires and copper read-out wires.

To determine the actual cause of the failure, the test circuit was scanned with an atomic force microscope. Square regions, 100 μm wide, were scanned about the junctions and the edge of one contact pad. Images of the junctions are shown in Figure 5.5. The light areas represent the raised regions, namely the YBCO film, and the darker areas the exposed substrate.

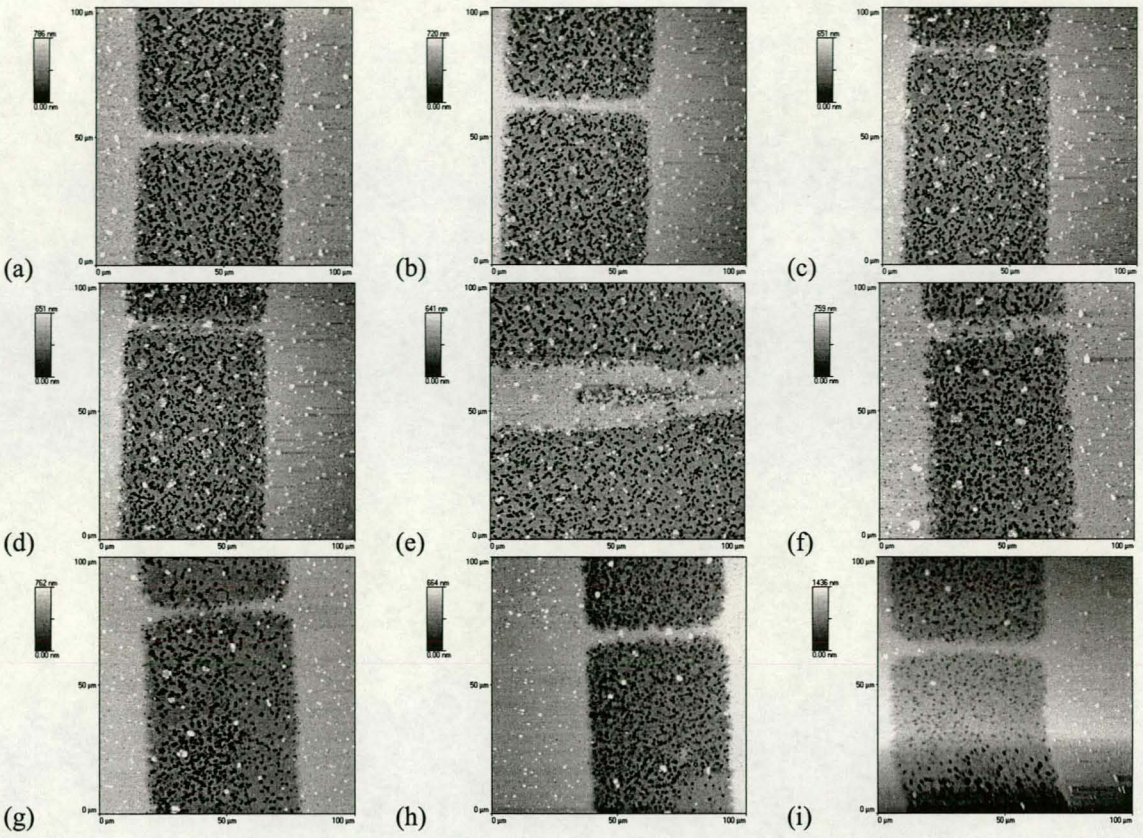

Figure 5.5 AFM images of the Josephson junctions and SQUID. The light areas represent the raised areas. The YBCO layer is therefore shown as light and the exposed substrate as darkish. The bicrystal line, which is not visible here, runs from top to bottom in all the images. The designed junction widths are, in order, 6, 6, 4, 4, 4 (SQUID), 5, 5, 7 and 7 μm.

It can immediately be seen that the line control of the structures is extremely poor and that the substrate is also severely pitted. The YBCO film is about 200 nm thick, as desired, but the gold contact pads are only 250 nm. The poor line control can largely be attributed to the pitting of the substrate which extends down to about 400 nm below its surface. The increased etching necessary to remove the YBCO from the hollows has caused underetching in random places. The quality of the mask also has an effect on the device quality. It causes rounding of sharp edges such as the widening of the junctions where they join the connecting wires. However, on a previous etching of a single-crystal substrate, its effect was not nearly as severe.

The surface of the YBCO film is surprisingly smooth although there are small dips where the pits have been filled in and a number of largish particles, about 200 nm

high, scattered across the surface. It was also noticed that the AFM scan did not detect the bicrystal line. This is surprising since chemical action, such as that which could have damaged the substrate, normally takes place more rapidly at the site of a crystal defect such as a grain boundary. This effect was used to expose the bicrystal line on the edge of the substrate. This suggests that the damage to the substrate was as a result of the first deposition process.

In retrospect, it should have been expected that the film would experience problems. As mentioned in Chapter 3, the entire film must be c-axis orientated. This would not necessarily be the case on a damaged substrate since the (100) and (010) planes of the MgO crystal are exposed in the pitted region. This could lead to the deposition of a- or b-axis orientated crystals, producing an amorphous film. This means that in addition to the possibility of having a poorly defined grain boundary, the YBCO film could also large numbers of random grain boundaries.

5.2.4 Second fabrication attempt

An YBCO film was deposited on a virgin MgO substrate using the parameters of Chapter 4. The photolithography necessary to pattern the film was performed using the professionally manufactured contact mask. Before the device was etched, a permeability measurement was performed on the film, yielding slightly better results than for the film discussed in Section 4.2.4. The gold for the contact pads was deposited for a full 3 hours to ensure that they were sufficiently thick. The wire-bonding was performed without any difficulties. At the rate of gold deposition which was deduced from the first fabrication attempt, the pads should be over 2 μm thick. The completed Josephson junction test circuit is shown in Figure 5.6(a). If it is compared with the corresponding photograph of the first fabrication attempt (Figure 5.3(a)), the outline of the device is much sharper and all of the YBCO has been removed from the relevant parts of the substrate. Probably because of overtightening of the beryllium copper clips, a crack developed on the substrate surface. Two junctions on the left were destroyed outright, the leads of the next two broken, and the common upper contact pads electrically insulated from the junctions themselves. The silver epoxy which was used to reconnect the circuit can be seen as a shiny band in the centre of the chip.

The AFM scans of Figure 5.6(b) show two different views of the SQUID shape in the test circuit fabricated on a single-crystal substrate with the chrome contact mask. The etching quality is exceptionally good. In comparison, the quality of the equivalent structure on the first fabrication attempt (see Figure 5.5(e)) is appalling.

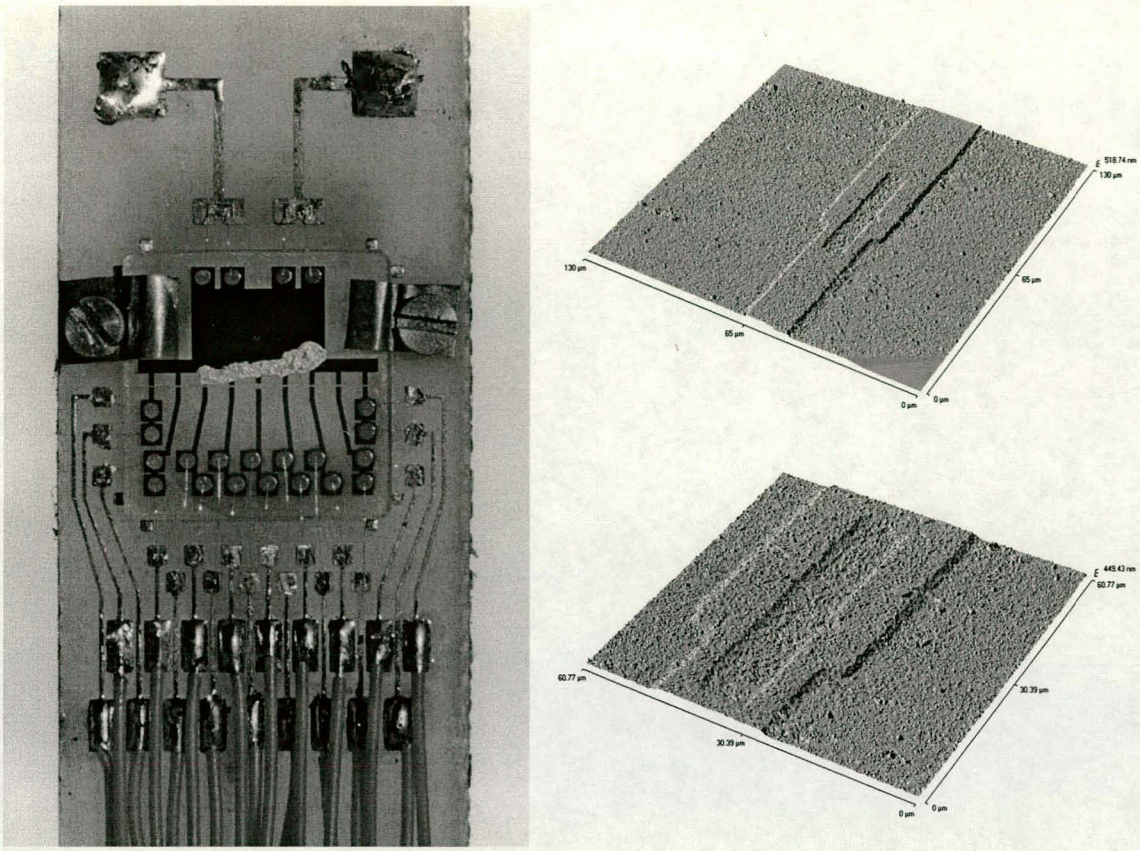

(a) (b)

Figure 5.6 (a) The fully constructed Josephson junction test circuit. At the centre of the picture is the MgO substrate with its etched YBCO layer and gold contact pads. Overtightening of the beryllium copper clips partially cracked the substrate. Silver epoxy was used to reconnect the larger YBCO sections. The magnification factor is about 3.5. (b) Two different AFM scans of the SQUID shape fabricated on a single-crystal substrate with a chrome contact mask. The etching quality is exceptionally good. The junctions (thinnest sections) are 4 µm wide.

5.2.5 Measurements of the second attempt

Particular attention was paid to the experimental set-up to avoid the noise and interference problems experienced in the measurement of the first device. To minimise interference, the fluorescent lights and all unnecessary equipment in the room were switched off. The only electronic equipment on in the room was the signal generator and oscilloscope used to make the measurement. The measurement circuit of Figure 5.4 was used once again. This time, the amplifier of the junction voltage was constructed using a low-noise operational amplifier (AD797) and it was powered by lead-acid batteries.

The junction test circuit was cooled in liquid nitrogen. Because the crack had disconnected the upper contact pads, it was necessary to measure the surviving junctions in series, two at a time. This arrangement allowed four junctions and a SQUID to be measured. Of these, one was open-circuited and the others produced similar measurements. The gradient of the voltage versus current curve was small at low currents, slowly increasing to a fixed value at higher currents. The curve was

never horizontal, even at zero current. It was not possible to measure a critical current because of the gradual change in the curve's slope. When measurements were performed the second time that the test circuit was cooled, all the junctions became open-circuited in quick succession. In order to measure the junctions individually and reconnect the two disconnected junctions, the crack was covered over with silver epoxy which was then cured in a low-temperature oven. On cooling, all the junctions were found to be open-circuited and testing had to be abandoned.

When the test circuit was viewed under a light microscope, fine cracks were noticed on most of the junctions. It is possible that the YBCO film was not completely epitaxial, i.e. the film had formed a layer on top of the substrate which did not follow the substrate's crystal structure. Cooling in liquid nitrogen and the accompanying thermal contraction could have caused small sections of the film to separate from the substrate. Small nitrogen bubbles from the bias current's heating effect on the junctions could have further stressed these sections, forming the cracks. The quality of the etching was not the best obtained with the chrome contact mask but definitely good enough to obtain working Josephson junctions if the properties of the film had permitted. The etching quality would have been better it there had been fewer large particles on the film.

5.3 Conclusion

Two attempts were made at producing Josephson junctions. Their measurements were very disappointing in that they did not provide any hint of Josephson behaviour. This can be directly attributed to the poor quality of the superconducting films. These films form the most basic element of the fabrication process. The lack of good results serves to emphasise the importance of materials science in fabrication. With the advances made in the photolithographic process, it is thought that the present fabrication method can be used successfully for the fashioning of Josephson junction devices if it is applied to good quality YBCO films.

Chapter 6

Conclusions and recommendations

The original aim of this thesis, namely the fabrication and testing of a SQUID gradiometer, has not been successful. In hindsight, this aim was perhaps overly ambitious and optimistic. It was based on the assumption that it was possible to have high quality, superconducting thin films deposited whenever necessary and that it was not needed to learn the intricacies of that process personally. Very little was known about high-T_c SQUIDs or their fabrication at the time, and it was thought that most of the effort would be expended on the design of the SQUID and on numerical simulations.

The fabrication facilities at the Department of Electrical and Electronic Engineering, although impressive in their day, are becoming rather dated. They were also designed primarily for semiconductor processing and not for the smaller substrates and the small dimensions necessary for Josephson junction devices. The laboratory had not been used for several years except for some etching of relatively large structures (>20 μm). There was no technical staff with a good working knowledge of the laboratory equipment and there was limited knowledge elsewhere. This meant that it was necessary to learn and optimise most of the processes from scratch, and maintain some of the laboratory equipment.

Despite these problems, good progress has still been made towards achieving the original goal. The entire fabrication process, except for the deposition of a good quality film, has been demonstrated to be a success. The misalignment which caused failure in Conradie's fabrication attempt is no longer as big a problem, nor is high-quality etching. A complete design of a SQUID gradiometer has been carried out. It has not been possible to come closer to fabricating such a device primarily because of problems with the deposition of superconducting films. The process described in this thesis can, in my opinion, be used to fabricate Josephson junction devices successfully if sufficient and simultaneous attention is given to the deposition of YBCO films. Once a good quality YBCO film can be deposited and it is used to fashion successful Josephson junctions, it will be relatively straightforward to fabricate a SQUID gradiometer since the same process is used.

In the introduction, it was mentioned that the gradiometer should be low cost and for that reason, the existing facilities were to be used as much as possible. However, this type of project is by nature expensive, and trying to save money can cause unnecessary delays and inferior results.

In this thesis, the simplest mathematics of Josephson junctions and dc SQUIDs are presented for completeness. A number of commonly used SQUID read-out schemes and their respective merits are discussed. The equations describing the SQUID can be used to simulate the operation of the read-out electronics. Of the various SQUID read-out schemes mentioned, additional positive feedback (APF) operated within a flux-locked loop appears to hold the most promise because of its simplicity.

A design procedure for directly coupled SQUID gradiometers has been developed which incorporates recommendations and typical values from the literature. This procedure has been used to design a gradiometer and estimate its electrical parameters. The design allows for fabrication difficulties. The effect of thermal noise on SQUID sensitivity as well as the current opinion on the mechanism and contribution of 1/f noise are discussed.

The process used to fabricate a Josephson junction device is described in some detail. The optimisations necessary to perfect the process and the problems encountered are also included. The home-made contact masks can be used to fabricate structures with a smallest feature larger than about 20 μm with relative ease. This makes them useful for the manufacture of various microwave components. Josephson junction devices, on the other hand, must be fabricated with a high-resolution mask. This dramatically improves the quality of the devices fabricated. It is certainly good enough for the successful fashioning of Josephson junctions and SQUIDs.

Two attempts were made at constructing a Josephson junction test circuit. The experimental set-up for measuring the critical currents and normal resistances of the junctions has been described. At no point did the measurements of the fabricated junctions ever detect any Josephson behaviour. At best, the junctions exhibited the properties of a standard superconductor. This can be directly attributed to the poor quality of the superconducting films.

The indirect cause of most of the problems encountered is a lack of continuity amongst researchers. As an example, the part of the fabrication process that Conradie was unable to perform successfully, namely the photolithography, etching, and the use of a good measurement set-up, was perfected in this project. However, the deposition of good quality YBCO thin films, which he was able to do, could not be repeated. As was mentioned earlier, the original intention was that either Conradie or Maritz, who had extensive experience with the pulsed laser deposition system, would be available to deposit films for this project when necessary. Because of study commitments elsewhere and extensive cost-cutting at NAC, both were unavailable this year. The only other person with experience on the PLD system, Dr Christopher Curran (employed by NAC), undertook to do depositions. He did not have experience in the deposition of YBCO films. He made several attempts but was unable to obtain good film quality. His busy schedule meant that he was unable to spend large amounts of time on this. He was, however, able to demonstrate the basic operation of the PLD system and provide a user manual. Continuity of knowledge can only be maintained if researchers are part of a project for the medium to long term. This means that doctoral students and permanent staff members should be directly involved in the research on this particular topic.

Much attention will have to be paid to the production of better quality superconducting materials before progress can be made on the electrical front. It would be ideal if a research group were to be formed which could investigate all aspects of superconducting devices. A more structured approach should be followed and there should be direct collaboration on a high level between engineers, physicists and material scientists.

A long-term project, together with the allocation of sufficient funds, will allow the purchase of more up-to-date equipment and permit regular servicing of existing equipment. Attached to the project should be a technician who can become familiar with the processes and equipment involved. He would then perhaps be able to perform many of the fabrication steps and repair equipment as soon as it breaks. It would be desirable to be able to test Josephson junction devices well below 77 K and only later test their operation at higher temperatures. One should also fabricate several devices to increase one's chances of acceptable results and observe their parameter spread.

In conclusion, it is certainly possible to fabricate high-T_c SQUIDs at the University of Stellenbosch with the basic process described in this thesis, but it will require a more concerted and organised effort.

References

1. I. M. Firth, *Superconductivity*. London: Mills and Boon, 1972.

2. R. A. Serway, *Physics for Scientists and Engineers with Modern Physics*, 3rd ed. Philadelphia: Saunders College Publishing, 1992, pp. 1290–1342.

3. V. Z. Kresin and S. A. Wolf, *Fundamentals of Superconductivity*. New York: Plenum Press, 1990.

4. T. P. Orlando and K. A. Delin, *Foundations of Applied Superconductivity*. Reading, Massachusetts: Addison-Wesley, 1991.

5. A. Pippard, "The historical context of Josephson's discovery," in *Superconductor Applications: SQUIDs and Machines*, B.B. Schwartz and S. Foner, Eds. New York: Plenum Press, 1997, pp. 1–20.

6. J. H. Hinken, *Superconductor Electronics: Fundamentals and Microwave Applications*. Berlin: Springer-Verlag, 1989, pp. 1–2.

7. D. Fishlock, *A Guide to Superconductivity*. D. Fishlock, Ed. London: Macdonald, 1969.

8. W. J. Perold, M. Jeffery, Z. Wang and T. Van Duzer, "Complementary output switching logic – a new superconductig voltage-state family," *IEEE Transactions on Applied Superconductivity*, vol. 6 no. 3, pp. 125–131, September 1996.

9. P. V. Czipott and W. N. Podney, "Use of a superconductive gradiometer in an ultrasensitive electromagnetic metal detector," *IEEE Transactions on Magnetics*, vol. 25 no. 2, pp. 1204–1207, March 1989.

10. P. V. Czipott and W. N. Podney, "Pulsed operation of a superconductive electromagnetic gradiometer," *IEEE Transactions on Magnetics*, vol. 27 no. 2, pp. 2971–2974, March 1991.

11. J. Clarke in *Superconducting Devices*. S. T. Ruggiero and D. A. Rudman, Eds. San Diego, CA: Academic Press, 1990, ch. 2.

12. J. C. Gallop, *SQUIDs, the Josephson Effects and Superconducting Electronics*. Bristol: Adam Hilger, 1991.

13. J. Lukens in *Superconducting Devices*. S. T. Ruggiero and D. A. Rudman, Eds. San Diego, CA: Academic Press, 1990, ch. 4.

14. E. J. Maritz, National Accelerator Centre, Faure, South Africa. December 1998, Private communication.

15. E. H. Conradie, *The Design and Fabrication of DC SQUID Magnetometers*, Master's thesis. Stellenbosch, University of Stellenbosch, 1998.

16. SPICE (Simulation Program for Integrated Circuit Engineering) was originally developed at the University of California, Berkley in the early 1970's to simulate circuits in the time domain. The original source code has been adapted by several commercial companies to produce a number of more user-friendly simulation packages.

17. R. Gross and P. Chaudari in *Principles and Applications of Superconducting Quantum Interference Devices*. A. Barone, Ed. Singapore: World Scientific, 1992, ch. 7.

18. K. K. Likharev, *Dynamics of Josephson Junctions and Circuits*. Philadelphia: Gordon and Breach Science Publishers, 1986, p. 48.

19. I. A. Powell, *The Simulation and Design of a Dc SQUID Linear Magnetic Flux Detector System*, Master's thesis. Stellenbosch: University of Stellenbosch, 1993.

20. F. Wellstood, C. Heiden and J. Clarke, "Integrated dc SQUID magnetometer with a high slew rate," *Review of Scientific Instruments*, vol. 55 no. 6, pp. 952–957, 1984.

21. D. J. Adelerhof, H. Nijstad, J. Flokstra and H. Rogalla, "(Double) relaxation oscillation SQUIDs with high flux-to-voltage transfer: Simulations and experiments," *Journal of Applied Physics*, vol. 76 no. 6, pp. 3875–3886, September 1994.

22. D. J. Adelerhof, J. Kawai, K. Tsukada, G. Uehara and H. Kado, "Magnetometers based on double relaxation oscillation superconducting quantum interference devices," *Applied Physics Letters*, vol. 66 no. 17, pp. 2274–2276, April 1995.

23. M. Mück and C. Heiden, "Simple dc-SQUID system based on a frequency modulated relaxation oscillator," *IEEE Transactions on Magnetics*, vol. 25 no. 2, pp. 1151–1153, 1989.

24. D. Drung and H. Koch, "An integrated DC SQUID magnetometer with variable additional positive feedback," *Superconductor Science and Technology,* vol. 7 no. 5, pp. 242–245, May 1994.

25. D. Drung, H. Matz and H. Koch, "A 5-MHz bandwidth SQUID magnetometer with additional positive feedback," *Review of Scientific Instruments,* vol. 66 no. 4, pp. 3008–3015, April 1995.

26. D. Drung, "Low-frequency noise in low-T_c multiloop magnetometers with additional positive feedback," *Applied Physics Letters*, vol. 67 no. 10, pp. 1474–1476, September 1995.

27. D. Drung, F. Ludwig, W. Müller, U. Steinhof, L. Trahms and H. Koch, "Integrated $YBa_2Cu_3O_{7-x}$ magnetometer for biomagnetic measurements," *Applied Physics Letters*, vol. 68 no. 10, pp. 1421–1423, March 1996.

28. D. Drung, E. Dansker, F. Ludwig, H. Koch, R. Kleiner, J. Clarke, S. Krey, D. Reimer, B. David and O. Doessel, "Low noise $YBa_2Cu_3O_{7-x}$ magnetometers operated with additional positive feedback," *Applied Physics Letters*, vol. 68 no. 13, pp. 1856–1858, March 1996.

29. V. Foglietti, R. H. Koch, W. J. Gallagher, R. B. Laibowitz and B. Oh in *Nonlinear Superconductive Electronics and Josephson Devices*. G. Costabile, S. Pagano, N. F. Pederson and M. Russo, Eds. New York: Plenum Press, 1991, pp. 95–107.

30. K. Peterson, C. Stölzel, M. Schmitt, C. Krimmer, W. Wilkens, J. Söllner, H. W. Grueninger and H. Adrian, "Fabrication of biepitaxial YBCO Josephson junctions on different substrates," *IEEE Transactions on Applied Superconductivity*, vol. 5, no.2, pp. 2180–2183, June 1995.

31. K. Char, M. S. Colclough, S. M. Garrison, N. Newman and G. Zaharchuk, "Bi-epitaxial grain boundary junctions in $YBa_2Cu_3O_7$," *Applied Physics Letters*, vol. 59, no. 6, pp. 733–735, August 1991.

32. J. R. Hook and H.E.Hall, *Solid State Physics,* 2nd ed. Chichester: John Wiley, 1991, p. 310–313.

33. J. M. Phillips, "Substrate selection for high-temperature superconducting thin films," *Journal of Applied Physics*, vol. 79 no. 4, pp. 1829–1848, February 1996.

34. MaTeck GmbH, Crystal manufacturer, http://www.physik.de/mateck/s05e.htm, Karl-Heinz-Beckurts-Str. 13, D-52428 Juelich, Germany.

35. S. Sandner, Crystal GmbH, Ostendstr. 1–14, D-12459 Berlin, Germany. Internet: www.crystal-gmbh.com. February 1999, Private communication.

36. J. Clarke in *The New Superconducting Electronics*. H. Weinstock and R. W. Ralston, Eds. Dordrecht: Kluwer Academic, 1993, ch. 5.

37. R. Cantor, L.P. Lee, M. Teepe, V. Vinetskiy and J. Longo, "Low noise, single layer $YBa_2Cu_3O_{7-x}$ magnetometers at 77 K," *IEEE Transactions on Applied Superconductivity*, vol. 5 no. 2, pp. 2927–2930, June 1995.

38. G. M. Daalmans, L. Bär, M. Kühnl, D. Uhl, M. Selent and J. Ramos, "Single layer YBaCuO – Gradiometer," *IEEE Transactions on Applied Superconductivity*, vol. 5 no. 2, pp. 3109–3112, June 1995.

39. M. B. Ketchen, W. J. Gallagher, A. W. Kleinsasser, S. Murphy and J. R. Clem, "Dc SQUID flux focuser," in *SQUID '85 Superconducting Quantum Interference Devices and their Applications*, H. Hahlbohm and H. Lübbig, Eds. Berlin: Springer-Verlag, 1985, pp. 865–871.

40. E. J. Romans, T. G. Henrici, C. Carr, J. C. MacFarlane, C. M. Pegrum and D. B. Donaldson, "The properties of HTS Josephson junctions and dc SQUIDs fabricated on MgO bicrystals," *IEEE Transactions on Applied Superconductivity*, vol. 7 no. 2, pp. 2530–2533, June 1997.

41. B. C. Wadell, *Transmission Line Handbook*. Boston: Artech House, 1991, pp. 83, 402–403.

42. K. Enpuku, , Y. Shimomura and T. Kisu, "Effect of thermal noise on the characteristics of a high T_c superconducting quantum interference device," *Journal of Applied Physics*, vol. 73 no. 11, pp. 7929–7934, June 1993.

43. D. Koelle, A. H. Miklich, F. Ludwig, E. Dantsker, D. T. Nemeth and J. Clarke, "Dc SQUID magnetometers from single layers of $YBa_2Cu_3O_{7-x}$," *Applied Physics Letters*, vol. 63 no. 16, pp. 2271–2273, October 1993.

44. L. Vonderbeck, C. A. Copetti, A. M. Klushin, G. Kunkel, M. Siegel, E. Sodtke, J. Schubert and W. Zander, "Investigation of $YBa_2Cu_3O_7$ Josephson junctions on MgO Bicrystal Substrates," *IEEE Transactions on Applied Superconductivity*, vol. 5 no. 2, pp. 2176–2179, June 1995.

45. J. Beyer, D. Drung, F. Ludwig, T. Minotani and K. Enpuku, "Low-noise $YBa_2Cu_3O_{7-x}$ single layer dc superconducting quantum interference device (SQUID) magnetometer based on bicrystal junctions with 30° misorientation angle," *Applied Physics Letters*, vol. 72 no. 2, pp. 203–205, January 1998.

46. D. Koelle, A. H. Miklich, E. Dantsker, F. Ludwig, D. T. Nemeth, J. Clarke, W. Ruby and K. Char, "High performance dc SQUID magnetometers with single layer $YBa_2Cu_3O_{7-x}$ flux transformers," *Applied Physics Letters*, vol. 63 no. 26, pp. 3630–3632, December 1993.

47. P. Å. Nilsson, Z. G. Ivanov, H. K. Olsson, D. Winkler, T. Claeson, E. A. Stepantsov and A.Ya. Tzalenchuk, "Bicrystal junctions and superconducting quantum interference devices in $YBa_2Cu_3O_7$ thin films," *Journal of Applied Physics*, vol. 75 no. 12, pp. 7972–7977, June 1994.

48. R. Gross, P. Chaudhari, M. Kawasaki, M. B. Ketchen and A. Gupta, "Low noise $YBa_2Cu_3O_{7-\delta}$ grain boundary junction dc SQUIDs," *Applied Physics Letters*, vol. 57 no. 7, pp. 727–729, August 1990.

49. R. Gross, P. Chaudhari, M. Kawasaki, M. B. Ketchen and A. Gupta, "Characteristics of $YBa_2Cu_3O_{7-\delta}$ grain boundary junction dc-SQUIDs," *IEEE Transactions on Magnetics*, vol. 27 no. 2, pp. 2565–2568, March 1991.

50. R. Gross, P. Chaudhari, M. Kawasaki, M. B. Ketchen and A. Gupta, "Scaling behaviour in $YBa_2Cu_3O_{7-\delta}$ superconductors," *Physical Review B*, vol. 42 no. 16, pp.10736–10737, December 1990.

51. E. Il'ichev, L. Dörrer, F. Schmidl, V. Zakosarenko, P. Seidel and G. Hildebrandt, "Current resolution, noise, and inductance measurements on high-T_c dc SQUID galvanometers," *Applied Physics Letters*, vol. 68 no. 5, pp. 708–710, January 1996.

52. C. D. Tesche and J. Clarke, "Dc SQUID: noise and optimization," *Journal of Low Temperature Physics*, vol. 29, no. 3/4, pp. 301–331, 1977.

53. Maxwell 3d Parameter Extractor, Ansoft Corporation, Pittsburgh.

54. S. Haykin, *An Introduction to Analog and Digital Communications*, 3rd ed. New York: John Wiley, 1989, pp. 604–606.

55. F. G. Stremler, *Introduction to Communication Systems*. Reading, Massachusetts: Addison-Wesley, 1990, pp. 190–191.

56. J. J. P. Bruines, V. J. de Waal and J. E. Mooij, "Comment on: "Dc SQUID: noise and optimization" by Tesche and Clarke," *Journal of Low Temperature Physics*, vol. 46, no. 3/4, pp. 383–386, 1982.

57. J. Clarke, "Principles and applications of SQUIDs," *Proceedings of the IEEE*, vol. 77 no. 8, pp. 1208–1223, August 1989.

58. R. H. Koch, W. Eidelloth, B. Oh, R. P. Robertazzi, S. A. Andrek and W. J. Gallagher, "Identifying the source of 1/f noise in SQUIDs made from high-temperature superconductors," *Applied Physics Letters*, vol. 60 no. 4, pp. 507–509, January 1992.

59. Y. Huang, K. L. Merkle, L. P. Lee, M. Teepe and K. Char, "Microstructural origin of 1/f noise in high T_c bicrystal SQUID magnetometers," *Applied Physics Letters*, vol. 71 no. 25, pp. 3703–3705, December 1997.

60. M. Kawasaki, P. Chaudari and A. Gupta, "1/f Noise in $YBa_2Cu_3O_{7-\delta}$ superconducting grain-boundary junctions," *Physical Review Letters*, vol. 68 no. 7, pp. 1065–1068, February 1992.

61. A. Marx, U. Fath, L. Alff and R. Gross, "Correlation of critical current and resistance fluctuations in bicrystal grain boundary junctions," *Applied Physics Letters*, vol. 67 no. 13, pp. 1929–1931, September 1995.

62. Y. Song, A. Misra, P. P. Crooker and J. R. Gaines, "Anisotropic 1/f noise and motion of magnetic vortices in $YBa_2Cu_3O_{7-\delta}$," *Physical Review B*, vol. 45 no. 13, pp. 7574–7576, April 1992.

63. A. H. Miklich and J. Clarke, "Flicker (1/f) noise in biepitaxial grain boundary junctions of $YBa_2Cu_3O_{7-\delta}$," *Applied Physics Letters*, vol. 60 no. 15, pp. 1899–1901, April 1992.

64. A. Adachi, K. Okajima, S. Tanaka, H. Toyoda and H. Itozaki, "A high-T_c superconducting interference device with an alternating current bias DOIT and additional positive feedback," *Superconductor Science and Technology*, vol. 9, pp. A100–A104, 1996.

65. G. Koren, A. Gupta, R. J. Baseman, M. I. Lutwyche and R. B. Laibowitz, "Laser wavelength dependent properties of $YBa_2Cu_3O_{7-\delta}$ thin films deposited by laser ablation." *Applied Physics Letters*, vol. 55 no. 23, pp. 2450–2452, December 1989.

66. RUMP is a software package for simulating Rutherford backscattering spectra. The original FORTRAN code was developed at Cornell University in Dr. J.W. Mayer's research group by the then graduate students L.R. Doolittle and M.O. Thompson with assistance from R.C. Cochran. The development of efficient simulation and search algorithms formed a major part of L.R. Doolittle's thesis.

67. R. S. Sokhi, P. W. Gilberd and L. G. Earwaker, "Investigation of films of $YBa_2Cu_3O_7$ using Rutherford backscattering spectrometry." *Nuclear Instruments and Methods in Physics Research B*, vol. 50, pp. 140–144, 1990.

68. S. Marais. Institute for Polymer Science, University of Stellenbosch, 1999, Private communication http://www.sun.ac.za/polymer/snom.htm, http://www.topometrix.com/teched_afm.htm.

69. H. S. Kim and H. S. Kwok, "Correlation between target-substrate distance and ocygen pressure in pulsed laser deposition of $YBa_2Cu_3O_7$." *Applied Physics Letters*, vol. 61 no. 18, pp. 2234–2236, November 1992.

70. S. F. Xu, Y. J. Tian, H. B. Lü, D. F. Cui, Z. H. Chen, L. Li and G. Z. Yang, "The effect of laser energy density and target-substrate distance on the quality of $YBa_2Cu_3O_{7-x}$ thin films." *Superconductor Science and Technology*, vol. 7, pp. 435–437, 1994.

71. C. Curran, National Accelerator Centre, South Africa. March 1999, Private communication.

72. H. S. Kwok and Q. Y. Ying, "Dynamics of in situ $YBa_2Cu_3O_7$ superconducting film formation." *Physica C*, vol. 177, pp. 122–128, 1991.

73. B. Dam, J. Rector, M. F. Chang, D. G. de Groot and R. Griessen, "Laser ablation threshold of $YBa_2Cu_3O_{6+x}$." *Applied Physics Letters*, vol. 65 no. 12, pp. 1581–1583, September 1994.

74. AutoCAD® release 13, Registered trademark of Autodesk, Inc.

75. Rubylith® masking film produced by Ulano Corporation, 110 Third Avenue, Brooklyn, NY 11217.

76. Millimask photographic glass plates are manufactured by Agfa-Gevaert. In South Africa they are a division of Beyer.

77. M. J. Langford, *Basic Photography*, 4th ed. London: Focal, 1977.

78. B. Meyer at Pico Systems CC.
Personal e-mail: bmeyer@csir.co.za
Address: Building 43, CSIR, Meiring Naude Road, Pretoria.
Postal address: P.O. Box 39290, Moreletapark, 0044, South Africa.
E-mail: pico@pico.co.za

79. A. Vader and G. Germishuisen at Tellumat, Retreat, Cape Town. Tellumat is comprised of certain assets of the former Plessey Corporation and possesses extensive microfabrication facilities.

80. J. Elliott, *Integrated Circuit Fabrication Technology*. New York: McGraw-Hill, 1982.

81. Shipley, Advice from Shipley agent concerning photolithographic process, 1998.

82. Mr SQUID™ (Conductus Inc., 969 West Maude Ave., Sunnyvale, Ca 94086, USA) magnetic shield for dc SQUID. Co-netic alloy tube equivalent to Magnetic Shield Corp (740 North Thomas Drive, Bensenville, Il 60106, USA) model 06P35.

83. H. A. Haus and J. R. Melcher, *Electromagnetic Fields and Energy*. Englewood Cliffs, New Jersey: Prentice Hall, 1989, pp.322-323.

Appendix A

Intusoft SPICE model for the dc SQUID

```
*SRC=DC;DCSQUID;Behavioral;Superconductors;SQUID (Unaveraged)
*SYM=DCSQUID
.SUBCKT DCSQUID  8 1 4 {RJ=2 IJCRIT=3.75U L=50P}

* Loop inductance is included by placing two inductors above the JJ's (B-sources)

*Inductors
Lloop1 1 10 {L}/2
Lloop2 1 11 {L}/2

* Junction 1
Bjunc1 10 2 I={IJCRIT}*SIN(V(5))
Rjunc1 10 2 {RJ}
VI1 2 4 0

* Junction 2
Bjunc2 11 3 I={IJCRIT}*SIN(V(6))
Rjunc2 11 3 {RJ}
VI2 3 4 0

* psi1
Bpsi1 0 5 I=V(10,4)*2*3.141593/2.07F
Cpsi1 5 0 1
Rpsi1 5 0 100meg

*psi2
Bpsi2 6 0 V=V(5)+2*3.141593/2.07F*V(7)
Rpsi2 6 0 1

* enclosed flux
Bphi 7 0 V=V(8)+{L}*V(9)
Rphi 7 0 1

* circulating current
BIcirc 9 0 V=(I(VI1)-I(VI2))/2
RIcirc 9 0 1

.ENDS
```

Appendix B

Inductance formulas

The inductance of a SQUID slit is modelled as two coplanar strip-lines, giving [40]

$$L_{par} = \mu_0 \frac{K(k)}{K(k')} l_{par} , \tag{D.1}$$

where $k = \frac{s}{(s+2w)}$, $k' = \sqrt{1-k^2}$, K is a complete elliptical integral of the first kind, w is the width, s is the distance between the lines and l_{par} is the length of the lines.

The inductance of a single-turn, rectangular planar inductor is given by [41] as

$$L = 23\,390\left[(l_1 + l_2)\log\left(\frac{2l_1 l_2}{w+t}\right) - l_1 \log(l_1 + g) - l_2 \log(l_2 + g)\right]$$
$$+10\,160\left[2g - \left(\frac{l_1 + l_2}{2}\right) + 0.447(w+t)\right], \tag{D.2}$$

where l_1 and l_2 are the outer dimensions of the loop, $g = \sqrt{l_1^2 + l_2^2}$, and w and t are respectively the width and thickness of the line. All dimensions are in inches!

Appendix C

Chemicals for superconducting device fabrication

C1 Recipe for Kodak D8 high-contrast developer

Name	Chemical formula	Function	Quantity
Sodium sulphite (desiccated)	Na_2SO_3	Preservative	90.0 g
Hydroquinone	$C_6H_4(OH)_2$	Developer	45.0 g
Sodium hydroxide	NaOH	Accelerator	37.5 g
Potassium bromide	KBr	Restrainer	30.0 g
Water at 32 °C	H_2O	Solvent	750 ml

Mix ingredients and add cold water until total volume is 1 000 ml.

Note If the developer is exposed to air for too long, it turns a dark brown colour and should not be used. Slight discolouration does not appear to affect performance.

C2 Citric acid solution suitable for etching YBCO films

Name	Chemical formula	Quantity
Citric acid	$C_6H_8O_7 \cdot H_2O$	10.2 g
Water	H_2O	500 ml

C3 Etch for exposing bicrystal line

Name	Chemical formula	Quantity
Hydrofluoric acid	HF	1% solution

Note Particular care should be taken when handling this acid because of its rather unpleasant effects on the human body.

C4 Non-acid gold etch

Name	Chemical formula	Quantity
Potassium iodide	KI	340 g
Iodine	I_2	7 g
Water	H_2O	200 ml

Dissolve ingredients at 50 °C.

C5 Photoresist chemicals

Shipley Microposit® S1818 photoresist
Shipley Microposit® MF®-319 developer
Shipley Microposit® 1165 remover

Note MF319 developer must be replenished regularly during processing or development will be unpredictable.

Appendix D

Using the laboratory equipment

D1 Mamiya-Sekor 210 mm camera and light-box

1. Tape the 20:1 negative artwork to the light-box.
2. Set the camera aperture to f/4, focus the image on a ground-glass plate with the help of a microscope and close down the aperture to f/8. This is done with the light-box on and the other lights off.
3. Turn off all lights except the red light.
4. Place a photographic plate in the camera, emulsion side facing the artwork, and close the camera and plate box. The emulsion side of the plate is indicated on the inside of the box by means of a plastic pin which can be felt in the dark.
5. Switch on the light-box at the wall plug for the required time.
6. Turn off the light-box and remove the plate for developing.
7. Rinse the plate in deionised water for 2 min.
8. Develop using Kodak D8 diluted 1:3 until the image is dark enough.
9. Rinse in deionised water for 1 min.
10. Fix with Acufix fixer diluted 1:3 for 2.5 min.
11. Rinse in running water.
12. Rinse in deionised water for 5–10 min.
13. Rinse in ethanol and blow dry with compressed nitrogen to prevent water stains.

Note

1. During processing, the mask is held with a pair of Perspex tweezers.
2. Processing is done in plastic containers to prevent scratching and chipping.

D2 Spinner

1. Switch on the vacuum pump.
2. Place the substrate on an appropriately sized O-ring on the chuck in the centre.
3. Set the timer for the desired spin time.
4. Press the front foot pedal to start, and adjust the speed according to the speed display.
5. Stop with the rear foot pedal.
6. Drop photoresist on the substrate using a syringe and make sure that the entire substrate is covered. Do not take too long or the resist will start to dry.
7. Put the lid on and start the spin. Spinning will stop automatically at the correct time.

Note

1. The timer is very inaccurate and should always be checked.
2. The spinner rotates slightly faster if it has just been used so one should keep an eye on the speed display.

D3 Karl Süss MJB3 mask-aligner

1. Switch on at least an hour before use. Make sure the vacuum pump is on and that the compressed air is at the correct pressure. Check that the **Source UV** and **Microscope** switches are on and that the **Mask** and **Maskholder** switches are off. Make sure that the contact lever is in the separation position.
2. Slide the substrate holder out to the right, place the coated substrate in the middle of the round plate and replace the holder.
3. Place the mask on the appropriate mask-holder with the emulsion/chrome side facing upwards. Switch on the **Mask** vacuum to suck it to the holder. Turn the holder upside down and slide in above the substrate from the left. It is advisable to hold one's hand underneath to catch the mask in the event of a vacuum failure (which actually does happen from time to time).
4. Align the substrate with the mask under the microscope using the X, Y and angular orientation micrometer screws. The black button under the eye-pieces switches between the two magnification settings.
5. The microscope can be moved across the substrate with the manipulator lever on the left. Depressing the red button releases the brake.
6. When the alignment is complete, the contact lever can be moved slowly towards the **Contact** position. The substrate can still be moved with the micrometer screws until it touches the mask. Alignment is easier when the substrate and mask are nearly in the same focal plane. The **Contact** light goes on when properly in contact.
7. Set the timer for the desired ultraviolet exposure time, making use of the multiplication factor.
8. Press the green **Exposure** button quickly. The whole lamp assembly will move forward, expose for the correct time, and move back.
9. Move the contact lever slowly back from the contact position. It must be done this way because the substrate often sticks to the mask.
10. Slide out the substrate holder and remove the substrate.
11. Slide out the mask assembly, invert it, and turn of the **Mask** switch to release the mask.

Note A pair of tweezers made from a broken Fluoroware® pair is used to hold the substrate at all times. A spring allows the tweezers to maintain a firm, but gentle grip on the substrate. An adjustable spacer prevents the tips from closing to much less than the substrate width. This stops the substrate from being flicked out by the spring if it not properly gripped.

D4 Etching in ultrasonic bath

1. Fill the bath with water to more than half capacity.
2. Switch on and hold the etching container partially submerged.

Note Beware of droplets thrown out by standing waves in the etchant.

D5 Depositing YBCO films using the National Accelerator Centre's pulsed laser deposition system

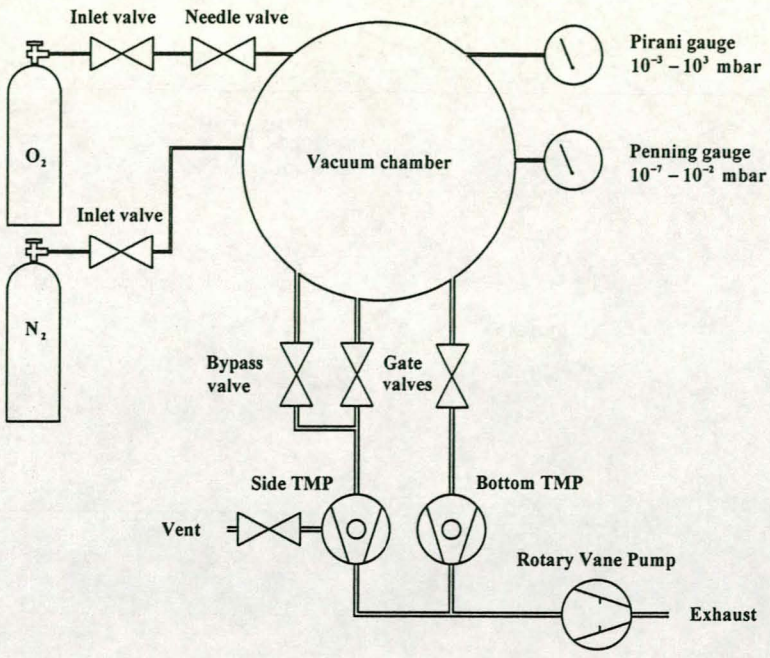

Figure D1 Diagram showing the PLD system layout.

1. Take off the top lid of the chamber and remove target with an Allen key.
2. Clean the target surface with course and fine sandpaper and blow away dust with compressed air.
3. Replace target, bearing in mind the target-substrate separation. It is easier to measure the distance between the target surface and the rear of the nearest steel plate (normally 37 mm).
4. Place seal assembly in lid's groove and replace lid.
5. Undo bolts from side flange and carefully remove substrate-holder assembly after removing heater/thermocouple socket. Place on wooden blocks above flat surface.
6. Turn shutter to the side and remove heat shield.
7. Clean substrate heater surface with fine sandpaper and methanol.
8. Coat centre of heater surface with thin layer of silver paint and drop substrate (shiny side up) onto it. Press down with back of tweezers.
9. Replace heat shield and check that substrate is centred. Adjust if necessary.
10. Allow to dry for at least 10 minutes. If ambient temperature is too low, connect heater leads and heat to about 30 °C.
11. Replace heater assembly and loosely tighten bolts. Reconnect heater/thermocouple socket.
12. Check that all gas inlet valves are closed (see Figure D1). Open bypass valve. Switch on rotary vane pump. Switch on the power supplies of both gate valves. Open both side and bottom gate valves by turning compressed air entry valve to the left and right respectively. Return to centre position. If a gate valve does not want to open, temporarily leave entry valve at its left or right position and switch

its power supply on and off until it opens. Switch on cooling fan for side turbo-molecular pump (TMP) and open cooling water for bottom TMP. Switch on both TMP's at their controller boxes.

13. After about 10 minutes, tighten flange bolts properly and leave for at least 12 hours to achieve a low enough base pressure ($2-3\times10^{-6}$ mbar).
14. Prepare laser for use by following its instructions but do not trigger it.
15. Place pyro-electric detector in the beam path.
16. Adjust laser energy and pulse frequency to desired level and pulse rate with oscilloscope (150 mJ, 10 Hz). Switch off output and remove pyro-electric detector.
17. Switch temperature control to the variac. Slowly turn up the variac voltage to about 67 V, ensuring that the heater current does not exceed about 5.5 A. (Use the multimeters for reference). Only minor changes to this voltage setting should be necessary to keep the substrate temperature constant at 795 °C.
18. Close both gate valves by switching off their power supplies and activating them with the entry valve as was done previously to open them. Switch off bottom TMP.
19. Open the oxygen shut-off valve and adjust the needle valve to obtain the desired oxygen pressure (0.3 mbar).
20. Make sure the correct target is in position and switch on the target rotator.
21. Check that the shutter is closed and switch on the laser output. Pre-ablate the target for several minutes during which time the alignment can be checked for obvious errors.
22. Open the shutter for the required deposition time (2.5 minutes) and switch of the laser when this is finished. When the shutter has just been opened do a final check on the alignment.
23. Lower the substrate temperature by reducing the variac voltage.
24. Close the bypass valve and switch off the side TMP and the rotary vane pump
25. Open oxygen inlet valve until chamber pressure reaches 900 mbar.
26. Maintain temperature at 490 °C for 30 minutes either by using variac (33 V) or by disconnecting variac and using temperature controller.
27. Switch off heater and allow to cool to below about 150 °C.
28. Open bypass valve and pump out oxygen with rotary vane pump (for safety).
29. Close bypass valve and switch off rotary vane pump. Let in nitrogen and then vent vacuum pump.
30. Unbolt flange and remove heater assembly.
31. Gain access to substrate as mentioned previously and remove substrate with razor blade.

Note

1. Rubber seals and their metal contact surfaces must be cleaned each time they are removed with a dry cloth to remove dirt and metal particles.
2. Turn off compressed air valve at wall when not in use.
3. After pumping down has started, it is advisable to check whether the substrate is still attached to the heater.
4. Laser energy should be measured at a low pulse rate, typically 2 Hz, to avoid the effects of the detector's large time-constant.

5. One should always keep an eye on the target rotator during depositions as it is inclined to stop each now and again. It can be helped along manually.
6. Substrates should always stored in a desiccator.
7. If the system is used to deposit gold contact pads, the mask (with the substrate inside) should be stuck to the heater surface with press-stick. The heat shield should not be used. A gold target is used and the deposition is performed at room temperature and about 10^{-5} mbar. The gold should be deposited for a long time (typically 3 hours) since thick contact pads are desirable and the deposition rate for gold is much lower than that for YBCO.

Appendix E

Summary of the complete photolithographic process

Exposing grain boundary

Action	Time	Details
Spin	90 s	5 000 rpm
Dry	10 min	Room temperature
Bake	30 min	100 °C
Cool	10 min	Room temperature
Expose	3 min	Edge mask
Develop	30 s	MF319
Bake	30 min	110 °C
Cool	10 min	Room temperature
Etch	70 s or until underlying substrate is exposed	Citric acid
Etch	5 min or until grain boundary is visible	1% HF
Remove resist	Until clean	1165 remover
Rinse		Ethanol
Blow dry		Compressed Nitrogen

Etching design

Action	Time	Details
Spin	90 s	5 000 rpm
Dry	10 min	Room temperature
Bake	30 min	100 °C
Cool	10 min	Room temperature
Expose	3 min	Edge mask
Develop	30 s	MF319
Align device mask with bicrystal line on substrate		
Expose	20 s	Device mask
Develop	40 s	MF319
Bake	30 min	110 °C
Cool	10 min	Room temperature
Etch	70 s or until underlying substrate is exposed	Citric acid
Remove resist	Until clean	1165 remover
Rinse		Ethanol
Blow dry		Compressed Nitrogen

Notes

1. Yellow filters must be placed over the all lights to prevent any ultraviolet from reaching the photoresist.
2. In order to check the progress of the etching, the substrate is viewed under a microscope with polarised light.
3. After processing, the etched device is stored in a desiccator to prevent water vapour from degrading the YBCO.
4. Deionised water should be used for washing off the etch so that chemical action is stopped completely. In addition, nitrogen gas is bubbled through the water to displace any CO_2 dissolved in the form of carbonic acid (H_2CO_3).
5. The entire process takes about 4½ hours.
6. If the photolithography is unsuccessful and desired shape is not formed correctly in the photoresist prior to the final bake, all remaining resist should be removed with 1165 remover. The substrate should then be washed in ethanol and dried with compressed nitrogen. The part of the process entitled "Etching design" should then be repeated with hopefully improved results.